

IDEALIZED MODELING OF CIRCULATION UNDER LANDFAST ICE

A  
THESIS

Presented to the Faculty  
of the University of Alaska Fairbanks

in Partial Fulfillment of the Requirements  
for the Degree of

Doctor of Philosophy

By

Jeremy Lucas Kasper, B.A.

Fairbanks, Alaska

December 2010

UMI Number: 3451181

All rights reserved

INFORMATION TO ALL USERS

The quality of this reproduction is dependent upon the quality of the copy submitted.

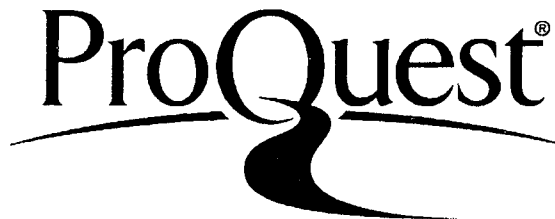
In the unlikely event that the author did not send a complete manuscript and there are missing pages, these will be noted. Also, if material had to be removed, a note will indicate the deletion.



UMI 3451181

Copyright 2011 by ProQuest LLC.

All rights reserved. This edition of the work is protected against unauthorized copying under Title 17, United States Code.




ProQuest LLC  
789 East Eisenhower Parkway  
P.O. Box 1346  
Ann Arbor, MI 48106-1346

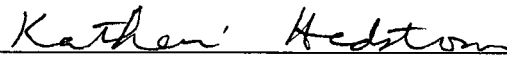
IDEALIZED MODELING OF CIRCULATION UNDER LANDFAST ICE

By

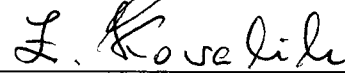
Jeremy L. Kasper


RECOMMENDED:


  
\_\_\_\_\_  
Dr. Rolf Gradinger

  
\_\_\_\_\_  
Dr. Katherine Hedström

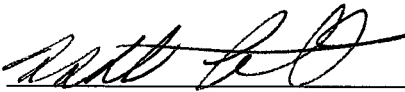
  
\_\_\_\_\_  
Dr. Mark Johnson

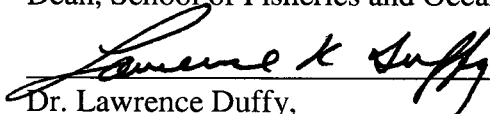
  
\_\_\_\_\_  
Dr. Zygmunt Kowalik

  
\_\_\_\_\_  
Dr. Thomas Weingartner, Advisory Committee Chair

  
\_\_\_\_\_  
Dr. Katrin Iken,  
Head, Program in Marine Science and Limnology

APPROVED:

  
\_\_\_\_\_  
Dr. Michael Castellini,  
Dean, School of Fisheries and Ocean Sciences

  
\_\_\_\_\_  
Dr. Lawrence Duffy,  
Dean of the Graduate School

  
\_\_\_\_\_  
Date

## Abstract

Idealized analytical and numerical models are used to elucidate the effects of a spatially variable landfast ice cover on under-ice circulation. Three separate forcing mechanisms are investigated; lateral inflow onto an ice-covered shelf (an elevated sea level at the western boundary), a spatially uniform upwelling wind blowing along the seaward landfast ice edge and a buoyant inflow under the ice cover that enters the domain through the southern coastal wall. The idealized models are configured to resemble the shallow Alaskan Beaufort Sea shelf. Models show that the inclusion of landfast ice means shelf response is substantially different from an ice-free shelf. In the case of a lateral inflow, landfast ice spreads the inflow offshore (in a manner similar to bottom friction) but the change in surface stress across the ice edge (from ice-covered to ice-free) limits the offshore spreading. In the case of an upwelling wind along the ice edge, the low sea level at the ice edge (due to ice edge upwelling) leads to a cross-shore sea level slope between the coast (high sea level) and the ice edge (low sea level), which drives a geostrophically balanced flow upwind. In the absence of along-shore changes in wind or ice the circulation does not vary along the shelf and currents near the coast are  $O(10^{-3}) \text{ m s}^{-1}$ . Along- and cross-shore variations in the ice-ocean friction coefficient introduce differences in the response time of the under-ice flow and can lead to along-shore sea level slopes, which drive along-shore flows near the coast ( $< 0.06 \text{ m s}^{-1}$ ). In the case of a time dependent buoyant inflow, the landfast ice spreads the buoyant inflow much farther offshore ( $\sim 9$  times the local baroclinic Rossby radius,  $\sim 45 \text{ km}$ ) than in the ice-free case ( $< 30 \text{ km}$ ). When the ice width is finite, the change in surface across the ice edge acts to

restrict offshore flow (in the anti-cyclonic bulge) and inhibits onshore flow farther downstream.

## Table of Contents

	Page
Signature Page .....	i
Title Page .....	ii
Abstract.....	iii
Table of Contents.....	v
List of Figures.....	viii
List of Tables .....	xi
Acknowledgements.....	xii
Introduction.....	1
References.....	8
Figures .....	11
Chapter 1 The effect of landfast ice on a lateral inflow to a shelf sea.....	15
Abstract.....	15
1.1 Introduction.....	16
1.2 The analytic model.....	19
1.2.1 Solution by separation of variables.....	22
1.2.1.1 Boundary conditions .....	24
1.2.1.1.1 Initial condition.....	27
1.3 Numerical results .....	32
1.4 Comparison of analytic and numerical results.....	36
1.5 Summary and conclusions .....	42

1.6 Appendix.....	44
1.6.1 Governing equations.....	48
1.6.2 Initial condition.....	54
1.6.3 Stream-functions.....	55
1.7 References.....	57
1.8 Figures.....	61
1.9 Tables.....	73
Chapter 2 Modeling winter circulation under landfast ice: The interaction of winds with landfast ice.....	75
Abstract.....	75
2.1 Introduction.....	76
2.2 The governing vorticity equation.....	79
2.3 Numerical model results.....	83
2.3.1 Model description.....	83
2.3.2 The basic vertically averaged experiments.....	86
2.3.3 Three dimensional results.....	89
2.3.4 Sensitivity results.....	93
2.3.5 The vorticity terms.....	97
2.3.6 Along-shore variations in under-ice friction.....	101
2.3.7 Along-shore variations of ice width.....	103
2.4 Discussion and conclusion.....	106
2.5 Appendix.....	109

2.6 References.....	113
2.7 Figures .....	116
2.8 Tables.....	131
Chapter 3 The spreading of a buoyant plume beneath a landfast ice cover.....	132
Abstract.....	132
3.1 Introduction.....	132
3.2 Model description .....	137
3.3 Results.....	138
3.4 Discussion and summary .....	166
3.5 References.....	170
3.6 Figures .....	176
Summary and conclusions .....	193
References.....	199



## List of Figures

	Page
Figure 0.1. Two seasons: the seasonal cycle of the Alaskan Beaufort Sea shelf.....	11
Figure 0.2. Map of the Alaskan Beaufort Sea and of the North Slope of Alaska.....	12
Figure 0.3. Spring conditions on an Arctic shelf sea. ....	13
Figure 0.4. The spring freshet. ....	14
Figure 1.1. Coordinate system for the ALW, the landfast ice analytic model.....	61
Figure 1.2. Magnitude of the ice-ocean friction coefficient. ....	62
Figure 1.3. Contours of sea level anomaly, $\eta$ (m). ....	63
Figure 1.4. The effect of the ice-ocean friction coefficient on $\eta$ . ....	64
Figure 1.5. Transport streamlines for the analytical ALW solution. ....	65
Figure 1.6. Contours of sea level anomaly, $\eta$ (m). ....	66
Figure 1.7. Along- and cross-shore transport. ....	67
Figure 1.8. Normalized along-shore sea level slope ( $m^{-1}$ ) versus the magnitude of the ice-ocean friction coefficient ( $m s^{-1}$ ). ....	68
Figure 1.9. Normalized along-shore sea level slope ( $m^{-1}$ ) versus the magnitude of the cross-shore variability of ice-ocean friction coefficient ( $m s^{-1}$ ). ....	69
Figure 1.10. Normalized along-shore sea level slope ( $m^{-1}$ ) versus the magnitude of the along-shore variability of ice-ocean friction coefficient ( $m s^{-1}$ ). ....	70
Figure 1.11. Normalized along-shore sea level slope ( $m^{-1}$ ) versus ice width (km). ....	71
Figure 1.12. Contours of $\eta$ (m) from numerical results. ....	72
Figure 2.1. Coordinate systems. ....	116

Figure 2.2. The ice-ocean friction coefficient. ....	117
Figure 2.3. Numerical results. ....	118
Figure 2.4. Under-ice velocities.....	119
Figure 2.5. The under-ice boundary layer.....	120
Figure 2.6. Currents near the ice edge. ....	121
Figure 2.7. Particle trajectories. ....	122
Figure 2.8. Cross-shore sea level slope and frictional adjustment time versus the magnitude of the ice-ocean friction coefficient. ....	123
Figure 2.9. Cross-shore sea level slope and frictional adjustment time as functions of cross-shore variability in the ice-ocean friction coefficient. ....	124
Figure 2.10. Effect of ice width on the cross-shore sea level slope. ....	125
Figure 2.11. The under-ice vorticity terms. ....	126
Figure 2.12. The effect of along-shore variations in $r_{ice}$ on under-ice circulation. ....	127
Figure 2.13. The effect of along-shore variations in the ice width on under-ice circulation. .....	128
Figure 2.14. The effect of along-shore changes in ice coverage on under-ice circulation. .....	129
Figure 2.15. An under-ice vorticity wave. ....	130
Figure 3.1. Mean daily discharge for the Colville River (2003-2007). ....	176
Figure 3.2. The numerical model domain and forcing. ....	177
Figure 3.3. Density anomaly, $\Delta\rho$ ( $\rho-1000$ , kg m <sup>-3</sup> ), at the surface. ....	178
Figure 3.4. Along-shore velocity, $u$ (m s <sup>-1</sup> ) at the surface. ....	179

Figure 3.5. Cross-shore velocity, $v$ ( $\text{m s}^{-1}$ ) at the surface. ....	180
Figure 3.6. Vertical velocity, $w$ ( $\text{m s}^{-1}$ ) at the surface. ....	181
Figure 3.7. Plume area ( $10^3 \text{ km}^2$ ) on day 30 versus ice width (km). ....	182
Figure 3.8. Freshwater flux, $F$ versus time. ....	183
Figure 3.9. Integrated transport ( $\text{m}^3 \text{ s}^{-1}$ ). ....	184
Figure 3.10. Location of the $\Delta\rho = 25 \text{ kg m}^{-3}$ contour at 5 - 30 days (at 5 day intervals). ....	185
Figure 3.11. Cross-shelf sections of the density anomaly, $\Delta\rho$ ( $\text{kg m}^3$ ). ....	186
Figure 3.12. Cross-shelf sections of $u$ , along-shore velocity ( $\text{m s}^{-1}$ ). ....	187
Figure 3.13. Cross-shelf sections of $v$ , cross-shore velocity ( $\text{m s}^{-1}$ ). ....	188
Figure 3.14. Cross-shelf sections of $w$ , vertical velocity ( $\text{m s}^{-1}$ ). ....	189
Figure 3.15. The important terms in the under-ice salinity balance. ....	190
Figure 3.16. The salinity balance ( $\text{s}^{-1}$ ) on day 30 from experiment 3 at $x = 100 \text{ km}$ and $y = 46 \text{ km}$ . ....	191
Figure 3.17. Plume area ( $10^3 \text{ km}^2$ at day 30) versus the $\log_{10}(r_{ice})$ for a 26 km wide ice cover. ....	192

## List of Tables

	Page
Table 1.1. Range of ice parameters considered. The range of $r_{ice}$ considered is $0 - 10^{-3}$ m $s^{-1}$ .....	73
Table 1.2. Eigenvalues of the analytic landfast model for the basic analytical ALW solution, constants as given in Table 1.1. ....	74
Table 2.1. Range of ice parameters considered. ....	131

## Acknowledgements

The following organizations graciously supported this research: The Prince William Sound Oil Spill Recovery Institute (OSRI), Alaska Sea Grant in cooperation with the Center for Global Change, the University of Alaska Fairbanks (UAF) Graduate School and the U.S. Bureau of Ocean Energy Management, Regulation and Enforcement (formerly the Minerals Management Service) in cooperation with the University of Alaska Coastal Marine Institute (Contract Number 1435-01-02-CA-85294). Most recently this research was funded by the Office of Naval Research through the National Oceanographic Partnership Program. In addition, the Arctic Region Supercomputing Center (ARSC) generously supplied the computing resources to conduct the numerical experiments.

Dr. Tom Weingartner, my major advisor and graduate committee chair provided a seemingly limitless amount of energy, guidance, oceanographic expertise and editorial skills without which this thesis and the proposals to fund the research within would not have been possible. In addition to serving as members of my graduate committee I have benefitted from discussions, expertise, guidance and/or classes with Dr. Kate Hedström (from ARSC) and Drs. Rolf Gradinger, Mark Johnson and Zygmunt Kowalik (from the UAF Institute of Marine Science). Dr. Robert Pickart, my future postdoctoral advisor at the Woods Hole Oceanographic Institute, was also instrumental in providing motivation to complete this work as well as to ski and run faster.

The regular visitors to the Oceanography Commons lunch table including, but not limited to, the staff and faculty of the UAF School of Fisheries and Ocean Sciences

Physical Oceanography Department (notably Seth Danielson and Rachel Potter) have all contributed to this research through their queries, expertise and collegiality. In addition numerous friends and family members have encouraged and supported me along the way. Finally, I would like to thank my wife, Kate Beattie for her support and companionship throughout this long process.

## Introduction

The Arctic Ocean occupies 1.5% percent of the global ocean volume and less than 5% of the surface area but receives 10% of the global freshwater runoff (Aagaard and Carmack, 1989). Though the details are largely unknown, much of the large freshwater influx into the Arctic is processed on the vast and shallow ice-covered Arctic shelves, which comprise ~ 30% of the Arctic Ocean area. Through connections between Arctic Ocean freshwater storage and global thermohaline circulation, Arctic shelves are a critical link in global climate (Proshutinsky and Johnson, 1997). Climactic feedbacks mean large-scale changes impact the smaller scales and vice versa: the Arctic Oscillation can substantially influence the transport of riverine water into the basin (Polyakov and Johnson, 2000), suggesting that climate change will likely first affect shelf ice conditions and terrestrial hydrological processes. In order to better understand possible changes in the Arctic environment and their impacts on shelf circulation, it is necessary to first understand current Arctic shelf circulation patterns and this understanding is lacking.

The Arctic's harsh environment and remote setting make year-round study of its shelves difficult and expensive. Herein we present idealized circulation models which are meant to advance our understanding of Arctic shelf circulation and, as far as possible, propose answers to questions raised by the scant observations of circulation on Arctic shelves. It is hoped these models will fill gaps in our observational knowledge and perhaps guide observational programs in this poorly understood region. We focus on the response of an idealized "interior" Arctic shelf covered by an immobile floating ice cover (landfast ice) and subject to various simple forcings. We examine the differences a

landfast ice cover introduces compared to an ice-free shelf setting. An interior Arctic shelf is one that is dominated by winds and buoyancy whereas an advective shelf is dominated by flow through (Carmack and Wassmann, 2006). Landfast ice is an immobile floating ice cover anchored to the coast that seasonally isolates most interior Arctic shelves from direct wind forcing between October and July (e.g. Macdonald and Carmack, 1991; Eicken et al., 2005).

Observations presented in Weingartner et al. (2009) from the Alaskan Beaufort Shelf Sea (ABS) show that by excluding mixing due to wind, a landfast ice cover creates a unique, low energy inner shelf environment. From top to bottom, Figure 0.1 presents ice thickness, bottom track speed (from the acoustic Doppler current profiler which indicates when the flow is wind driven and when ice covers the mooring) and current velocity from the “Dinkum” mooring deployed in 10 m of water near Prudhoe Bay (Figure 0.2). The mooring record shows that when the shelf is ice-free, flow is wind driven and current velocities can exceed  $0.5 \text{ m s}^{-1}$ . When landfast ice is present and river discharge is zero, mean subtidal flow under the ice is reduced by an order of magnitude compared to the open water season ( $< 0.05 \text{ m s}^{-1}$ ) and fluctuates along the coast so that mean along-shore transport is not significantly different from zero. Furthermore, the observations show that: 1) there is no relation between local winds and currents under the landfast ice, 2) sea level under the ice is weakly correlated with local winds, and 3) the along-shore coherence scale of the sea level is much longer than the along-shore coherence scale of under-ice current speed. The momentum balance beneath the landfast ice cover is between along-shore sea level slopes (of uncertain origin) and the frictional



coupling between the bottom and the floating landfast ice cover (Weingartner et al., 2009).

For comparison to Weingartner et al.'s (2009) observations we configured our idealized model domain to resemble the ABS. The ABS is a marginal interior Arctic shelf sea bordered to the south by the North Slope of Alaska, to the west by the Chukchi Sea and to the east by the Canadian Beaufort Sea (Figure 0.2). The ABS is a shallow, low gradient Arctic shelf sea; the width of the ABS is between 65 - 80 km, the shelfbreak is generally  $< 65$  m and bottom slope,  $s$ , is  $\sim 7.5 \times 10^{-4}$  and the latitude ( $\varphi$ , treated here as constant) is  $\sim 70^\circ$  N. The inner shelf of the ABS (depths  $< 20$  m) and of other interior Arctic shelf seas is seasonally covered by an immobile floating landfast ice cover.

In addition to excluding mixing due to wind, landfast ice exerts a stress on the surface of the ocean in the same direction as bottom stress (assuming the sign of the velocity does not change sign with depth, Weingartner et al., 2009). In the ABS, landfast ice extends 20 – 40 km offshore (Mahoney et al., 2007) and is typically present on the shelf between October and early July (Figure 0.1). At times, the landfast ice cover can extend seaward of the shelf break (Mahoney et al., 2007). Winds along the ABS are primarily upwelling-favorable year-round (Weingartner et al., 2009). In the present study we concentrate on the effect landfast ice has on inner shelf circulation during winter and spring.

Sea ice (and landfast ice in particular) is very different from the smooth bottom topography of the ABS and other interior Arctic shelves; Rothrock and Thorndike (1980) describe sea ice as rough at all scales. Variations in landfast ice thickness and roughness

are substantial and likely important to under-ice circulation; on the Beaufort Sea shelf, ice thickness and roughness generally increases with increasing distance from the coast (Tucker et al., 1979). In the Canadian Beaufort, the *stamukhi* zone, a thick line of pressure ridges that constitutes the offshore edge of the landfast ice, prevents Mackenzie River water from spreading offshore (Macdonald and Carmack, 1991). In contrast to the Beaufort, the landfast ice cover of the Laptev Shelf Sea is generally smooth and extends for large distances (up to 100 km) over the very wide and shallow Siberian Shelf (Eicken et al., 2005). Observations of cross-shore variability in ice roughness and thickness (Tucker et al., 1979) and simple scaling suggests that understanding the effects of 1) the magnitude of the ice-ocean friction coefficient and 2) the variability in the ice-ocean friction coefficient are important to understanding both buoyancy-driven and mean circulation beneath landfast ice. In general in the ABS, inshore of the *stamukhi* zone (the ~ 20 m isobath), landfast ice is thickest (> 2 m) at the onset of breakup (typically late June) and typically roughness (and thickness) increases with distance offshore.

Measurements of the ice-ocean drag coefficient suggest that variations in ice roughness affect the strength of the frictional coupling between landfast ice and the ocean. Shirasawa (1986) directly measured the ice-ocean drag coefficient beneath landfast ice in the Canadian Archipelago and found a quadratic drag coefficient of  $5 \times 10^{-3}$  (for smooth ice) while for a rough ice cover he determined the quadratic drag coefficient was  $9 \times 10^{-3}$ . McPhee (1990) reports a similar range for pack ice (mobile ice that covers the major Arctic Basins) and further notes that the drag coefficient can vary substantially within short distances. McPhee (1990) attributes these large variations to

form drag associated with deep ice keels. Since we will be working with linear friction coefficients, it is necessary to linearize the drag coefficients; we expect the linear ice-ocean friction coefficient,  $r_{ice}$ , to vary between  $10^{-4}$  and  $10^{-3} \text{ m s}^{-1}$  (see section 1.6). Weingartner et al. (2009) assumed  $r_{ice}$  to be  $O(10^{-4} \text{ m s}^{-1})$  to infer the vertically averaged momentum balance beneath the ABS landfast ice cover. Studies of topographic drag due to bottom roughness (Brink, 1986) and ice topography (Pite et al., 1995) suggest that understanding the effects of 1) the magnitude of the ice-ocean drag coefficient and 2) the variability in the ice-ocean drag coefficient are important to understanding both buoyancy driven and mean circulation beneath landfast ice. Since along- and cross-shore variations in the ice-ocean drag and variations in ice roughness could result in along-shore sea level slopes such as those reported by Weingartner et al. (2009).

In the winter circulation beneath the landfast ice cover of the ABS is weak. However, in June and July, when the seasonally frozen Arctic rivers of Alaska's North Slope begin to melt, the inner shelf environment changes very rapidly. From top to bottom, Figure 0.3 shows the climatological discharge record of the Sagavanirktok River (a small seasonally frozen river to the east of Prudhoe Bay that flows into the Alaskan Beaufort Sea), ice thickness, salinity and temperature and transmissivity through time from the Dinkum mooring that was located just offshore of the Sagavanirktok River. The Sagavanirktok River begins to melt when the landfast ice cover is thickest ( $\sim 2 \text{ m}$ ) and the ambient shelf water is at the seasonal maximum density ( $\rho \sim 1025 \text{ kg m}^{-3}$ ) due to the winter accumulation of salt on the shelf. Transmissivity decreases rapidly when the river discharge drops its accumulated load of sediment as it enters the shelf. Reports indicate

that the other Arctic Alaskan rivers follow a similar pattern (e.g. Reimnitz, 2002). Further since Arctic shelves are essentially ice-covered estuaries (e.g. Macdonald and Carmack, 1991; Eicken et al., 2005) estuarine processes in the Arctic are likely very different from mid-latitudes.

While the Arctic rivers of Alaska are seasonally frozen, larger Arctic rivers discharge into ice-covered shelves year round (Figure 0.4). Figure 0.4 shows that despite the year round flow, these large Arctic rivers exhibit a sub-inertial surge in discharge ( $> 50\%$  of the annual discharge occurs in June and July) similar to smaller Arctic rivers such as the Sagavanirktok River shown in Figure 0.3. The freshwater from these large rivers is thought to play critical roles in shelf- and basin-scale processes. Arctic rivers play an important role in upper ocean stratification (Bjork, 1989) and ventilation of the halocline (Melling, 1993) but the transport of shelf waters to the basin is poorly understood (e.g. Steele et al., 1996). Here we study idealized river inflows that mimic the relatively small rivers of the ABS though it is hoped that the results are useful in understanding how river water is processed on other Arctic shelves where large rivers flow year-round.

While there are clearly many complications which could be included in a study of Arctic shelf circulation, the primary goal of this thesis is to understand the fundamental effect the surface stress, exerted by the landfast ice cover on the ocean, has on inner shelf circulation. We investigate the effect of the landfast ice surface stress on inner shelf circulation using idealized numerical model experiments. Landfast ice is included in the models as a surface stress (there is no ice thickness) and topographic variations in the ice are considered indirectly; the effects of variability in ice roughness are studied by

allowing the linear ice-ocean friction coefficient to vary. The questions we address with our idealized models are:

- 1) What is the effect of a landfast ice cover on an along-shore sea level slope (and does the presence of an ice cover explain the differences in the along-shore coherence scales between sea level and under-ice velocities).
- 2) What is the effect of an along-shore upwelling wind blowing along an ice edge on under-ice circulation?
- 3) Can uniform along-shore winds interacting with along-shore changes in ice (including ice coverage, roughness and width) lead to along-shore sea level slopes?
- 4) How does a landfast ice cover affect a rapidly (temporally) varying buoyant discharge?

The thesis is laid out as follows: Chapter 1 is an examination of how landfast ice affects an along-shore sea level slope. Chapter 2 examines the effects of an upwelling wind offshore of the landfast ice edge. Chapter 3 is an examination of the effect of landfast ice on buoyant river discharge. The overall results are summarized in the final section; Summary and conclusions.

## *References*

- Aagaard, K., Carmack, E.C., 1989. The role of sea ice and other fresh water in the Arctic circulation. *Journal of Geophysical Research* 94 (C10), 14485-14498.
- Bjork, G., 1989. A one-dimensional time-dependent model for the vertical stratification of the upper Arctic Ocean. *Journal of Physical Oceanography* 19 (1), 52-67.
- Brink, K.H., 1986. Topographic drag due to barotropic flow over the continental shelf and slope. *Journal of Physical Oceanography* 16 (12), 2150-2158.
- Carmack, E., Wassmann, P., 2006. Food webs and physical-biological coupling on pan-Arctic shelves: Unifying concepts and comprehensive perspectives. *Progress In Oceanography* 71 (2-4), 446-477.
- Eicken, H., Dmitrenko, I., Tyshko, K., Darovskikh, A., Dierking, W., Blahak, U., Groves, J., Kassens, H., 2005. Zonation of the Laptev Sea landfast ice cover and its importance in a frozen estuary. *Global and Planetary Change* 48 (1-3), 55-83.
- Macdonald, R.W., Carmack, E.C., 1991. The role of large-scale under-ice topography in separating estuary and ocean on an Arctic shelf. *Atmosphere-Ocean* 29 (1), 37-53.
- Mahoney, A., Eicken, H., Shapiro, L., 2007. How fast is landfast sea ice? A study of the attachment and detachment of nearshore ice at Barrow, Alaska. *Cold Regions Science and Technology* 47 (3), 233-255.
- McPhee, M.G., 1990. Small scale processes, in: Smith, W.C. (Ed.), *Polar Oceanography Part A Physical Science*. Academic Press, New York, pp. 287-334.
- Melling, H., 1993. The formation of a haline shelf front in wintertime in an ice-covered Arctic sea. *Continental Shelf Research* 13 (10), 1123-1147.

- Pite, H.D., Topham, D.R., van Hardenberg, B.J., 1995. Laboratory measurements of the drag force on a family of two-dimensional ice keel models in a two-layer flow. *Journal of Physical Oceanography* 25 (12), 3008-3031.
- Polyakov, I.V., Johnson, M.A., 2000. Arctic decadal and interdecadal variability. *Geophysical Research Letters* 27 (24), 4097-4100.
- Proshutinsky, A.Y., Johnson, M.A., 1997. Two circulation regimes of the wind-driven Arctic Ocean. *Journal of Geophysical Research* 102 (C6), 12493-12514.
- Reimnitz, E., 2002. Interactions of river discharge with sea ice in proximity of Arctic deltas: a review. *Polarforschung* 70, 123-134.
- Rothrock, D.A., Thorndike, A.S., 1980. Geometric properties of the underside of sea ice. *Journal of Geophysical Research* 85 (C7), 3955-3963.
- Shirasawa, K., 1986. Water stress and ocean current measurements under first-year sea ice in the Canadian Arctic. *Journal of Geophysical Research* 91 (C12), 14305-14316.
- Steele, M., Thomas, D., Rothrock, D., Martin, S., 1996. A simple model study of the Arctic Ocean freshwater balance, 1979-1985. *Journal of Geophysical Research* 101 (C9), 20833-20848.
- Tucker, W.B., III, Weeks, W.F., Frank, M., 1979. Sea ice ridging over the Alaskan continental shelf. *Journal of Geophysical Research* 84 (C8), 4885-4897.
- Weingartner, T.J., Danielson, S., Sasaki, Y., Pavlov, V., Kulakov, M., 1999. The Siberian Coastal Current: A wind- and buoyancy-forced Arctic coastal current. *Journal of Geophysical Research* 104 (C12), 29697-29713.

Weingartner, T.J., Danielson, S.L., Kasper, J.L., Okkonen, S.R., 2009. Circulation and water property variations in the nearshore Alaskan Beaufort Sea (1999-2007). US Dept. of Interior, Minerals Management Service, Alaska Outer Continental Shelf Region, Anchorage, Alaska, p. 154.



## Figures

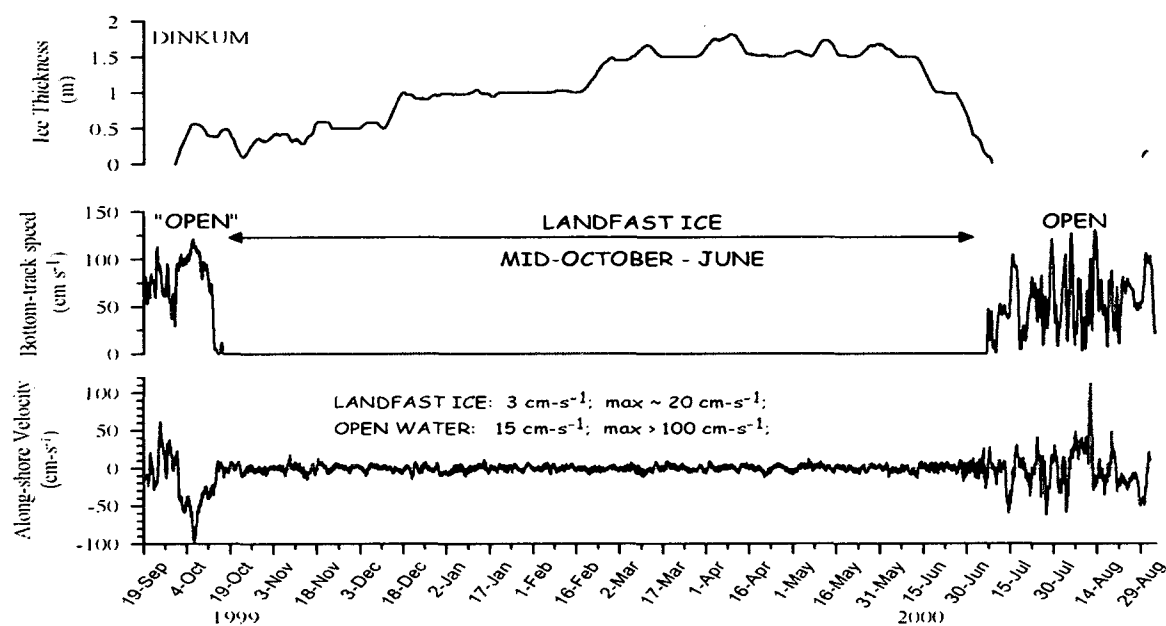


Figure 0.1. Two seasons: the seasonal cycle of the Alaskan Beaufort Sea shelf. From top to bottom: ice thickness (m), surface velocity ( $\text{cm s}^{-1}$ ) from the ADCP bottom track feature and along-shore velocity ( $\text{cm s}^{-1}$ ) versus time (months). Observations are from the Dinkum mooring and are described in detail in Weingartner et al. (2009).

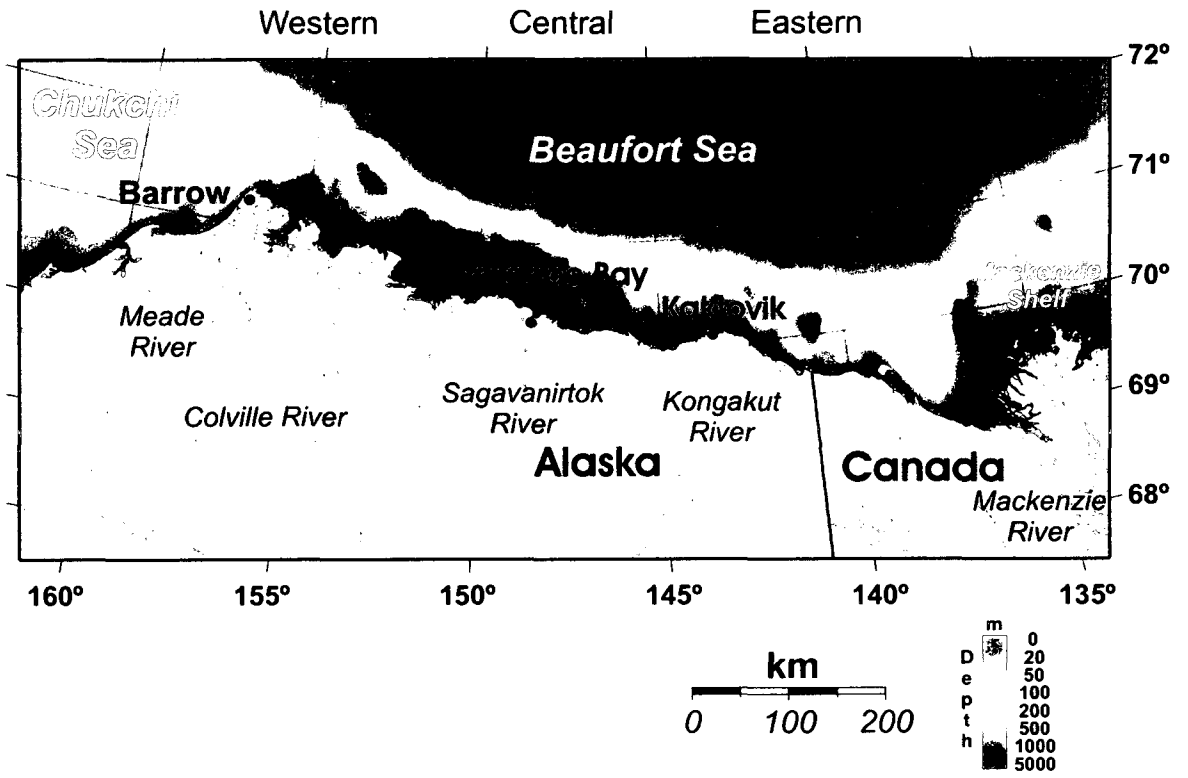


Figure 0.2. Map of the Alaskan Beaufort Sea and of the North Slope of Alaska.

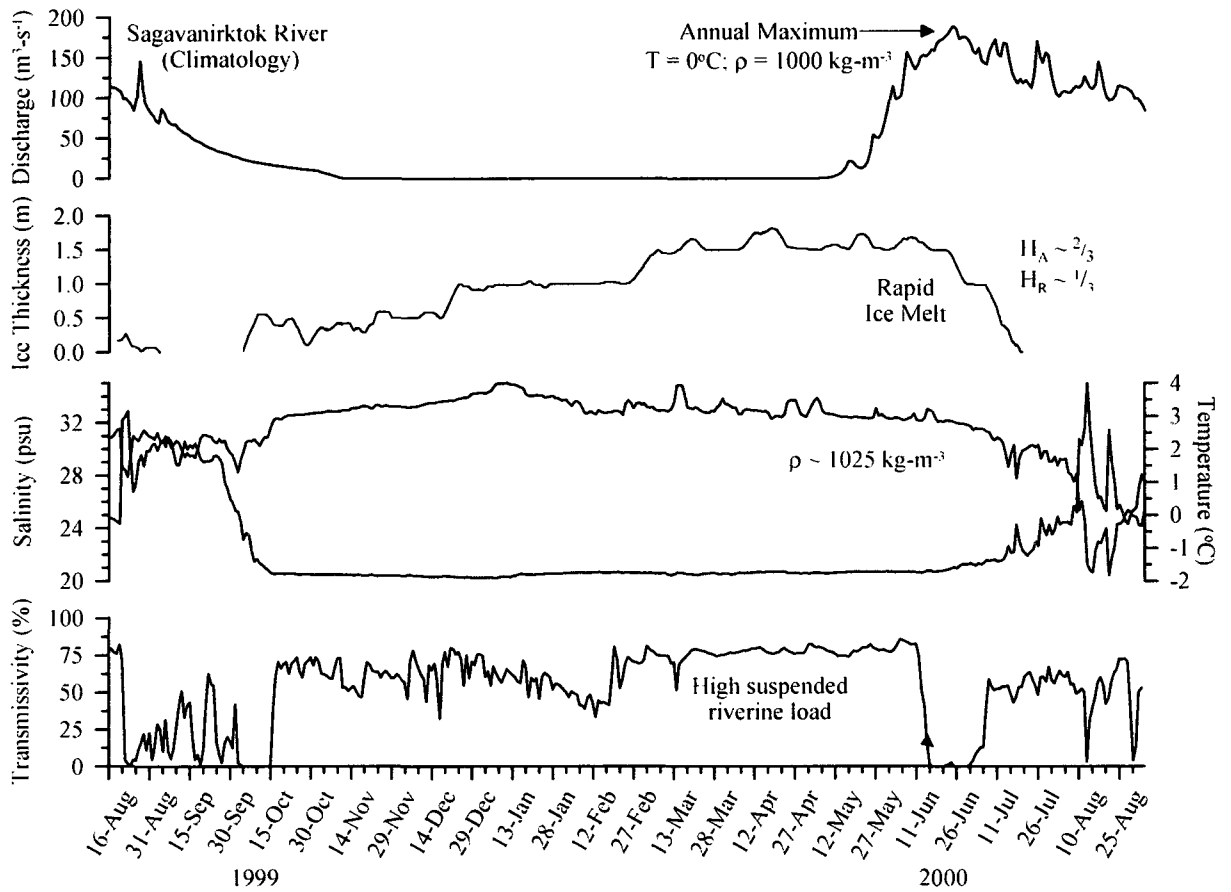


Figure 0.3. Spring conditions on an Arctic shelf sea. Description is based on *pers. comm.* with Weingartner. From top to bottom: the climatological discharge of the Sagavanirktok River ( $\text{m}^3 \text{s}^{-1}$ ), ice thickness (m), near bottom salinity (psu) and temperature ( $^{\circ}\text{C}$ ) and transmissivity (%) versus time (months).

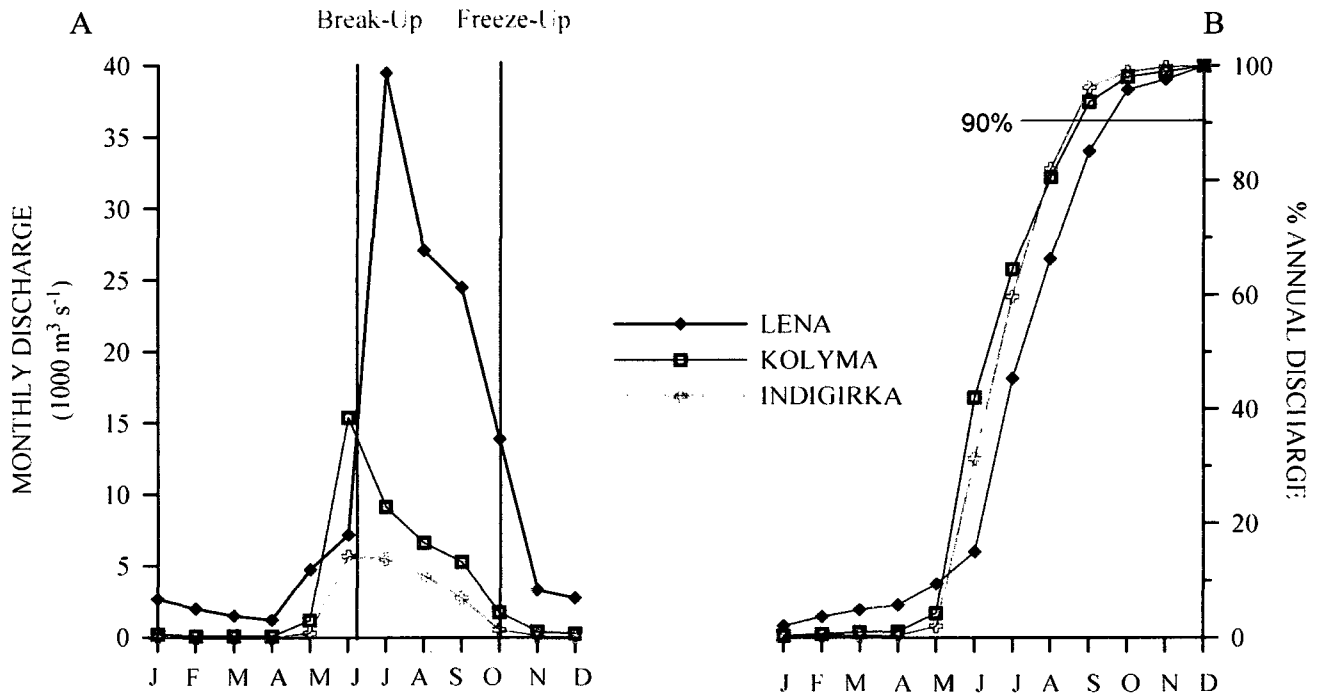


Figure 0.4. The spring freshet. A) Climatological discharge ( $10^3 \text{ m}^3 \text{ s}^{-1}$ ) of the Lena, Kolyma and Indigirka rivers versus month. B) Cumulative annual discharge of the same three rivers versus month. Breakup and freeze up dates based on Weingartner et al. (1999).

## **Chapter 1 The effect of landfast ice on a lateral inflow to a shelf sea<sup>1</sup>**

### *Abstract*

Due to an immobile landfast ice cover in winter, under-ice circulation along Arctic shelf seas is influenced by frictional drag at both the surface and bottom. We use both simple analytical and numerical models (based on the “arrested topographic wave” or ATW) to understand how this frictional coupling may control the mean flow within the landfast ice zone. Herein we examine how the arrested landfast ice topographic wave model (ALW) describes how frictional effects in the landfast ice zone affect lateral inflow along the western boundary of a shelf sea similar to the Alaskan Beaufort Sea. All models (numerical, the ALW and the ATW) show that due to the presence of bottom friction and the additional frictional coupling between the landfast ice and the ocean, a velocity signal due to an elevated sea level will not be coherent at large distances from the source, although sea level may be. Thus observations of currents beneath the landfast ice cover near Prudhoe Bay, ~ 300 km east of Barrow Canyon will probably show no relation between currents in the vicinity of Barrow. However, currents within about 50 km of Barrow may be coherent with the flow in Barrow Canyon. Further, results suggest that proper interpretation of current observations beneath landfast ice requires knowledge of the ice width, the magnitude of the ice-ocean friction coefficient, and spatial variations

---

<sup>1</sup> Kasper, J.L., Weingartner, T.J., The effect of landfast ice on a lateral inflow to a shelf sea, prepared for submission to Continental Shelf Research.

in this coefficient, since these affect the vorticity balance of shallow landfast ice-covered shelves.

## ***1.1 Introduction***

Winds and river runoff influence the dynamics and circulation over the innermost portion (water depths  $< \sim 20$  m) of most continental shelves. While this is true for Arctic shelves as well, observations from the Alaskan Beaufort Sea shelf show that the effects of winds and buoyancy are substantially modulated by the annual freeze/thaw cycle, which controls the phasing and duration of the sea ice season and river discharge (Weingartner et al., 2009). The focus of this paper is on the control that landfast ice may have on under-ice circulation. Landfast ice, common to most Arctic shelves in winter, extends from the coast offshore to between the 20 and 40 m isobaths. It persists from October through June (Macdonald and Carmack, 1991; Reimnitz, 2002) and because it is effectively immobile, inhibits the direct air-sea transfer of momentum.

The Alaskan Beaufort Sea landfast ice cover encompasses  $\sim 20$ -25% of the shelf area. Landfast ice is a prominent feature of the Mackenzie Beaufort shelf and the broad Eurasian shelf seas and covers a similar fraction of the area of these shelves as well. Its effects on the seasonal variation in circulation are pronounced. When present, nearshore (under-ice) currents are weak ( $< 0.05$  m s<sup>-1</sup>), variable, and uncorrelated with wind and sea level fluctuations (Weingartner et al., 2009). In contrast, when landfast ice is absent, currents are swift ( $\sim 0.20 - 1.00$  m s<sup>-1</sup>) and both currents and sea-level are coherent with one another and the local winds.

The observations suggest that to first-order the circulation beneath the landfast ice is controlled by time-varying along-shore pressure gradients ( $O[10^{-6} \text{ m s}^{-2}]$ ) and frictional coupling of the currents to the seabed and to the sea ice (Weingartner et al., 2009). The origin of the pressure gradients is unknown but these likely arise due to remote processes associated with larger scale wind or ocean circulation fields. Herein, we modify conceptual models of shallow shelf seas in a preliminary examination of the dynamics of shallow, landfast ice-covered Arctic shelf seas.

The along- and cross- shore variability of landfast ice are poorly known but the roughness characteristics of sea ice (Rothrock and Thorndike, 1980) are such that the ice-ocean drag coefficient may vary by at least an order of magnitude within several kilometers. Furthermore, skin friction, form drag and internal wave mixing all contribute to frictional stress at various times and locations throughout the Arctic (McPhee, 1990). On the Alaskan Beaufort shelf, Tucker et al.'s (1979) observations suggest that landfast ice thickness and ridging intensity varies throughout winter in both the along- and cross-shore directions and Mahoney et al. (2007) show that the cross-shore width of landfast ice can vary along-shore. Hence we expect similar spatial variations in the frictional coupling between the ocean and ice. Herein we ignore the complexities of the landfast ice and simply include its effect on ocean circulation indirectly by imposing a stress on the surface of the ocean exactly analogous to a bottom drag. Along- and cross-shore landfast ice variability is parameterized by specifying a linear ice-ocean friction coefficient that may vary in both the along- and cross-shore direction, i.e.  $r_{ice} = r_{ice}(x, y)$ .

While the Alaskan Beaufort shelf is typically covered by landfast ice during winter, freely drifting ice and/or polynas typically occur over Barrow Canyon along the western boundary of the Beaufort shelf. The Alaskan Coastal Current flows along the canyon toward the northeast, on average drawing water from the Chukchi shelf and transporting it onto the shelfbreak (Mountain et al., 1976; Weingartner et al., 1998; Pickart et al., 2010) and, at least occasionally, onto the Beaufort shelf (Okkonen et al., 2009). In the model setting described below, this inflow is mimicked by imposing a cross-shelf sea surface slope along the western boundary of a shallow shelf partially covered by landfast ice.

The outline of the paper is as follows: In Section 1.2 we use the steady shallow water equations to derive and analytically solve a vorticity equation that incorporates surface stress via frictional coupling between the landfast ice and the under-ice flow. The formulation follows Csanady's (1978) ATW model and describes the effects of bottom friction, landfast ice, and a sloping bottom on an imposed cross-shore sea level slope at the western boundary. In Section 1.3 idealized process numerical results are discussed that include processes that the analytic model cannot incorporate; the surface stress curl across the landfast ice edge and the area offshore of the landfast ice cover. As in the analytical results, numerical experiments are driven by a lateral inflow, an elevated sea level at the western boundary. Section 1.4 is a discussion of the similarities and differences between the analytic and numerical results, while Section 1.5 concludes and summarizes the paper.



## 1.2 The analytic model

We apply the steady state shallow water equations under the long-wave approximation to a long, straight coastline with the  $x$ -axis at the coast and  $y$  increasing offshore (Figure 1.1). The along-shore domain is such that  $x \geq 0$ . Landfast ice extends from the coast ( $y = 0$ ) offshore to a distance  $y = L$ . Depth,  $h(y) = h_0 + sy$ , is a function of offshore distance,  $y$ , only and  $s$  is the constant bottom slope ( $s = 7.5 \times 10^{-4}$ , similar to the bottom slope on the Alaskan Beaufort shelf and  $h_0 = 1$  m is the depth at the coast). The model domain represents the area covered by landfast ice—the northern boundary is the seaward extent of the landfast ice cover. Linear bottom friction is assumed proportional to the depth-averaged transport, and surface stress between landfast ice and the ocean is parameterized similarly. Note in actuality water depth may vary both with offshore distance and the thickness of landfast ice, though for simplicity we assume that landfast ice thickness is constant. We force the model by specifying a sea surface height distribution at the western boundary, analogous to the “mound of water” examined by Csanady (1978). The “mound” at the western boundary represents the accumulated effects of wind forcing or mean flow over the “backward” portion of the coast ( $x < 0$ ). With these assumptions the governing equations are:

$$\left. \begin{aligned} -fv &= -g \frac{\partial \eta}{\partial x} - B_x - S_x \\ fu &= -g \frac{\partial \eta}{\partial y} - B_y - S_y \\ \frac{\partial(uh)}{\partial x} + \frac{\partial(vh)}{\partial y} &= 0 \end{aligned} \right\} \quad 1.1$$

where  $u$  and  $v$  are the along- and cross-shore velocities ( $\text{m s}^{-1}$ ) respectively,  $\eta$  is the sea level anomaly (m),  $g$  is the acceleration due to gravity ( $\text{m s}^{-2}$ ),  $f$  the Coriolis parameter (latitude  $70^\circ \text{ N}$ ,  $f = 1.37 \times 10^{-4} \text{ s}^{-1}$ ) and  $h$  is the depth (m) given above.  $B$  and  $S$  are the bottom and surface (due to landfast ice) stresses, respectively. Note that both terms have the same sign since these stresses oppose the interior flow. Following Csanady (1978), we neglect the cross-shore stress terms,  $B_y$  and  $S_y$ , as small compared to the larger along-shore stress components. Numerical results presented later show that except within  $\sim 5$  km of the western boundary this assumption is valid in our idealized setting. Setting the along-shore bottom and surface stresses equal to the vertically averaged transport yields:

$$\left. \begin{aligned} -fv &= -g \frac{\partial \eta}{\partial x} - \frac{(r_{ice} + r_b)u}{h} \\ fu &= -g \frac{\partial \eta}{\partial y} \\ \frac{\partial(uh)}{\partial x} + \frac{\partial(vh)}{\partial y} &= 0 \end{aligned} \right\} \quad 1.2$$

where  $r_{ice}$  and  $r_b$  are the surface and bottom friction coefficients, respectively. The first and second equations of 1.2 are the along- and cross-shore momentum balances, respectively, while the third is the continuity equation.

Upon taking the curl of the momentum equations and substituting from the continuity equation, we form a vorticity equation (the arrested landfast ice topographic wave, ALW) in terms of the sea level anomaly,  $\eta$ :

$$\frac{\partial \eta}{\partial x} = \frac{1}{fs} \frac{\partial}{\partial y} \left( (r_{ice} + r_b) \frac{\partial \eta}{\partial y} \right) = \underbrace{\frac{(r_{ice} + r_b)}{fs} \frac{\partial^2 \eta}{\partial y^2}}_{\text{Term 1}} + \underbrace{\frac{1}{fs} \frac{\partial(r_{ice} + r_b)}{\partial y} \frac{\partial \eta}{\partial y}}_{\text{Term 2}} \quad 1.3$$

The left side of equation 1.3 is the along-shore sea level slope and it varies in part due to vortex stretching associated with the product of the Coriolis parameter ( $f$ ) and bottom slope ( $s$ ). Note that analytical simplicity requires that we treat the surface and bottom stresses as a single term. Thus in our analysis we allow the sum of the friction coefficients, ( $r_{ice} + r_b$ ), to vary with  $x$  and  $y$ . Since the model is vertically averaged the separation of the surface and bottom stresses is meaningless though conceptually we make the distinction that we are using the ALW vorticity equation to study the effects of spatial variations in under-ice friction.

The ALW vorticity equation is similar to Csanady's (1978) ATW vorticity equation, a simple parabolic, diffusion equation,  $\frac{\partial \eta}{\partial x} = \frac{r_b}{fs} \frac{\partial^2 \eta}{\partial y^2}$  where the diffusion coefficient,  $r_b/fs$ , is constant, the along-shore distance,  $x$ , assumes the role of the time-like coordinate, and wind forcing enters through the coastal boundary condition as in Gill and Schumann (1974). Equation 1.3 is also a parabolic diffusion equation although the diffusivity may vary both spatially and in the time-like  $x$  coordinate. Expansion of the partial derivative in the middle of equation 1.3, leads to the two terms on the far right. Term 1 is the ATW-like term. The diffusion coefficient, which may vary in both  $x$  and  $y$ , is the sum of the under-ice and bottom friction coefficients divided by  $fs$ . As in the ATW, diffusion is proportional to the cross-shore divergence of the along-shore geostrophic velocity (a vortex contraction term). Term 2 is the cross-shore gradient in ice friction multiplied by the along-shore geostrophic transport. It behaves like the advection term in an advective-diffusive differential equation and results in vortex contraction. The

advective-like velocity is thus the gradient in ice-ocean drag divided by  $fs$ . For our setting we take the gradient in the ice-ocean friction coefficient,  $\partial(r_{ice} + r_b)/\partial y$ , to be positive since the Alaskan Beaufort landfast ice cover is generally smoother near shore and rougher due to increased ridging farther offshore (Tucker et al., 1979). In our model this effect is represented by an increase in  $r_{ice}$  moving offshore. Observational evidence suggests that this parameterization is not unrealistic although there are other considerations discussed later that may be important as well (Shirasawa, 1986; McPhee, 1990). The ALW vorticity balance requires that an increase in diffusion or advection be balanced by an increase in along-shore sea level slope. It also shows that changes in under-ice friction lead to along- and cross-shore variation in the cross-shore divergence of the along-shore geostrophic transport.

With assumed values of the parameters  $(r_{ice} + r_b) \sim 10^{-3} \text{ m s}^{-1}$ ,  $L \sim 20 \text{ km}$ ,  $\partial^2 \eta / \partial y^2 \sim 10^{-10} \text{ m}^{-1}$ ,  $\partial \eta / \partial y \sim 10^{-6}$ ,  $\partial(r_{ice} + r_b) / \partial y \sim 10^{-7} \text{ s}^{-1}$ , scaling the terms of the ALW vorticity equation shows that terms 1 and 2 contribute equally to the balance. For certain simple choices of the along- and cross-shore variation of the ice-ocean friction coefficient the vorticity equation (eq. 1.3) is analytically tractable.

### 1.2.1 Solution by separation of variables

We outline the basic solution procedure below and leave the details to the Appendix. We first set  $\eta = X(x)Y(y)$ , assume that

$$(r_{ice} + r_b) = A \times [C_0 + C_1 \sin(mx)](C_2 + C_3 y)^2 \quad 1.4$$

and substitute into the ALW vorticity equation (eq. 1.3), which then separates. The constants  $C_0, C_1, C_2, C_3$  and  $m$  describe the magnitude and variability of the ice-ocean friction coefficient and in the basic case are chosen so that  $r_{ice} + r_b \sim O(10^{-4} \text{ m s}^{-1})$ . In the basic case,  $A$  is 1. The analytical and numerical models are used to test the sensitivity of the under-ice circulation to these parameters and to the landfast ice width. The range of constants considered for the analytical and numerical models is listed in Table 1.1. Figure 1.2, a plot of  $(r_{ice} + r_b)$ , provides a sense of the range of parameters considered. For small values of  $C_3$  the friction coefficient is nearly constant across the shelf. Consequently, the advective-like term 2 is an order of magnitude less than the diffusive-like vorticity term 1, whereas for larger values of  $C_3$  ( $> \sim 10^{-5}$ ) the two vorticity terms are similar in magnitude.

The separated ordinary differential equations for  $X$  and  $Y$  are:

$$\begin{aligned} \lambda C_3^2 Y &= \frac{d}{dy} \left( (C_2 + C_3 y)^2 \frac{dY}{dy} \right) \\ \lambda C_3^2 X [C_0 + C_1 \sin(mx)] &= fs \frac{dX}{dx} \end{aligned} \tag{1.5}$$

where the separation constant,  $\lambda$ , is an eigenvalue. The  $Y$  equation is similar to the ordinary differential equation satisfied by the radial component of Laplace's equation in spherical coordinates. More generally, it is a nonlinear Euler-Cauchy type second-order ordinary differential equation of the Sturm Liouville form (e.g. Boas, 1983). A solution is found upon substituting  $Y = (C_2 + C_3 y)^\alpha$ . The resulting quadratic characteristic equation for  $\alpha$  allows for real repeated, distinct real, and complex conjugate roots. Application of the boundary conditions shows that  $\alpha$  is a set of complex conjugates so that the solution

takes the form given below (eq. 1.6) with eigenvalues,  $\lambda$ , less than  $-1/4$ . The equation for  $X(x)$  is a simpler first-order ordinary differential equation and can be solved by direct integration.

The solution to the ALW vorticity equation for  $\eta$  (from the Appendix), is:

$$\eta = \sum_{\lambda} A_{\lambda} \underbrace{\frac{\sin\left(\sqrt{-\frac{1}{4} - \lambda} \ln(C_2 + C_3 y) + \varphi\right)}{(C_2 + C_3 y)^{\frac{1}{2}}}}_{\text{Cross-Shore term}} \underbrace{\exp\left[\frac{\lambda}{fs} \left(C_0 x - \frac{C_1}{m} \cos(mx)\right) C_3^2\right]}_{\text{Along-Shore Term}} \quad 1.6$$

where the constants  $A_{\lambda}$ ,  $\lambda$  and  $\varphi$  are determined by the initial condition (the inflow at  $x = 0$ ) and boundary conditions discussed next. The cross-shore term is a summation of sinusoids with coefficients chosen to satisfy the initial condition. The along-shore term decays exponentially in  $x$ : since for non-zero real solutions to exist  $\lambda < -1/4$ . In contrast to the ALW solution, the ATW solution, shown below in closed form, is a Gaussian distribution (Csanady, 1978):

$$\eta = \frac{1}{(4\pi\kappa x)^{1/2}} \int_0^{\infty} \eta_0(s) \left[ \exp\frac{(y-s)^2}{4\kappa x} + \exp\frac{(y+s)^2}{4\kappa x} \right] ds \quad 1.7$$

where  $\eta_0$  is the initial condition.

### 1.2.1.1 Boundary conditions

Since the ALW vorticity equation, eq. 1.3, is second order in the cross-shore direction ( $y$ ) and first-order in the along-shore direction, two boundary conditions are needed for the cross-shore direction and one for the along-shore direction.

The cross-shore boundary conditions are applied at the coast ( $y = 0$ ) and at the ice edge ( $y = L$ ). At the coast, the cross-shelf transport is zero. Hence from the first of equations 1.2 we have:

$$(r_{ice} + r_b)u = -gh_0 \frac{\partial \eta}{\partial x} \quad 1.8$$

At the coast there is a balance between the along-shore surface and bottom stresses and the along-shore sea level slope. Substituting  $u = -\frac{g}{f} \frac{\partial \eta}{\partial y}$  (cross-shore geostrophy) into

eq. 1.8 we have:

$$\left. \frac{\partial \eta}{\partial y} \right|_{y=0} = \frac{fh_0}{(r_{ice} + r_b)} \left. \frac{\partial \eta}{\partial x} \right|_{y=0} \quad 1.9$$

Thus, beneath a landfast ice cover the coastal constraint implies that an imposed along-shore sea level slope results in a cross-shore sea level slope at the coast. The magnitude of the cross-shore sea level slope depends upon both the bottom and landfast ice friction.

The cross-shore boundary condition at the ice edge,  $y = L$ , is that the pressure field is continuous at the edge of the domain (e.g. Buchwald and Adams, 1968). Hence, at the ice-edge:

$$\left. \frac{\partial \eta}{\partial y} \right|_{y=L} = 0 \quad 1.10$$

where  $L$  is the landfast ice width. Inspection of the cross-shore momentum equation (the second of eqs. 1.2) reveals that this boundary condition implies the along-shore transport at the ice edge is zero. Hence any transport at the ice-edge is entirely offshore and

perpendicular to the ice edge. In contrast, the ATW boundary condition is that the sea level decays to zero far from the coast.

Comparisons between analytical and numerical results show that our analytical offshore boundary condition causes unreasonably large values of offshore transport at the ice edge. As a result, the analytical solution is overly sensitive to ice width as well as to the ice parameters that affect cross-shore transport. While other boundary conditions (considered in section 1.4) are analytically intractable, the physical nature of the landfast ice edge complicates the choice of offshore boundary condition as well. For now, we ignore these complications and proceed with the boundary condition of a continuous sea level at the ice edge because this choice allows us to solve for the sea level anomaly,  $\eta$ , and gain some understanding of the effects of a landfast ice cover on ocean circulation. As Brink and Allen (1998) noted the ATW offshore boundary condition is also problematic, though for different reasons. As discussed below, the difference in boundary conditions is very important to the behavior of the analytical and numerical solutions.

Taken together, the coastal boundary condition and the offshore boundary condition imply that  $\varphi$  in eq. 1.6 is:

$$\varphi = \arctan \left( 2 \sqrt{\left( -\frac{1}{4} - \lambda \right)} \right) - \sqrt{-\frac{1}{4} - \lambda} \ln(C_2 + C_3 L) - n\pi \quad 1.11$$

where  $n = 0, 1, 2, 3, \dots$ . The eigenvalues,  $\lambda$ , are also determined by the cross-shore boundary conditions (see Appendix), which result in the following equation:



$$\arctan \left( \frac{2\sqrt{-\frac{1}{4}-\lambda}}{\left[ h_0 \frac{\lambda}{s} 2C_3 (C_2)^{-1} + 1 \right]} \right) - \arctan \left( 2\sqrt{-\frac{1}{4}-\lambda} \right) = \sqrt{-\frac{1}{4}-\lambda} \left[ \ln(C_2) - \ln(C_2 + C_3 L) \right] + (l-n)\pi \quad 1.12$$

from which  $\lambda$  is determined. Table 1.2 lists several values for  $\lambda$ . Note that  $\lambda$  decreases rapidly with  $l-n$ .

### 1.2.1.1.1 Initial condition

Since there is no wind stress at the coast, a vorticity source term must be specified at either the along-shore or offshore boundary. Vorticity can be supplied by specifying either  $\eta$ ,  $\frac{\partial \eta}{\partial x}$  or  $\frac{\partial \eta}{\partial y}$ . The case examined here, the ‘‘mound’’ example of the ATW, is for a positive sea level anomaly,  $\eta$ , specified at the western boundary ( $x = 0$ ). In keeping with the diffusion equation analogy, we refer to the along-shore boundary condition as the initial condition. The flow then enters the domain through an along-shore geostrophic transport. Though not discussed, here a negative sea level at  $x = 0$ , a sink, results in flow in the opposite direction (upstream in the Kelvin wave sense). In a separate paper (Chapter 2 of this thesis) we discuss the response to a sea level imposed at the seaward landfast ice edge, which arises in response to up- (or down-) welling winds blowing along and offshore of the landfast ice edge (Chapter 2 of this thesis).

To aid comparison between the analytical ALW model, the ATW solution, and numerical results, the initial condition is the same in all cases, i.e.,  $\eta(0, y) = e^{-y/2000}$  (with

$y$  in meters), which is a mound of water tightly constrained to the coast. In this case, the coefficients,  $A_\lambda$ , (see Appendix) are:

$$A_\lambda = \frac{1}{\|Y_\lambda\|^2} \exp \left\{ \frac{\lambda}{fs} \frac{C_1 C_3^2}{m} \right\} \int_0^L e^{-y/2000} \frac{\sin \left( \sqrt{-\frac{1}{4} - \lambda \ln(C_2 + C_3 y)} + \varphi \right)}{(C_2 + C_3 y)^{1/2}} dy \quad 1.13$$

where

$$\|Y_\lambda\|^2 = \int_0^L \frac{\sin^2 \left( \sqrt{-\frac{1}{4} - \lambda \ln(C_2 + C_3 y)} + \varphi \right)}{(C_2 + C_3 y)} dy. \quad 1.14$$

Eq. 1.13 is integrated using the Matlab® symbolic toolbox using the values of  $C_0$ ,  $C_1$ ,  $C_2$ ,  $C_3$  and  $m$  given in Table 1.1 (for the basic analytical solution). The full solution (using the first eight eigenfunctions) is shown in Figure 1.3A. The seaward edge of the landfast ice domain is 26 km offshore and corresponds to the 20 m isobath for the specified bottom slope and a depth of 1 m at the coast. The solution to the ATW vorticity equation with  $r_b = 2 \times 10^{-4} \text{ m s}^{-1}$  (to simulate under-ice and bottom friction) is shown in Figure 1.3B and the ATW solution with  $r_b = 10^{-4} \text{ m s}^{-1}$  (to simulate bottom friction alone) is shown in Figure 1.3C. Note that both the ALW and ATW solutions are such that the magnitude of the sea level at the western boundary only affects the magnitude of the sea level contours and not the eigenvalues. Hence comparisons between solutions (numerical and analytic) are easily carried out.

There are substantial differences between the ALW and the ATW solutions. For example, the distance that the 0.1 contour extends along-shore between the ALW and the ATW solutions shows that the ALW predicts that sea level decays to 10% of its western

boundary value by  $x \sim 35$  km, whereas the ATW solutions decay to this level by 65 km (with  $r_b = 2 \times 10^{-4} \text{ m s}^{-1}$ ) and  $\geq 100$  km (with  $r_b = 10^{-4} \text{ m s}^{-1}$ ). Sea-level isopleths near the source are more compact in the ALW solution implying greater velocities near the source than in either ATW solution. The along-shore sea level distribution reflects the Gaussian ATW solution as opposed to the decaying exponential ALW solution. The maximum offshore distance of the 0.1 contour is  $\sim 10$  km for both ATW solutions but only  $\sim 5$  km for the ALW. The zero contour is visible in the ALW solution but not in either ATW solutions (the zero contour lies along the western boundary in both ATW solutions). In the ALW solution the zero contour approaches the offshore boundary and becomes perpendicular to this boundary for large along-shore distances. This is consistent with the behavior imposed by the offshore boundary condition. The ATW solution shows that large values of diffusion (large friction coefficients) lead to large along-shore sea level slopes. The slightly more complex ALW solution shows that a different offshore boundary condition and the inclusion of spatial variations in friction (variable diffusivity) lead to larger along-shore sea level slopes than the constant diffusivity ATW solution predicts for similar friction coefficient magnitudes.

Figure 1.4 shows the effects of the ice width and changes in the ice-ocean drag parameters on  $\eta$ . For comparison the basic ALW solution is given in Figure 1.4A. For wider landfast ice covers (Figure 1.4B, ice width,  $L = 60$  km), the along-shore sea level slope is smaller, but the inflow spreads more broadly in both the along- and cross-shore directions. For narrower ice widths the flow is forced offshore by the boundary condition and the along-shore sea level slope increases. The ALW solution with a wide ice cover

(Figure 1.4B) resembles the ATW solutions (Figure 1.3C and 1.3D) more closely than the ALW solution with a narrower ice cover (Figure 1.4A).

The ALW solutions shows that for larger values of the friction coefficient (eq. 1.4 with  $A > 1$  and the remaining constants as given for the basic ALW solution) and values of  $C_0 > 10^{-2}$  (where  $C_0$  is the constant portion of the friction coefficient) the mound spreads farther offshore and not as far along the coast (the along-shore sea level slope increases). Hence the ALW solution, not unexpectedly, is similar to the ATW.

Whereas the overall magnitude of the ice-ocean frictional coupling (and of  $C_0$ , the constant portion of the friction coefficient) affects the solution, changes in  $C_1$  and  $m$  have little effect. The effects of variations in the cross-shore spatial structure of the frictional term (in terms of  $C_2$  and  $C_3$ ) are examined in Figures 1.4C and 1.4D. The assumed form of the ice-ocean friction coefficient (eq. 1.4) yields a tight coupling between the two ALW vorticity terms. Recall that both vorticity terms are vortex contraction terms; term 1 is diffusive-like and term 2 is advective-like. Thus changes in the ice-ocean friction constants ( $C_1$ - $C_3$ ) introduce changes to both vorticity terms. Examination of Figures 1.4C and 1.4D shows that larger values of the advective-like vorticity term tend to broaden the distribution along the coast, whereas larger values of the diffusive-like term cause the sea level distribution to broaden offshore; in panel c the diffusive-like term is  $\sim 8$  times the advective-like term and in panel d the two vorticity terms are of similar magnitude. Similarities and differences between the ALW and ATW are discussed further in regards to the numerical results, which show that the variable landfast ice cover introduces changes to the vorticity balance but the changes are not as dramatic as suggested by

Figure 1.4. Despite the complexity, Figure 1.4 helps to understand the effects of various parameters on the solution.

We can construct a transport stream-function ( $uh = \partial\psi/\partial y$  and  $vh = -\partial\psi/\partial x$ ) from the continuity equation, the last of eqs. (1.2). The stream-function, derived in the appendix, is:

$$\psi = -\frac{g}{f} \sum_{\lambda} \left( hY + \frac{(C_2 + C_3 y)^2}{\gamma} \frac{dY}{dy} \right) X_0^{\infty} - \frac{g}{f} \int_0^L h \frac{\partial \eta}{\partial y} dy \quad 1.15$$

where  $X(x)$  and  $Y(y)$  are the solutions to the separated governing equation and

$\gamma = (\lambda / fs) C_3^2$ . Transport streamlines are shown in Figure 1.5. The effect of the offshore boundary condition on the transport is clearly visible in Figure 1.5a, which shows transport streamlines for the basic analytical ALW solution. Figure 1.5b shows transport streamlines for the same constants except with  $L = 60$  km.

The ALW solution predicts that along-shore velocities decay to  $\sim 10\%$  of their initial value within 25 km of the western boundary and to  $\sim 5\%$  within 50 km. For a sea level anomaly of 1 cm at the western boundary (with the exponential initial condition above), the along-shore velocity at the western boundary is  $0.35 \text{ m s}^{-1}$ , similar to the velocity scale of the Alaskan Coastal Current in Barrow Canyon (Weingartner et al., 1998). Fifty (100) km east of the western boundary the along-shore velocity is  $\sim 0.02$  ( $0.005$ )  $\text{m s}^{-1}$ . The decay scale of the analytical model is similar to numerical results discussed below.

As well as illustrating the effect of the second vorticity term, Figures 1.3-1.5 underscore the importance of the offshore boundary condition on the behavior of the

solution. Because the ATW offshore boundary condition requires that the sea level anomaly decays far from the coast, the domain width is not a part of the ATW model. In contrast, the domain width, e.g., the width of the landfast ice,  $L$ , partially determines the eigenvalues for the ALW solution via equations 1.10-1.12. Whereas the ATW boundary condition is physically problematic because it leads to discontinuities offshore (Brink and Allen, 1998), the boundary condition used here is also problematic because the narrow domain (the landfast ice-covered inner shelf) combined with the offshore boundary condition leads to excessive offshore transport. Previous authors have noted that for wind-driven flow along ice edges (e.g. Clarke, 1978 and Fennel and Johannessen, 1998) the transition between landfast ice-covered and ice-free water causes a surface stress curl similar to that encountered at the coast. In contrast to a coast, normal transport across a shallow landfast ice edge is possible. Since the surface stress curl across the ice edge is a delta function (discussed in section 1.4) it is difficult to deal with analytically but its effects can be understood by comparing the numerical and analytic results and by analyzing the governing equations at the ice edge.

### ***1.3 Numerical results***

We next compare the analytical solutions to numerical model results obtained using the Regional Ocean Modeling System (ROMS) primitive equation model. ROMS is a free surface model that couples the fast (barotropic) and slow (baroclinic) modes to solve the equations of motion (Shchepetkin and McWilliams, 2005). For direct comparison to the analytical results, ROMS was configured to solve the linearized

vertically averaged shallow water equations. Both the surface and bottom stresses are linearly related to the velocity, i.e.  $B, S \propto ru$  and the bottom slope is the same as in the analytical model. Unlike the analytical model, the numerical solutions specify bottom stress separately from under-ice stress and the bottom friction coefficient is constant everywhere (with  $r_b = 10^{-4} \text{ m s}^{-1}$ ). So in the basic numerical experiment the combined frictional drag of the ice and the bottom is  $\sim 2$  times that of the basic ALW solution. For the basic numerical experiment, ice covers the area inshore of the 20 m isobath ( $\sim 26$  km offshore). Additional experiments examined the effects of varying ice width and spatial variations in the ice-ocean friction coefficient. The coast lies along the southern boundary and the remaining boundaries are open. The model domain is a rectangle 600 km in east-west extent and 200 km in north-south extent.

The ROMS experiments allow us to include the transition between landfast and ice-free waters, including the infinite surface stress curl at the landfast ice edge. Additionally, the effects of a wider range of along- and cross-shore landfast ice variability can be addressed with the numerical model. In the numerical experiments, inflow magnitude was ramped up gradually over 4 days and the results examined after  $\sim 10$  days, when steady state was attained. The basic result from the numerical experiments is shown in Figure 1.6A, for the same constants as the basic ALW solution (see Table 1.1). For comparison, Figure 1.6B shows the analytical solution to the ALW vorticity equation for the same parameter values (except with a slightly wider inflow to account for differences in how the sea level is initialized in the numerical model). There are clear differences between the solutions; offshore the curvature of the numerical contours is

much different than in the landfast ice analytic solution, indicating that differences in the offshore boundary condition indeed affect the solution. Also, the 0.01 contour extends farther along the coast in numerical results than it does in the analytical ALW solution. In the numerical experiment the sea level at the western boundary is 4 cm and the along-shore velocity is  $0.65 \text{ m s}^{-1}$  eastward at the western boundary. While these velocities are quite large, the along-shore velocity decays to  $\sim 15 \%$  of its inflow value over  $\sim 30 \text{ km}$ , similar to the scale from the analytical model. Figure 1.7 is a companion plot showing the transport streamlines (panel A), and the along- and cross-shore velocities (panels B and C respectively) from the numerical experiment shown in Figure 1.6A. The sensitivity of the numerical results to variations in the ice-ocean friction coefficients are discussed next and differences between the analytical and numerical solutions are discussed in section 1.4.

Figures 1.8-1.11 summarize the effect of the ice-ocean friction coefficient on the along-shore sea level slope. For comparison among various experiments the along-shore sea level slope in these figures is normalized by the sea level at  $x = y = 0$ , so the plots have units of  $\text{m}^{-1}$ . A normalized sea level slope of  $O(10^{-6} \text{ m}^{-1})$  corresponds to an actual sea level slope of  $O(10^{-7})$ . Overall, Figures 1.8-1.11 show that the greatest variation in the along-shore sea level slope is due to the magnitude of the friction coefficient and to the magnitude of the cross-shore gradient ( $C_3$ ) of the ice-ocean friction coefficient. Smaller variations are associated with along-shore variability ( $C_1$ ) of the ice-ocean friction coefficient.

Figure 1.8 was generated by changing the value of  $A$  in eq. 1.4, the ice-ocean friction coefficient:  $(r_{ice} + r_b) = A \times [C_0 + C_1 \sin(mx)](C_2 + C_3 y)^2$  with the values of the



other coefficients being those of the basic ALW analytical model (given in Table 1.1).

Such that the value of  $[C_0 + C_1 \sin(mx)](C_2 + C_3 y)^2$  is  $O(10^{-4} \text{ m s}^{-1})$  and  $A$  varies

between 1 and 10. Figure 1.8 indicates that an increase in  $A$  increases the along-shore sea level slope consistent with the ATW and ALW vorticity equations. Subsequent figures show that the along-shore sea level slope is controlled by both variations in the cross-shore ice-ocean frictional coupling ( $C_3$ , Figure 1.9) and the along-shore ice-ocean frictional coupling ( $C_1$ , Figure 1.10). As with the analytical ALW solution, as  $C_3$  increases the vorticity balance changes (the relative magnitudes of the diffusive-like and advective-like vorticity terms change with  $C_3$ ) and the along- and cross-shore spreading of the mound change in a manner similar to the ALW solution. For small  $C_3$  the diffusive-like term dominates and for large  $C_3$  the diffusive- and advective-like terms are of similar magnitudes. There are differences between the analytical and numerical solutions due primarily to the inclusion of the ice edge and which are discussed in detail below. Close examination of the results included in Figure 1.10 show that the sea level isopleths are bent towards the coast with increasing along-shore distance by the along-shore increase in the ice-ocean friction coefficient acting in concert with the infinite stress curl across the ice edge, which inhibits offshore transport. This is in contrast to the analytical ALW solution where the sea level isopleths are bent offshore (with increasing along-shore distance) by the ice edge boundary condition. The difference is discussed further in section 1.4. As with the analytical ALW solution, changes in  $m$  do not change the along-shore sea level slope. Instead, the solution is affected by  $C_1$ , the magnitude of

the along-shore change in the drag (the analytical ALW solution is only weakly sensitive to  $C_I$ ).

Despite the complications due to the spatially-varying friction, the dynamics of the flows beneath landfast ice are similar enough to the ATW that Csanady's (1978) non-dimensional analysis is helpful in diagnosing the dynamics of the idealized ALW model that includes variable surface friction. This is examined next.

#### ***1.4 Comparison of analytic and numerical results***

Before beginning, we note that there are slight differences between analytic and numerical results imposed by differences in depth at the coast and the inflow width. For numerical stability the depth at the coast for the basic numerical experiment is  $h_o = 1$  m, the same as in the analytic ice model. The ATW solution assumes a depth of zero at the coast. As a result, the along-shore stress terms responsible for cross-shore spreading of the inflow are slightly smaller in the numerical results than in the ATW solutions, i.e., diffusivity is smaller so the along-shore sea level slope is slightly reduced compared to the ATW solution.

Despite attempts to match the inflow width, the numerical inflow is slightly wider than in the ALW solution so that along-shore sea level slope is reduced. This is visible at the western boundary in Figure 1.6 and partially explains why the 0.005 contour extends farther along-shore in the numerical results than in the analytical ALW solution. In general, all solutions are extremely sensitive to the inflow width. This basic result is consistent with Csanady's ATW solution, which predicts that an inflow affects

circulation along a shelf to distances of  $l^2/\kappa$  where  $l$  is the inflow width and  $\kappa$  is the diffusivity ( $\kappa = r_b/fs$ , Csanady, 1978). Hence as inflow width increases, the along-shore sea level slope decreases. Thus in Figure 1.6, the 0.005 contour is initialized farther offshore in the numerical model than in the analytic model, so the contour moves farther along the coast.

The most substantial differences between the analytical ALW solution and numerical solutions result from differences in the offshore boundary conditions between the models. This is a result of the surface stress curl at the seaward ice edge, which is accounted for by the numerical model, but not the analytical ALW model. In order to understand the differences between the analytical and numerical results consider the governing equations;

$$\left. \begin{aligned} -fv &= -g \frac{\partial \eta}{\partial x} - \frac{(r_{ice} + r_b)u}{h} \\ fu &= -g \frac{\partial \eta}{\partial y} \\ \frac{\partial(uh)}{\partial x} + \frac{\partial(vh)}{\partial y} &= 0 \end{aligned} \right\} \quad 1.16$$

Taking the curl of the along-shore momentum equation across the ice edge underscores the effect of the surface stress curl at the ice edge on transport across the ice edge:

$$-f \frac{\partial}{\partial y}(vh) = -g \frac{\partial}{\partial y} \left( h \frac{\partial \eta}{\partial x} \right) - u \frac{\partial [r_i H(L-y)]}{\partial y} - (r_{ice} + r_b) \frac{\partial u}{\partial y} \quad 1.17$$

where the ice-ocean friction coefficient is  $r_{ice} = r_i H(L-y)$  and  $H$  is the Heaviside step function (Abramowitz and Stegun, 1972). Hence the ice-ocean drag induces a surface

stress inshore of  $y < L$ , but there is no surface stress offshore of  $y > L$ . The derivative of the step function is the delta function,

$$-\left. \frac{\partial [r_i H(L-y)]}{\partial y} \right|_{y=L} = +[r_{ice}]_{y=L} \delta \quad 1.18$$

where we use the convention that  $H(0) = 1/2$ . To demonstrate the effect of the surface stress curl on the transport across the ice edge we retain the cross-shore transport,  $vh$ , and momentarily neglect the remaining terms for clarity (these are included below for completeness):

$$\frac{\partial}{\partial y}(vh) = -u \frac{[r_{ice}]_{y=L}}{f} \delta \quad 1.19$$

The surface stress curl across the ice edge results in a reduction and convergence in the cross-shore transport at the ice edge for  $u > 0$ . Moreover, the cross-shelf convergence leads to along-shore transport divergence:

$$\frac{\partial}{\partial x}(uh) = u \frac{[r_{ice}]_{y=L}}{f} \delta \quad 1.20$$

Thus the surface stress curl at the ice edge redirects the flow downstream (i.e., toward  $x > 0$ ). In contrast, the ice-edge boundary condition in the analytical model forces the along-shore transport to zero at the ice edge so that all transport is cross-shore. As a consequence of the differences in the offshore boundary condition, the analytic solution exaggerates the effects of cross-shore changes in the ice compared to the numerical results.

The importance of the proximity to the ice edge is shown by plotting along-shore sea level slope [for  $0 \leq x \leq 100$  km and normalized by  $\eta$  ( $x = y = 0$ )] versus ice width (Figure 1.11). Plus signs denote experiments where the ice-ocean friction coefficient was everywhere constant whereas points denoted by x are from experiments using eq. 1.4, with  $A = 1$ . For the latter experiment the advective-like vorticity term (term 2 of the ALW vorticity equation) increases with increasing ice width and the along-shore sea level slope approaches a constant for landfast ice widths  $> \sim 30$  km. The figure shows that at along-shore distances less than 100 km the ice edge affects the vorticity balance beneath narrow ice covers ( $< 30$  km wide for the variable ice-ocean friction coefficient and  $< 40$  km for a constant ice-ocean friction coefficient). As ice width increases the magnitude of the along-shore sea level slope increases (the stress curl at the ice edge is a vorticity stretching term). In contrast, the analytical ALW model results show a decrease in the along-shore sea level slope with increasing ice width. Again these differences are a consequence of the different ice-edge boundary condition between the two models. Whereas the analytic sensitivity to ice width is a result of the transport boundary condition at the ice edge, the result in Figure 1.11 arises due to the surface stress curl across the ice edge. The boundary condition in the analytical ALW solution leads to excessive transport across the ice edge, whereas the surface stress curl included in numerical results restricts transport across the ice edge.

The ATW (and ALW) analytical models show that bottom friction (and in our ALW model, under-ice friction) causes a lateral inflow to spread across the shelf with increasing along-shore distance. The ATW predicts that the cross-shore width of flow

controlled by bottom friction is  $L_y = (2r_b x / fs)^{1/2}$  (Csanady, 1978). A factor of 2 is included to account for the inclusion of surface and bottom friction. For the parameters given above and an along-shore distance of  $x = 100$  km, the width of the inflow is 20 km. While the basic behavior of the numerical and analytical solutions are consistent with this expression, our results show that the ice edge and the gradient in the ice-ocean friction coefficient affect the cross-shore length scale as well. Numerical results show that the flow broadens less with along-shore distance than the analytical ALW and ATW solutions because the ice edge stress curl is a vortex stretching term.

The analysis of transport across the ice edge heuristically shows that the surface stress curl across the ice edge redirects cross-shore transport in the positive along-shore direction. A slightly different approach shows that the mechanism by which the flow “feels” the ice edge can be understood in terms of an advective-like vorticity term at the ice edge. Taking the curl of the governing equations across the ice edge leads to a slightly different vorticity equation than for the shelf beneath landfast ice:

$$\left[ \frac{\partial \eta}{\partial x} = \frac{r_{ice} + r_b}{fs} \frac{\partial^2 \eta}{\partial y^2} - r_i \delta \frac{\partial \eta}{\partial y} \right]_{y=L} \quad 1.21$$

Whereas beneath landfast ice the surface stress curl due to cross-shore changes in the ice-ocean drag enters in via the second advective-like vorticity term:

$$\frac{\partial \eta}{\partial x} = \underbrace{\frac{(r_{ice} + r_b)}{fs} \frac{\partial^2 \eta}{\partial y^2}}_{\text{term 1}} + \underbrace{\frac{1}{fs} \frac{\partial(r_{ice} + r_b)}{\partial y} \frac{\partial \eta}{\partial y}}_{\text{term 2}} \quad 1.22$$

Hence the under-ice vorticity balance requires that an increase in the gradient of the ice-ocean friction coefficient leads to an increase in the magnitude of the along-shore sea

level slope. In contrast, equation 1.21 requires that an increase in the magnitude of the vorticity term due to the ice edge stress curl be balanced by a decrease in along-shore sea level slope magnitude. While the magnitude of the advective-like vorticity due to the ice edge stress curl does not change, the magnitude of the cross-shore sea level slope at the ice edge decreases with increasing ice width. As seen in Figure 1.11 the ice edge stress curl vorticity term decreases in importance as ice width increases. By including the surface stress curl (and excluding the excessive cross-shore transport caused by the analytic model boundary condition) the along-shore sea level slopes in the numerical results are generally smaller than those predicted by the analytical ALW solution. Alternatively, the vorticity balance changes abruptly on crossing the ice edge due to the ice edge stress curl. Hence the diffusive-like vorticity term decreases across the ice edge so the along-shore sea level slope must decrease.

To illustrate the effects of the important vorticity terms (rather than differences in model configuration or differences between analytical and numerical experiments) we show the result of three numerical experiments in Figure 1.12. In all experiments the depth at the coast is 1 m and the inflow width is the same. In panel a, ice covers the area inshore of the 20 m isobath and the ice-ocean friction coefficient is the same as for the basic analytical ALW solution ( $r_{ice} = [C_0 + C_1 \sin(mx)](C_2 + C_3 y)^2$  the value of the constants is given in Table 1.1) and the bottom friction coefficient is constant ( $r_b = 10^{-4} \text{ m s}^{-1}$ ) everywhere. Panel b is a numerical run equivalent to the ATW solution with  $r = 2 \times 10^{-4} \text{ m s}^{-1}$  everywhere and no ice edge. In the third experiment (panel c), there is ice inshore of the 20 m isobath and the ice-ocean friction coefficient is constant everywhere

there is ice ( $r_{ice} = 10^{-4} \text{ m s}^{-1}$ ). The bottom friction coefficient is constant everywhere and is  $10^{-4} \text{ m s}^{-1}$ . Comparing panels a and c (both include an ice edge) to panel b (no ice edge) shows that the ice edge stress curl is a vorticity stretching term and is important for ice covers as wide as 26 km. Differences between panels a and c are due to the advective-like vorticity term. Panel a includes this term which arises due to cross-shore variations in the under-ice friction coefficient. For constant under-ice friction this term is absent (panel c).

As mentioned above, the cross-shore stress terms ( $B_y$  and  $S_y$ , included in the numerical results but neglected in the analytic results) do not contribute to substantial differences between analytical and numerical results. Numerical results show that close to the western boundary, the inflow undergoes rapid adjustment and at distances less than 5 km from the western boundary cross-shore stress terms are on the same order of magnitude as the along-shore stress terms. At distances greater than 5 km from the western boundary, the cross-shore stress terms are at least an order of magnitude smaller than the along-shore stress terms. Also, since the wave number of the under-ice friction,  $m$ , is unimportant this also demonstrates that the derivative of the cross-shore stresses is unimportant.

### ***1.5 Summary and conclusions***

Building upon Csanady's arrested topographic wave model (the ATW, Csanady, 1978), we constructed a vorticity equation (termed the ALW vorticity equation) that includes vorticity contraction terms due to the presence of a landfast ice cover (a surface stress) and bottom friction. Allowing for spatial variations in under-ice friction leads to



an additional vorticity contraction term not present in the ATW model. The model is forced by a lateral inflow along its western boundary. Comparison between analytical solutions to the ALW vorticity equation and numerical simulations shows that the analytic boundary condition is problematic and that the surface stress curl across the ice edge (included in numerical experiments) is a vortex stretching term similar to rotation and bottom slope that causes the inflow to hug the coast. Numerical results show that ice width, the magnitude of the ice-ocean friction coefficient and cross-shore gradients in the ice-ocean friction coefficient are of first-order importance to the behavior of the solution, and though of secondary importance, along-shore changes in the ice-ocean friction coefficient affect the solution as well.

All models (numerical, the ALW and the ATW) show that due to the presence of bottom friction and the additional frictional coupling between the landfast ice and the ocean a velocity signal due to an elevated sea level will not be coherent at large distances from the source although sea level may be. Thus Weingartner et al.'s (2009) observations of currents beneath the landfast ice cover (near Prudhoe Bay, ~ 300 km east of Barrow Canyon) will probably show no relation between currents in the vicinity of Barrow. However, currents within about 50 km of Barrow may be coherent with the flow in Barrow Canyon.

Our results suggest that proper interpretation of current observations beneath landfast ice requires knowing the ice width, the magnitude of the ice-ocean friction coefficient, and spatial variations in this coefficient, since these affect the vorticity balance of shallow landfast ice-covered shelves. A subsequent paper uses the ALW

vorticity equation to model the effect of a wind offshore of the seaward landfast ice edge and how the presence of the ice changes the response from the ice-free case.

While useful for heuristic purposes these idealized models clearly oversimplify the potential complexity of the landfast ice zone of Arctic shelves. Our analyses have neglected other possible influences of the under-ice topography, including blocking and channeling flows, and form drag (e.g. McPhee, 1990). In addition, ice thickness (due to ridging) may increase on approaching the landfast ice edge, implying that cross-shore variations in water depth may not change solely through the sloping bottom. We note further that results from Morris et al. (1999), indicate that the change between the immobile landfast ice and highly mobile drifting pack ice may not be as abrupt as modeled here. Instead there may be a transition zone consisting of a region of reduced ice mobility between the landfast and freely drifting pack ice. Hence the change in stress curl at the ice edge may not always be abrupt, as modeled here, but rather vary more gradually over this transition zone. These are all important considerations that require additional theoretical and observational efforts in order to understand the broad inner shelf regions of the Arctic Ocean.

## ***1.6 Appendix***

To elucidate the approximation that the stresses of the ice and of the bottom on the ocean are related to under-ice transport through a linear friction coefficient,  $r$ , such that the stress,  $\tau_x = -(r_{ice} + r_b)u/h$ , it is necessary to consider the origin of the bottom and under-ice stress terms [where  $h$  is the bottom depth,  $u$  is the along-shore velocity and the  $r$ 's are the linear ice and bottom (subscript  $b$ ) friction coefficients]. The stress of the ice

on the ocean is due to the frictional coupling between the ice and the ocean and observations show that the strength of the coupling depends on the under-ice topography, ice roughness, ambient stratification and the local flow rate (e.g. McPhee, 1990) and that the drag of the sea ice on the ocean is a combination of form (pressure) drag and skin friction.

Vertically integrating the momentum equations allows us to ignore the complexities of the frictional coupling between the ice and the ocean and instead parameterize the coupling using the definition of a stress and a quadratic drag law. For simplicity we only consider the along-shore,  $x$ , direction and we begin by introducing the definition of a stress (e.g. Kowalik and Murty, 1993),

$$\tau_x = \rho_0 N_z \frac{\partial u}{\partial z} \quad \text{A.1}$$

where  $\rho_0$  is the ambient fluid density,  $N_z$  is the vertical diffusion coefficient and  $z$  is the vertical direction. Following Kowalik and Murty (1993), we integrate the vertical momentum diffusion term from the bottom ( $-h$ ) to the free surface ( $\eta$ ):

$$\rho_0 \int_{-h}^{\eta} \frac{\partial}{\partial z} \left( N_z \frac{\partial u}{\partial z} \right) dz = \tau_x^s - \tau_x^b \quad \text{A.2}$$

Finally, the stress from the bottom and the ice is distributed over the water column so that the steady state, vertically averaged along-shore momentum equation is

$$-fv = -g \frac{\partial \eta}{\partial x} + \frac{\tau_x^s - \tau_x^b}{\rho_0 D} \quad \text{A.3}$$

where  $D = h + \eta$  is the total depth. The under-ice and bottom stresses can be expressed using quadratic drag laws (Kowalik and Murty, 1993) such that

$$\tau_x^s = -\rho r_{surf} u \sqrt{u^2 + v^2} \quad \text{and} \quad \tau_x^b = \rho r_{bot} u \sqrt{u^2 + v^2} \quad \text{A.4}$$

The terms  $r_{surf}$ ,  $r_{bot}$  are the ice-ocean and bottom drag coefficients, respectively. The ice-ocean drag coefficient depends upon the local flow rate, ice topography and the roughness of the ice (e.g. Shirasawa, 1986; McPhee, 1990; Kowalik and Murty, 1993).

McPhee (1990) reports values for the ice-ocean drag coefficient between  $0.4 - 3 \times 10^{-2}$ . McPhee (1990) reports the roughness length,  $z_0$  which we then convert to a drag

coefficient using the following formula from Shirasawa (1986):  $r_{surf} = \kappa^2 \left( \ln\left(\frac{1}{z_0}\right) \right)^{-2}$

where  $\kappa$ , von Karman's constant, = 0.4. The minimum value ( $4 \times 10^{-3}$ ) is based on ice measured as smooth by Langleben (1980) as reported in McPhee (1990). For neutrally stratified flow, Shirasawa (1986) reports a range between  $5 - 9 \times 10^{-3}$ . Since Shirasawa's measurements were done in neutrally stratified conditions, the controlling factor in his estimates of the drag coefficients was ice topography: the rougher the ice the greater the drag coefficient.

In our treatment we further simplify the problem by assuming  $D \approx h$  and

$r_s \sqrt{u^2 + v^2} = r_{ice}$ , where  $r_{ice}$  has units of  $\text{m s}^{-1}$  and is strongly dependent on velocity. Note since  $r_{ice}$  is not non-dimensional, the magnitude will vary with the chosen units (similar to Manning coefficients in hydraulics). With these simplifications, we have

$$-f\nu = -g \frac{\partial \eta}{\partial x} - \frac{(r_{ice} + r_b)u}{h} \quad \text{A.5}$$

If we assume that near the coast the ice is smooth (and ignore stratification) then for a current velocity of  $10^{-1}$  ( $10^{-2}$ )  $\text{m s}^{-1}$  based on the range in drag coefficients McPhee

(1990) reports,  $r_{ice} = 4 \times 10^{-4}$  ( $4 \times 10^{-5}$ )  $\text{m s}^{-1}$ , whereas farther offshore where the ice is rough, we expect  $r_{ice} \sim 10^{-3}$  ( $10^{-4}$ ). Shirasawa (1986) found a slightly smaller range in the roughness length though his values are from a single area (landfast ice in the Canadian Archipelago) whereas McPhee's (1990) values are compiled from a range of sea ice types around the Arctic basin. From Shirasawa's (1986) values the range in  $r_{ice}$  for  $u = 0.10 \text{ m s}^{-1}$  is between  $5 - 9 \times 10^{-4}$  whereas for  $u = 10^{-2} \text{ m s}^{-1}$   $r_{ice}$  will range between  $5 - 9 \times 10^{-5}$ . Thus the strength of frictional coupling is strongly dependent on the current velocity.

In Chapter 2 where we consider flow driven by ice edge upwelling, in the simplest case the current velocity is large near the ice edge ( $O[10^{-1} \text{ m s}^{-1}]$ ) and small near the coast ( $\leq 10^{-2} \text{ m s}^{-1}$ ) thus we might realistically expect  $r_{ice}$  to range between  $10^{-3} \text{ m s}^{-1}$  at the ice edge and between  $10^{-5}$  to  $10^{-4} \text{ m s}^{-1}$  at the coast (a slightly larger range than the largest we consider in Chapter 2). In Chapter 1 where in general the current speed is largest near the coast and smaller near the ice edge, a maximum realistic range for  $r_{ice}$  might be between  $10^{-4}$  at the coast and  $3 \times 10^{-4} \text{ m s}^{-1}$  at the ice edge, and this is a slightly wider range than considered in the basic solution (where  $r_{ice}$  ranged between  $10^{-4}$  and  $\sim 1.4 \times 10^{-4} \text{ m s}^{-1}$ ). Given the strong dependence of the linear friction coefficient  $r_{ice}$  on velocity, in a more realistic treatment than the models we consider, we might expect the cross-shore gradient in the ice friction coefficient to vary with the current velocity and thus the importance of the advective vorticity term would vary as well.

### 1.6.1 Governing equations

We begin with the steady vertically averaged momentum equations under the long wave approximation (Csanady, 1978).

$$\left. \begin{aligned} -fv &= -g \frac{\partial \eta}{\partial x} + \frac{-B_x - S_x + F_x}{h} \\ fu &= -g \frac{\partial \eta}{\partial y} + \frac{-B_y - S_y + F_y}{h} \\ \frac{\partial(uh)}{\partial x} + \frac{\partial(vh)}{\partial y} &= 0 \end{aligned} \right\} \text{A.6}$$

where  $v$  is the cross-shore velocity,  $u$  is the along-shore velocity,  $g$  is the acceleration due to gravity,  $\eta$  is the sea level anomaly,  $h$  is the depth ( $h = h_0 + sy$ ,  $s$  is the constant slope and  $h_0$  is the depth at the coast) and  $B$  and  $S$  are the surface and bottom stresses due to bottom and under-ice friction, respectively, and  $F$  is the wind stress. Note  $B$  and  $S$  both have the same sign.

Assuming that  $B$  and  $S$  are proportional to the under-ice transport, we have

$$\left. \begin{aligned} -fv &= -g \frac{\partial \eta}{\partial x} + \frac{-(r_{ice} + r_b)u + F_x}{h} \\ fu &= -g \frac{\partial \eta}{\partial y} + \frac{-(r_{ice} + r_b)v + F_y}{h} \\ \frac{\partial(uh)}{\partial x} + \frac{\partial(vh)}{\partial y} &= 0 \end{aligned} \right\} \text{A.7}$$

where  $r_{ice}$  [ =  $r_{ice}(x,y)$  ] is the linear ice-ocean friction coefficient and  $r_b$  is the linear bottom friction coefficient. Taking the curl of the governing equations, we find

$$g \frac{\partial \eta}{\partial x} = \underbrace{\frac{((r_b v)_x - (r_b u)_y)}{S}}_{\substack{\text{Bottom Stress Curl} \\ \text{Bottom Slope}}} + \underbrace{\frac{((r_{ice} v)_x - (r_{ice} u)_y)}{S}}_{\substack{\text{Surface Stress Curl} \\ \text{Bottom Slope}}} - \underbrace{\frac{((F_y)_x - (F_x)_y)}{S}}_{\substack{\text{Wind Stress Curl} \\ \text{Bottom Slope}}} \quad \text{A.8}$$

Long Shore Pressure Gradient

So the along-shore pressure gradient is balanced by the stress curls divided by the bottom slope. From the cross-shore momentum equation, the second of equations A.7, we see that the cross-shore balance is between Coriolis, surface and bottom stresses and the wind stress:

$$g \frac{\partial \eta}{\partial y} = -fu - \frac{(r_{ice} + r_b)v}{h} + \frac{F_y}{h} \quad \text{A.9}$$

For the area under the landfast ice cover the wind stress is zero and we have

$$\left. \begin{aligned} -fv &= -g \frac{\partial \eta}{\partial x} + \frac{-(r_{ice} + r_b)u}{h} \\ fu &= -g \frac{\partial \eta}{\partial y} + \frac{-(r_{ice} + r_b)v}{h} \\ \frac{\partial(uh)}{\partial x} + \frac{\partial(vh)}{\partial y} &= 0 \end{aligned} \right\} \quad \text{A.10}$$

Neglecting the cross-shore stress terms as small compared to the along-shore stress terms (Csanady, 1978)

$$\left. \begin{aligned} -fv &= -g \frac{\partial \eta}{\partial x} + \frac{-(r_{ice} + r_b)u}{h} \\ fu &= -g \frac{\partial \eta}{\partial y} \\ \frac{\partial(uh)}{\partial x} + \frac{\partial(vh)}{\partial y} &= 0 \end{aligned} \right\} \quad \text{A.11}$$

We can construct a vorticity equation, in terms of  $\eta$ , for the area under the landfast ice cover by taking the curl of the governing equations, eqns. A.11,

$$\frac{\partial \eta}{\partial x} = \frac{(r_{ice} + r_b)}{fs} \frac{\partial^2 \eta}{\partial y^2} + \frac{1}{fs} \frac{\partial (r_{ice} + r_b)}{\partial y} \frac{\partial \eta}{\partial y} \quad \text{A.12}$$

Equation A.12 is a parabolic differential equation, a diffusion equation with variable diffusivity. Its solution depends on the boundary conditions at the coast ( $y = 0$ ) and at the ice edge ( $y = L$ ) and an “initial condition” at  $x = 0$ .

Equation A.12 is separable for  $(r_{ice} + r_b) = [C_0 + C_1 \sin(mx)](C_2 + C_3 y)^2$  and  $\eta = X(x)Y(y)$ . Substituting these expressions into (A.12) and simplifying yields:

$$\frac{1}{X[C_0 + C_1 \sin(mx)]} \frac{dX}{dx} = \frac{(C_2 + C_3 y)^2}{fsY} \frac{d^2 Y}{dy^2} + \frac{1}{fsY} \frac{d(C_2 + C_3 y)^2}{dy} \frac{dY}{dy} \quad \text{A.13}$$

from which we obtain:

$$\begin{aligned} \frac{fs}{X[C_0 + C_1 \sin(mx)]} \frac{dX}{dx} &= \lambda C_3^2 \\ \frac{(C_2 + C_3 y)^2}{Y} \frac{d^2 Y}{dy^2} + \frac{1}{Y} \frac{d(C_2 + C_3 y)^2}{dy} \frac{dY}{dy} &= \lambda C_3^2 \end{aligned} \quad \text{A.14}$$

where  $\lambda$  is the separation constant. The second of equations A.14 is of Sturm Liouville form so the solutions,  $Y$ , form a complete orthogonal basis set of the function space and the separation constants  $\lambda$  are eigenvalues.

The expression for  $X$  is obtained directly upon integration:

$$X = \exp \left\{ \frac{\lambda}{fs} \left[ C_0 x - \frac{C_1}{m} \cos(mx) \right] C_3^2 \right\} \quad \text{A.15}$$

The integration constant is left out because it can be included in the overall solution. To solve for  $Y$ , we assume that:



$$Y = (C_2 + C_3 y)^\alpha \Rightarrow \frac{dY}{dy} = \alpha C_3 (C_2 + C_3 y)^{\alpha-1} \text{ and } \frac{d^2 Y}{dy^2} = \alpha(\alpha-1) C_3^2 (C_2 + C_3 y)^{\alpha-2} \quad \text{A.16}$$

Substituting these expressions into the  $Y$ -equation (the second of equations A.16) yields the characteristic equation

$$\alpha(\alpha-1) C_3^2 (C_2 + C_3 y)^\alpha + 2\alpha C_3^2 (C_2 + C_3 y)^\alpha - \lambda C_3^2 (C_2 + C_3 y)^\alpha = 0$$

which simplifies to:

$$\alpha^2 + \alpha - \lambda = 0 \quad \text{A.17}$$

The roots of equation A.17 are

$$\alpha_{1,2} = -\frac{1}{2} \pm i \sqrt{-\frac{1}{4} - \lambda} \quad \text{A.18}$$

In order to determine the solution, two boundary conditions are necessary: one at the coast and one at the ice edge ( $y = L$ ). The coastal boundary condition is no transport through the coast ( $vh = 0$ ) at  $y = 0$ , which from the governing equations yields

$$\frac{\partial \eta}{\partial y} = \frac{fh_o}{(r_{ice} + r_b)} \frac{\partial \eta}{\partial x} \text{ at } y=0. \text{ At } y = L \text{ we specify that the sea level is continuous, i.e.,}$$

$$\frac{\partial \eta}{\partial y} = 0. \text{ There are three cases to consider:}$$

1. If  $\lambda = -\frac{1}{4}$  then  $\alpha = -\frac{1}{2}$  and the roots are real and repeated, in which case (e.g.

Boas, 1983)

$$Y(y) = A(C_2 + C_3 y)^{-1/2} + B(C_2 + C_3 y)^{-1/2} \ln(C_2 + C_3 y) \quad \text{A.19}$$

and application of the boundary condition leads to the trivial solution.

2. If  $\lambda > -\frac{1}{4}$ , then we have distinct real roots and

$Y = A(C_2 + C_3 y)^{\alpha_1} + B(C_2 + C_3 y)^{\alpha_2}$ , which also yields trivial solutions upon applying the boundary conditions.

3. If  $\lambda < -\frac{1}{4}$ , then  $\alpha_{1,2} = -\frac{1}{2} \pm i\sqrt{-\frac{1}{4} - \lambda}$ , the roots are complex conjugates with solution:

$$Y = A(C_2 + C_3 y)^{-1/2} \sin\left(\sqrt{-\frac{1}{4} - \lambda} \ln(C_2 + C_3 y) + \varphi\right) \quad \text{A.20}$$

where  $A$  and  $\varphi$  are constants determined by the boundary and initial conditions.

Applying the offshore boundary condition to  $Y$  (from A.20), we find

$$\begin{aligned} \frac{dY}{dy} = & -\frac{AC_3}{2}(C_2 + C_3 y)^{-3/2} \sin\left(\sqrt{-\frac{1}{4} - \lambda} \ln(C_2 + C_3 y) + \varphi\right) \\ & + AC_3(C_2 + C_3 y)^{-3/2} \sqrt{-\frac{1}{4} - \lambda} \cos\left(\sqrt{-\frac{1}{4} - \lambda} \ln(C_2 + C_3 y) + \varphi\right) \\ & - \frac{AC_3}{2}(C_2 + C_3 L)^{-3/2} \sin\left(\sqrt{-\frac{1}{4} - \lambda} \ln(C_2 + C_3 L) + \varphi\right) \\ & + AC_3(C_2 + C_3 L)^{-3/2} \sqrt{-\frac{1}{4} - \lambda} \cos\left(\sqrt{-\frac{1}{4} - \lambda} \ln(C_2 + C_3 L) + \varphi\right) = 0 \end{aligned}$$

Further simplification leads to a condition for  $\varphi$

$$\frac{1}{2} \sin\left(\sqrt{-\frac{1}{4} - \lambda} \ln(C_2 + C_3 L) + \varphi\right) = \sqrt{-\frac{1}{4} - \lambda} \cos\left(\sqrt{-\frac{1}{4} - \lambda} \ln(C_2 + C_3 L) + \varphi\right).$$

Finally

$$\varphi = \arctan\left(2\sqrt{-\frac{1}{4}-\lambda}\right) - \sqrt{-\frac{1}{4}-\lambda} \ln(C_2 + C_3 L) - n\pi \quad \text{A.21}$$

where  $n=0,1,2,3\dots$  Our solution has the following form;

$$\eta = A \exp\left\{\frac{\lambda}{fs}\left[C_0 x - \frac{C_1}{m} \cos(mx)\right] C_3^2\right\} \frac{\sin\left(\sqrt{-\frac{1}{4}-\lambda} \ln(C_2 + C_3 y) + \varphi\right)}{(C_2 + C_3 y)^{1/2}} \quad \text{A.22}$$

To determine the eigenvalues,  $\lambda$ , we apply the remaining boundary condition at

the coast ( $y = 0$ );  $\frac{\partial \eta}{\partial y} = \frac{fh_o}{(r_{ice} + r_b)} \frac{\partial \eta}{\partial x}$ . Calculating the terms

$$\frac{fh_o}{(r_{ice} + r_b)} \frac{\partial \eta}{\partial x} = Ah_o \frac{\lambda}{s} C_3^2 \exp\left\{\frac{\lambda}{fs}\left[C_0 x - \frac{C_1}{m} \cos(mx)\right] C_3^2\right\} \frac{\sin\left(\sqrt{-\frac{1}{4}-\lambda} \ln(C_2 + C_3 y) + \varphi\right)}{(C_2 + C_3 y)^{-5/2}}$$

$$\frac{\partial \eta}{\partial y} = A \exp\left\{\frac{\lambda}{fs}\left[C_0 x - \frac{C_1}{m} \cos(mx)\right] C_3^2\right\} *$$

$$\left[ \begin{aligned} &-\frac{C_3}{2} (C_2 + C_3 y)^{-3/2} \sin\left(\sqrt{-\frac{1}{4}-\lambda} \ln(C_2 + C_3 y) + \varphi\right) \\ &+ C_3 (C_2 + C_3 y)^{-3/2} \sqrt{-\frac{1}{4}-\lambda} \cos\left(\sqrt{-\frac{1}{4}-\lambda} \ln(C_2 + C_3 y) + \varphi\right) \end{aligned} \right]$$

This leads to an equation for the eigenvalues

$$\sqrt{-\frac{1}{4}-\lambda} [\ln(C_2) - \ln(C_2 + C_3 L)] + (l - n)\pi =$$

$$\arctan\left(\frac{2\sqrt{-\frac{1}{4}-\lambda}}{\left(h_o \frac{\lambda}{s} 2 \frac{C_3}{C_2} + 1\right)}\right) - \arctan\left(2\sqrt{-\frac{1}{4}-\lambda}\right) \quad \text{A.23}$$

where  $l, n \in \mathbb{Z}^+$ . Equation A.23 (appearing in the text as equation 1.10) can be solved for  $\lambda$  using Matlab (Table 1.2 in the text lists several of the eigenvalues). Once the eigenvalues and eigenfunctions are known, we can check the effect of changing the phase shift,  $\varphi$ , on the eigenfunctions. The first eigenvalue is simply the trivial solution. For  $n=0,1,2,3,\dots$ , the second eigenvalue,  $\lambda_1 \approx -37.5$  produces only one unique eigenfunction, For even  $n$ , all of the eigenfunctions are the same and for odd  $n$  the eigenfunctions are simply the eigenfunctions for even  $n$  multiplied by -1. This holds for the other eigenvalues also. Hence each eigenvalue produces one unique eigenfunction independent of the phase angle,  $\varphi$ .

### 1.6.2 Initial condition

The initial condition (at  $x = 0$ ) determines the constant  $A$  in the solution;

$$\eta = A_\lambda \exp \left\{ \frac{\lambda}{fs} \left[ C_0 x - \frac{C_1}{m} \cos(mx) \right] C_3^2 \right\} \frac{\sin \left( \sqrt{-\frac{1}{4} - \lambda} \ln(C_2 + C_3 y) + \varphi \right)}{(C_2 + C_3 y)^{1/2}} \quad \text{A.24}$$

$$A_\lambda = \frac{1}{\|Y_\lambda\|^2} \exp \left\{ \frac{\lambda}{fs} \frac{C_1 C_3^2}{m} \right\} \int_0^\infty \eta_0(y) \frac{\sin \left( \sqrt{-\frac{1}{4} - \lambda} \ln(C_2 + C_3 y) + \varphi \right)}{(C_2 + C_3 y)^{1/2}} dy \quad \text{A.25}$$

Where  $\eta_0(y)$  is the initial condition and summation is implied over  $A_\lambda$  in equation A.24.

Also,

$$\|Y_\lambda\|^2 = \int_0^L \frac{\sin^2 \left( \sqrt{-\frac{1}{4} - \lambda} \ln(C_2 + C_3 y) + \varphi \right)}{(C_2 + C_3 y)} dy \quad \text{A.26}$$

It is fairly straightforward to find  $Y_\lambda$ . Let  $u = \sqrt{-\frac{1}{4} - \lambda} \ln(C_2 + C_3 y) + \varphi$ , then

$$\|Y_\lambda\|^2 = \frac{1}{2C_3 \sqrt{-\frac{1}{4} - \lambda}} \left[ \sqrt{-\frac{1}{4} - \lambda} \ln(C_2 + C_3 y) + \varphi - \frac{1}{2} \sin \left( 2 \sqrt{-\frac{1}{4} - \lambda} \ln(C_2 + C_3 y) + 2\varphi \right) \right]_0^L \quad \text{A.27}$$

The remaining integral for  $A_\lambda$  can be evaluated analytically for certain simple choices of the initial condition (e.g. a delta function or a polynomial). For the exponential initial condition used in the text, the Matlab symbolic toolbox is used to perform the integration. Other initial conditions may require numerical evaluation of the integral.

### 1.6.3 Stream-functions

Using the continuity equation (the last of equations A.11), we define the stream-function

$$uh = \frac{\partial \psi}{\partial x}; \quad vh = -\frac{\partial \psi}{\partial y} \quad \text{A.28}$$

The complete stream-function is the sum of the contributions from  $uh$  and  $vh$  such that

$\psi = \psi_{uh} + \psi_{vh}$ . From A.24 and the second of equations A.11, we find

$$uh = -\frac{gh}{f} \sum_{\lambda} A_{\lambda} \exp \left\{ \frac{\lambda}{fs} \left[ C_0 x - \frac{C_1}{m} \cos(mx) \right] C_3^2 \right\} \left[ -\frac{1}{2} C_3 \frac{\sin \left( \sqrt{-\frac{1}{4} - \lambda} \ln(C_2 + C_3 y) + \varphi \right)}{(C_2 + C_3 y)^{3/2}} + C_3 \sqrt{-\frac{1}{4} - \lambda} \frac{\cos \left( \sqrt{-\frac{1}{4} - \lambda} \ln(C_2 + C_3 y) + \varphi \right)}{(C_2 + C_3 y)^{3/2}} \right]$$

and

$$\frac{\partial \psi}{\partial y} = -\frac{gh}{f} \sum_{\lambda} T_{\lambda} \exp \left\{ \frac{\lambda}{fs} \left[ C_0 x - \frac{C_1}{m} \cos(mx) \right] C_3^2 \right\} \times$$

$$\frac{C_3}{(C_2 + C_3 y)^{3/2}} \left[ \begin{aligned} & -\frac{1}{2} \sin \left( \sqrt{-\frac{1}{4} - \lambda} \ln(C_2 + C_3 y) + \varphi \right) + \\ & \sqrt{-\frac{1}{4} - \lambda} \cos \left( \sqrt{-\frac{1}{4} - \lambda} \ln(C_2 + C_3 y) + \varphi \right) \end{aligned} \right]$$

Further,  $\psi_{uh} = \int_0^L -\frac{gh}{f} \frac{\partial \eta}{\partial y} dy$ . To find the contribution from  $vh$ , note that  $\psi_{vh} = -\int_0^{\infty} v h dx$ .

From the governing equation, A.11,

$$vh = -\frac{gh}{f} \frac{\partial \eta}{\partial x} + (r_{ice} + r_b) \frac{g}{f} \frac{\partial \eta}{\partial y} \quad \text{A.29}$$

Then

$$\psi_{vh} = -\int_0^{\infty} v h dx = \frac{g}{f} \int_0^{\infty} -hY \frac{dX}{dx} + \frac{dY}{dy} (r_{ice} + r_b) X dx \quad \text{A.30}$$

which simplifies to

$$\psi_{vh} = -\frac{g}{f} \left( hY + \frac{(C_2 + C_3 y)^2}{\gamma} \frac{dY}{dy} \right) X_0^{\infty} \quad \text{A.31}$$

where  $\gamma = \frac{\lambda}{fs} C_3^2$ . Finally, the complete stream-function is

$$\psi = \int_0^L -\frac{gh}{f} \frac{\partial \eta}{\partial y} dy - \frac{g}{f} \left( hY + \frac{(C_2 + C_3 y)^2}{\gamma} \frac{dY}{dy} \right) X_0^{\infty} \quad \text{A.32}$$

## ***1.7 References***

- Abramowitz, M., Stegun, I.A., 1972. Handbook of Mathematical Functions with Formulas, Graphs, and Mathematical Tables. National Bureau of Standards, Washington, D.C.
- Boas, M.L., 1983. Mathematical Methods in the Physical Sciences, 2nd ed. Wiley, New York.
- Brink, K.H., Allen, J.S., 1998. Comments on "The non-wavelike response of a continental shelf to wind" by G. T. Csanady. *Journal of Marine Research* 56 (4), 789-792.
- Buchwald, V.T., Adams, J.K., 1968. The propagation of continental shelf waves. *Proceedings of the Royal Society of London. Series A. Mathematical and Physical Sciences* 305 (1481), 235-250.
- Clarke, A.J., 1978. On wind-driven quasi-geostrophic water movements at fast ice edges. *Deep Sea Research* 25 (1), 41-47.
- Csanady, G.T., 1978. The arrested topographic wave. *Journal of Physical Oceanography* 8 (1), 47-62.
- Fennel, W., Johannessen, O.M., 1998. Wind forced oceanic responses near ice edges revisited. *Journal of Marine Systems* 14 (1-2), 57-79.
- Gill, A.E., Schumann, E.H., 1974. The generation of long shelf waves by the wind. *Journal of Physical Oceanography* 4 (1), 83-90.

- Kowalik, Z., Murty, T.S., 1993. Numerical Modeling of Ocean Dynamics. World Scientific Publishing.
- Langleben, M.P., 1980. Water drag coefficient at AIDJEX, station Caribou, in: Pritchard, R.S. (Ed.), Sea Ice Processes and Models. University of Washington Press, pp. 464-471.
- Macdonald, R.W., Carmack, E.C., 1991. The role of large-scale under-ice topography in separating estuary and ocean on an Arctic shelf. *Atmosphere-Ocean* 29 (1), 37-53.
- Mahoney, A., Eicken, H., Shapiro, L., 2007. How fast is landfast sea ice? A study of the attachment and detachment of nearshore ice at Barrow, Alaska. *Cold Regions Science and Technology* 47 (3), 233-255.
- McPhee, M.G., 1990. Small scale processes, in: Smith, W.C. (Ed.), *Polar Oceanography Part A Physical Science*. Academic Press, New York, pp. 287-334.
- Morris, K., Li, S., Jefferies, M., 1999. Meso- and microscale sea-ice motion in the East Siberian Sea as determined from ERS-1 SAR data. *Journal of Glaciology* 45 (15), 370-383.
- Mountain, D.G., Coachman, L.K., Aagaard, K., 1976. On the flow through Barrow Canyon. *Journal of Physical Oceanography* 6 (4), 461-470.
- Okkonen, S.R., Ashjian, C.J., Campbell, R.G., Maslowski, W., Clement-Kinney, J.L., Potter, R., 2009. Intrusion of warm Bering/Chukchi waters onto the shelf in the western Beaufort Sea. *Journal of Geophysical Research* 114 (C1), C00A11.



- Pickart, R.S., Pratt, L.J., Torres, D.J., Whitley, T.E., Proshutinsky, A.Y., Aagaard, K., Agnew, T.A., Moore, G.W.K., Dail, H.J., 2010. Evolution and dynamics of the flow through Herald Canyon in the western Chukchi Sea. *Deep Sea Research Part II: Topical Studies in Oceanography* 57 (1-2), 5-26.
- Reimnitz, E., 2002. Interactions of river discharge with sea ice in proximity of Arctic deltas: a review. *Polarforschung* 70, 123-134.
- Rothrock, D.A., Thorndike, A.S., 1980. Geometric properties of the underside of sea ice. *Journal of Geophysical Research* 85 (C7), 3955-3963.
- Shchepetkin, A.F., McWilliams, J.C., 2005. The regional oceanic modeling system (ROMS): a split-explicit, free-surface, topography-following-coordinate oceanic model. *Ocean Modelling* 9 (4), 347-404.
- Shirasawa, K., 1986. Water stress and ocean current measurements under first-year sea ice in the Canadian Arctic. *Journal of Geophysical Research* 91 (C12), 14305-14316.
- Tucker, W.B., III, Weeks, W.F., Frank, M., 1979. Sea ice ridging over the Alaskan continental shelf. *Journal of Geophysical Research* 84 (C8), 4885-4897.
- Weingartner, T.J., Cavalieri, D.J., Aagaard, K., Sasaki, Y., 1998. Circulation, dense water formation, and outflow on the northeast Chukchi shelf. *Journal of Geophysical Research* 103 (C4), 7647-7661.

Weingartner, T.J., Danielson, S.L., Kasper, J.L., Okkonen, S.R., 2009. Circulation and water property variations in the nearshore Alaskan Beaufort Sea (1999-2007). US Dept. of Interior, Minerals Management Service, Alaska Outer Continental Shelf Region, Anchorage, Alaska, p. 154.

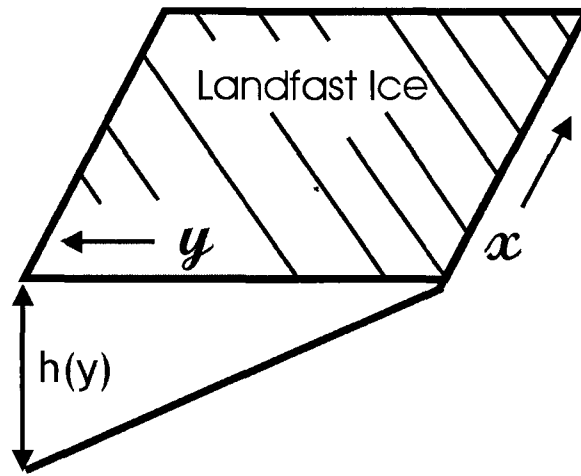
*1.8 Figures*

Figure 1.1. Coordinate system for the ALW, the landfast ice analytic model.

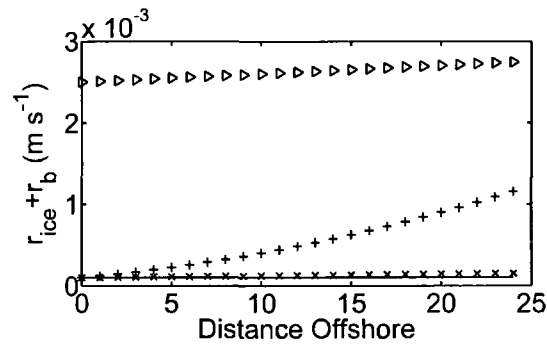


Figure 1.2. Magnitude of the ice-ocean friction coefficient. The ice-ocean friction coefficient at the western boundary ( $x = 0$ ) for various values of the constants given in Table 1.1. Xs mark the basic case ( $C_0 = 10^{-1}$ ,  $C_2=10^{-1}$ ,  $C_3=10^{-6}$ ). Plus signs mark  $C_0 = 10^{-1}$ ,  $C_2=10^{-1}$ ,  $C_3=10^{-5}$ . Triangles mark the case with  $C_0 = 10^{-1}$ ,  $C_2=5 \times 10^{-1}$ ,  $C_3=10^{-6}$ . The solid line is the constant ice-ocean friction coefficient ( $10^{-4}$ ). The full range between  $10^{-4}$  and  $10^{-3}$  was investigated using numerical simulations.

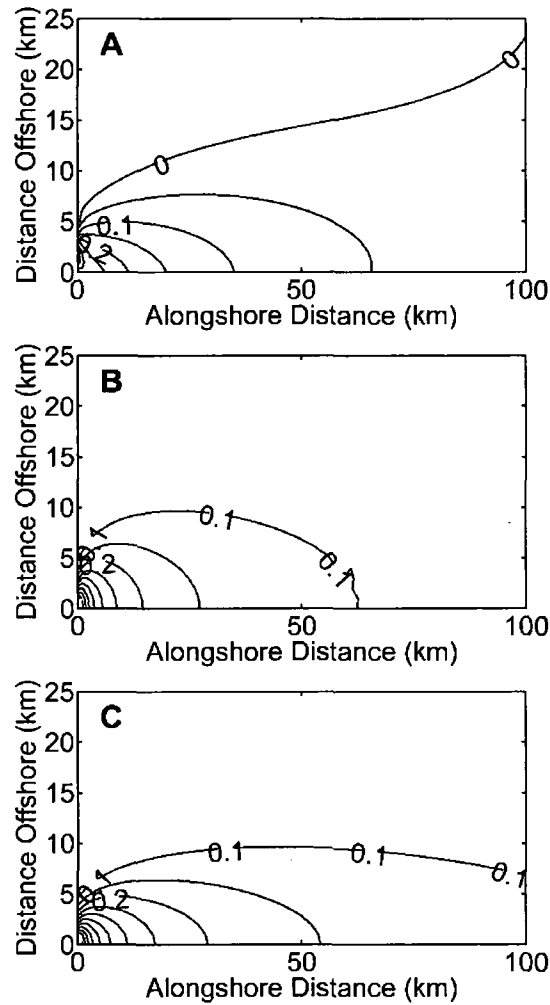


Figure 1.3. Contours of sea level anomaly,  $\eta$  (m). (A) the basic analytical ALW solution, with  $r_{ice} + r_b \sim O(10^{-4} \text{ m s}^{-1})$  with constants given in Table 1.1. (B) the ATW vorticity equation with  $r_b = 2 \times 10^{-4} \text{ m s}^{-1}$ . (C) the ATW solution with  $r_b = 10^{-4} \text{ m s}^{-1}$ . Other parameters are  $s = 7.5 \times 10^{-4}$  and  $f = 1.371 \times 10^{-4} \text{ s}^{-1}$ . The contour interval is 0.05. In all panels the forcing consists of an inflow at the western boundary due to elevated sea surface height at the coast,  $\eta(0, y) = e^{-y/2000}$ . Note distortion of the 0.1 contour near  $\sim 60$  km in B is due to difficulties in accurately reproducing the error function of the ATW solution far from the western boundary.

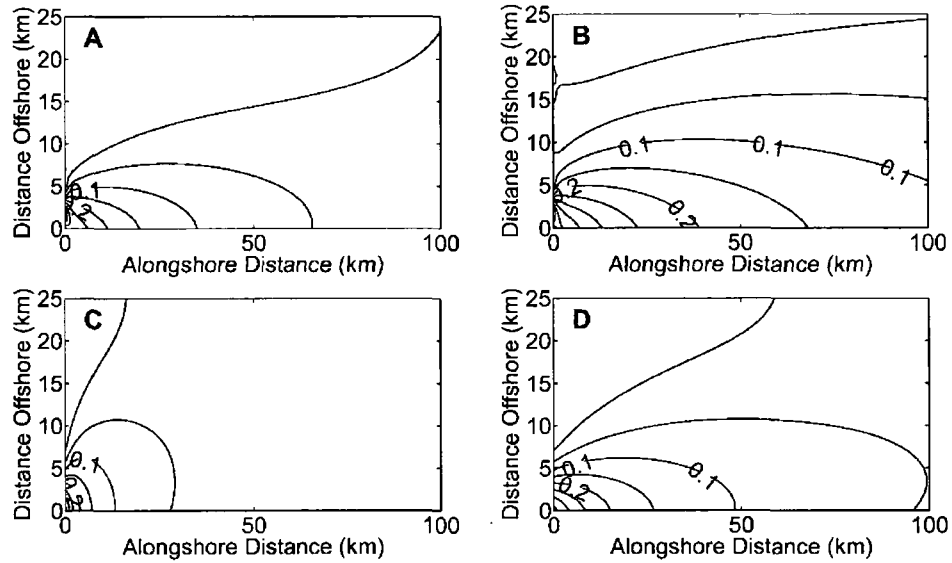


Figure 1.4. The effect of the ice-ocean friction coefficient on  $\eta$ . Contours of  $\eta$  showing the effect of various ice-ocean drag parameters on the behavior of the analytical ALW solution. Contour interval is 0.05 m. (A) the basic analytical ALW solution. (B) Analytical ALW solution for an ice width of 60 km. All other constants remain as for the basic analytical ALW solution. (C) Analytical ALW solution with  $C_2$  ( $C_2 = 0.2$  versus  $C_2 = 0.1$  for the other results in this figure). (D) Analytic ALW solution with  $C_3$  ( $C_3 = 5 \times 10^{-7}$  versus  $C_3 = 10^{-6}$  for other results in this figure).

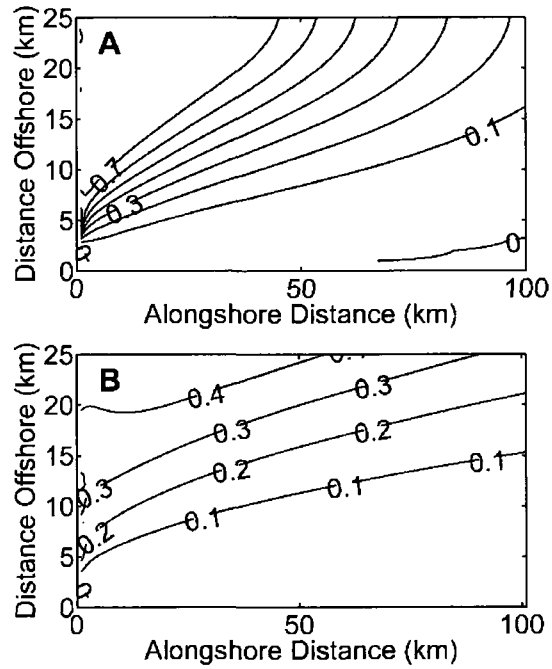


Figure 1.5. Transport streamlines for the analytical ALW solution. Transport is normalized by total transport. (A) Streamlines from the basic analytical ALW solution (for which  $\eta$  contours are shown in the top panel of Figure 1.4). (B) Transport streamlines for a wide ice cover ( $L = 60$  km, for which  $\eta$  contours are shown Figure 1.4b).

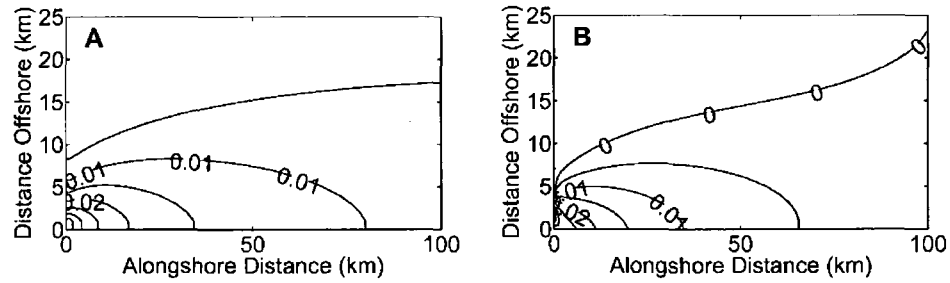


Figure 1.6. Contours of sea level anomaly,  $\eta$  (m). (A) From the basic ROMS experiment and (B) the basic analytical ALW solution. In A, the numerical experiment, the bottom friction coefficient is constant everywhere ( $r_b = 10^{-4} \text{ m s}^{-1}$ ). Inshore of the 20 m isobath  $r_{ice}$  is the same as the combined bottom and under-ice friction coefficients in the basic analytical ALW solution shown in B. To account for differences between the numerical and analytical initial conditions, in panel a, the inflow at the western boundary is slightly narrower;  $\eta(0, y) = 0.1x e^{-y/1500}$  than in the analytical ALW solution shown in panel b where  $\eta(0, y) = 0.1x e^{-y/2000}$ . In both cases  $s = 7.5 \times 10^{-4}$  and  $f = 1.371 \times 10^{-4} \text{ s}^{-1}$ .



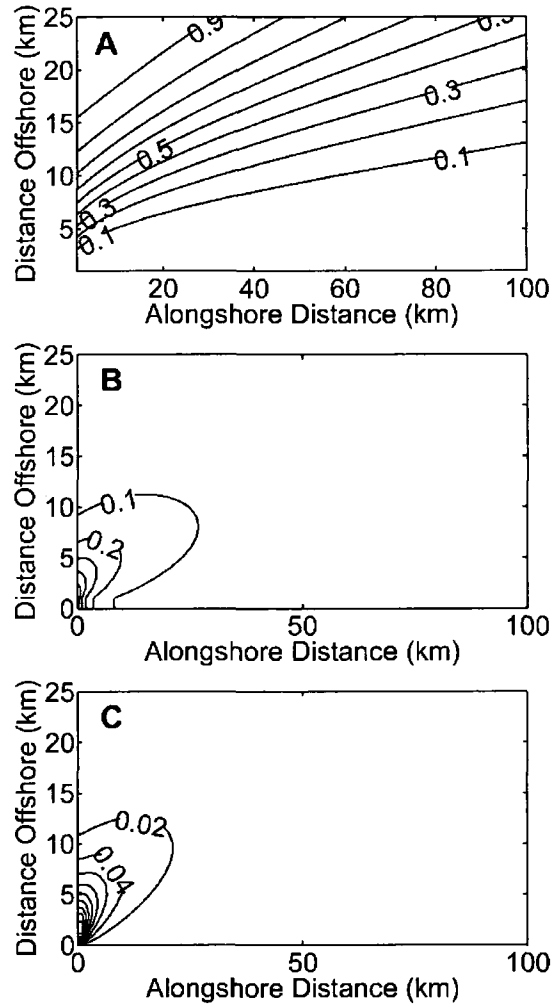


Figure 1.7. Along- and cross-shore transport. (A) Transport Streamlines (normalized by the total transport; top), (B) along-shore and (C) cross-shore velocities ( $\text{m s}^{-1}$ ) for the basic numerical experiment (for which  $\eta$  contours are shown in Figure 1.6a). Positive velocities denote eastward flow (B) and northwards (C).

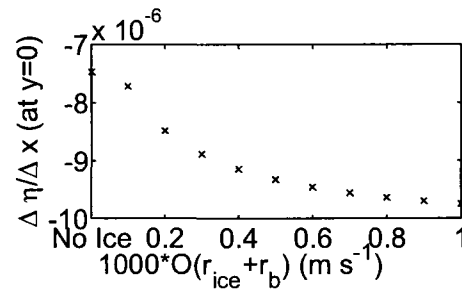


Figure 1.8. Normalized along-shore sea level slope ( $m^{-1}$ ) versus the magnitude of the ice-ocean friction coefficient ( $m s^{-1}$ ). The along-shore sea level slope is calculated by taking the difference in sea surface height between the western boundary and 100 km along-shore and dividing by the along-shore distance (100 km). For comparison between experiments, the sea level slope is normalized by the sea level at  $x = y = 0$  and the units are  $m^{-1}$ . No ice indicates the case where  $r_b = 10^{-4}$  and  $r_{ice} = 0$  everywhere.

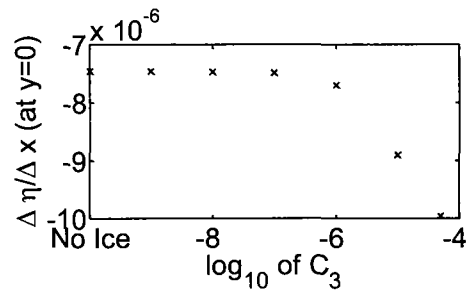


Figure 1.9. Normalized along-shore sea level slope ( $\text{m}^{-1}$ ) versus the magnitude of the cross-shore variability of ice-ocean friction coefficient ( $\text{m s}^{-1}$ ). The friction coefficient is constant in the along-shore direction;  $(r_{ice} + r_b) = 10^{-2} (10^{-1} + C_3 y)^2$ . For  $\log_{10} (C_3) \approx -4$  the combined ice and bottom friction coefficient varies between  $10^{-4} \text{ m s}^{-1}$  at the coast and  $1.4 \times 10^{-3} \text{ m s}^{-1}$  at the ice edge. No ice indicates the case where  $r_b = 10^{-4}$  and  $r_{ice} = 0$  everywhere.

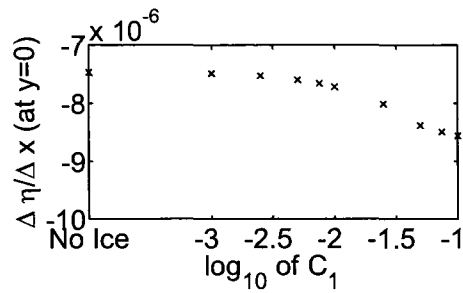


Figure 1.10. Normalized along-shore sea level slope ( $\text{m}^{-1}$ ) versus the magnitude of the along-shore variability of ice-ocean friction coefficient ( $\text{m s}^{-1}$ ). The ice-ocean friction coefficient does not vary in the cross-shore direction so

$(r_{ice} + r_b) = 10^{-2} [10^{-2} + C_1 \sin(mx)]$ . The friction coefficient varies between  $10^{-4} \text{ m s}^{-1}$  at the western boundary and  $10^{-3} \text{ m s}^{-1}$  at the middle of the domain with  $C_1 = 10^{-1}$ . No ice indicates the case where  $r_b = 10^{-4}$  and  $r_{ice} = 0$  everywhere.

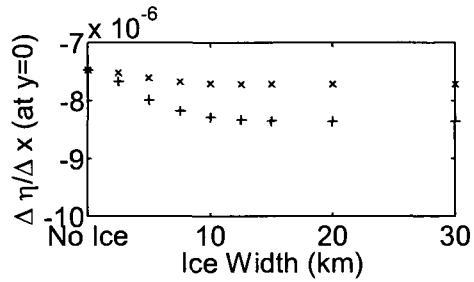


Figure 1.11. Normalized along-shore sea level slope ( $m^{-1}$ ) versus ice width (km). The x's mark experiments where  $(r_{ice} + r_b) = [C_0 + C_1 \sin(mx)](C_2 + C_3 y)^2$  so the magnitude of the combined ice-ocean and bottom friction coefficient increases with increasing ice width. The + signs mark the experiments where  $r_{ice} = 10^{-4} m s^{-1}$  so the ice-ocean friction coefficient does not change with changing ice width ( $r_{ice} + r_b = 2 \times 10^{-4} m s^{-1}$ ). For a variable ice-ocean friction coefficient the along-shore sea level slope is constant for ice widths greater than 30 km whereas for a constant ice-ocean friction coefficient the along-shore sea level slope changes between 30 and 40 km but is constant thereafter. No ice indicates the case where  $r_b = 10^{-4}$  and  $r_{ice} = 0$  everywhere.

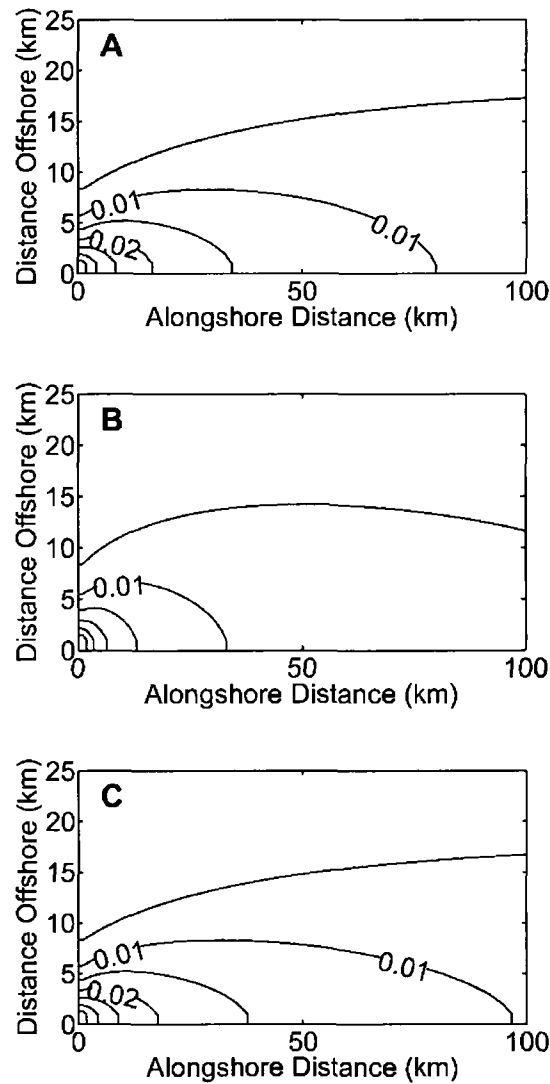


Figure 1.12. Contours of  $\eta$  (m) from numerical results. (A) The combined ice-ocean and bottom friction coefficient is  $(r_{ice} + r_b) = [C_0 + C_1 \sin(mx)](C_2 + C_3 y)^2$ . (B) The ATW solution; the friction coefficient is constant everywhere and is  $2 \times 10^{-4} \text{ m s}^{-1}$ . (C) The ice-ocean friction coefficient is constant ( $r_{ice} = 10^{-4} \text{ m s}^{-1}$ ) and ice covers the area inshore of the 20 m isobath ( $r_b = 10^{-4} \text{ m s}^{-1}$  everywhere).

### 1.9 Tables

Table 1.1. Range of ice parameters considered. The range of  $r_{ice}$  considered is  $0 - 10^{-3}$  m  $s^{-1}$ .

	$C_0$	$C_1$	$C_2$	$C_3$	$m=2\pi/M$ ( $M$ , km)	Ice Width ( $L$ , km)
Basic ALW	$10^{-2}$	$10^{-2}$	$10^{-1}$	$10^{-6}$	$M=1200$	26
Analytical	$10^{-3}-10^{-1}$	$10^{-3}-10^{-1}$	$10^{-3}-10^{-1}$	$10^{-6}-10^{-7}$	$M=100-600$	5-60
Numerical	$10^{-3}-10^{-1}$	$10^{-3}-10^{-1}$	$10^{-3}-10^{-1}$	$5*10^{-5}-10^{-7}$	$M=200-1200$	10-60

Table 1.2. Eigenvalues of the analytic landfast model for the basic analytical ALW solution, constants as given in Table 1.1.

$\lambda$	$(l-n)$
-37.5	0
-165.5	0
-1498.5	-1
-2678.0	-2
-4208.0	-3
-6093.8	-4
-8339.2	-5
-10947.2	-6
-13919.7	-7



## Chapter 2 Modeling winter circulation under landfast ice: The interaction of winds with landfast ice<sup>1</sup>

### *Abstract*

Idealized process models and a simple vertically-averaged vorticity equation are used to elucidate the effects of an upwelling wind and a spatially variable landfast ice cover on the circulation beneath landfast ice. In the case of no along-shore changes in ice, upwelling winds seaward of the ice edge result in: 1) a decrease in sea level at the coast and ice edge, 2) a cross-shore sea level slope that drives an under-ice, geostrophic flow in the upwind direction, 3) a strong jet flowing downwind offshore of the ice edge, and 4) offshore transports in the under-ice and bottom boundary layers that remove water from beneath the landfast ice. This transport leads to a coastal sea level drop of  $\sim 1.3$  m in 10 days for  $7 \text{ m s}^{-1}$  winds. The upwind under-ice current accelerates quickly over several days and then slows as cross-shore transport leads to a decrease in the cross-shore sea level slope with time. Near the ice edge bottom boundary layer convergence results in an upwelling frontal structure that induces ice-edge exchange at the surface and above the bottom boundary layer. Along- and cross-shore variations in ice width and under-ice friction ( $r_{ice}$ ) affect the magnitude and duration of under-ice currents and relationships between under-ice currents, sea level and offshore winds. For example, along-shore

---

<sup>1</sup> Kasper, J.L., Weingartner, T.J., Modeling winter circulation under landfast ice: The interaction of winds with landfast ice, prepared for submission to Continental Shelf Research.

variations in  $r_{ice}$  can create along-shore currents ( $> 0.03 \text{ m s}^{-1}$ ) beneath landfast ice.

Along-shore changes in landfast ice width, when subject to spatially uniform along-shore winds, generate sub-inertial, topographic waves that propagate along the coast in the Kelvin wave direction.

## ***2.1 Introduction***

Winds and river runoff influence the dynamics and circulation over continental shelves, particularly the innermost portion of the shelf (depths  $< \sim 20 \text{ m}$ ). While this is true for Arctic shelves as well, the effects of wind stress and buoyancy are substantially modulated by the annual freeze/thaw cycle, which controls the phasing and duration of the landfast ice season and river discharge (Weingartner et al., 2009). Nearshore circulation processes on arctic shelves differ from ice-free seas because of landfast ice, which covers the inner portion of arctic shelves for up to 9 months of the year. This ice is essentially immobile so it inhibits momentum transfer from the wind to the ocean and it exerts a frictional stress on the under-ice flow. Thus, the dynamical properties of the landfast ice zones surrounding the Arctic Ocean are quite different than those of ice-free shelves.

In the Alaskan Beaufort Sea (ABS), the circulation seaward of the landfast ice zone is vigorous ( $\sim 0.2 - 1 \text{ m s}^{-1}$ ) and wind-forced (e.g. Aagaard and Roach, 1990; Pickart et al., 2009), whereas on the inner shelf, under the landfast ice cover, currents are an order of magnitude smaller than on the wind forced outer shelf ( $\leq 0.05 \text{ m s}^{-1}$ ) and uncorrelated with local or regional winds (Weingartner et al., 2009). On the inner shelf,

under the landfast ice, the flow is controlled by along- and cross-shore pressure gradients (of uncertain origin) and frictional coupling with the underside of the ice and seabed.

The frictional coupling between landfast ice and the ocean is poorly understood. It likely depends on both the under-ice topography and current speed. For example, the under-ice topography on windward shelves, such as the ABS, is highly deformed due to collisions at the seaward boundary with the wind-driven pack ice. Ridging intensity and keel depths generally increase offshore and throughout the freezing season, although these features can vary substantially in the along-shore direction (Tucker et al., 1979). Further, the landfast ice width varies along the ABS (Mahoney et al., 2007). These considerations suggest that ice-water friction will also vary over a range of time and spatial scales and complicate the circulation response.

Shirasawa (1986) directly measured the ice-ocean drag coefficient beneath landfast ice in the Canadian Archipelago and found that the quadratic under-ice drag coefficient ranged between  $5 \times 10^{-3}$  for smooth ice and  $9 \times 10^{-3}$  for rough ice. McPhee (1990) found a similar range for pack ice, noted that the drag coefficient varied substantially over short distances, and attributed the variations to form drag (pressure drag) associated with deep ice keels. Shirasawa's (1986) values suggest the range for a linear ice-ocean friction coefficient ( $r_{ice}$ ) is between  $10^{-4}$  and  $10^{-3} \text{ m s}^{-1}$  (Chapter 1 of this thesis).

In a modeling study of the effect of landfast ice on an along-shore pressure gradient, we used a vertically-averaged, linear, steady-state vorticity equation that mimics the effects of landfast ice by imposing a surface stress (no-slip condition) on the ocean

surface (Chapter 1 of this thesis). The stress is assumed to be related to the under-ice velocity through  $r_{ice}$ , which was allowed to vary in both the along- and cross-shore directions. Their vorticity equation, termed the arrested landfast ice topographic wave equation (ALW), was based on the “arrested topographic wave” (ATW) model of Csanady (1978).

Here we use the ALW vorticity equation to examine the effect of a landfast ice cover on a sea level slope that extends across the landfast ice zone and that is established by offshore winds. While ice edge processes have been considered before, previous studies (e.g. Gammelsrod et al., 1975; Clarke, 1978; Fennel and Johannessen, 1998) concentrated on wind-forced motions near the ice edge rather than the circulation beneath the ice. In addition, they assumed a constant bottom depth and that the ice edge was far from any coastal boundaries. They also ignored along- and cross-shore ice variations and under-ice friction. Herein, we focus on the response of nearshore circulation beneath immobile landfast ice to offshore winds and how spatial variations in ice extent and in under-ice friction affect this response. The paper proceeds as follows: section 2.2 describes the governing (ALW) vorticity equation. Numerical simulations of flow under landfast ice driven by a cross-shore sea level slope between the coast and the ice edge due to offshore winds are described in section 2.3. Section 2.4 discusses relevant observations and summarizes the paper.

## 2.2 *The governing vorticity equation*

To demonstrate the first-order effect of landfast ice on inner shelf circulation an analytic description of mean barotropic subtidal flow beneath landfast ice was developed following Csanady's (1978) ATW model. The ATW vorticity equation models the effects of a sloping, frictional bottom on the mean coastal flow. For the ALW, we modify the ATW governing equations, the steady state vertically-averaged momentum equations under the long wave approximation to include landfast ice as a surface stress. This stress is analogous to placing a bottom boundary layer on the ocean surface. We present a simple solution to the ALW vorticity equation, which illustrates the effect of under-ice friction on the sea level anomaly beneath the ice.

Our model domain is a rectangle bounded by a straight coastline along the southern boundary ( $y = 0$ , with  $x$  being the along-shore coordinate; Figure 2.1A). The northern boundary is the landfast ice edge ( $y = L$ , with  $L$  the width of the landfast ice). Figure 2.1B is the numerical model domain, which encompasses the entire shelf (the inner shelf under the landfast ice and the area offshore of the ice edge). For simplicity we assume bottom depth,  $h$ , increases linearly with distance offshore ( $h = sy$ ,  $s = 7.5 \times 10^{-4}$ , the approximate slope of the ABS). Bottom and under-ice friction are linearly related to the depth averaged under-ice transport. The governing steady state equations are:

$$\left. \begin{aligned}
 -fv &= -g \frac{\partial \eta}{\partial x} + \frac{-(r_{ice} + r_b)u + F_x}{h} && \text{along-shore momentum} \\
 fu &= -g \frac{\partial \eta}{\partial y} + \frac{-(r_{ice} + r_b)v}{h} && \text{cross-shore momentum} \\
 \frac{\partial(uh)}{\partial x} + \frac{\partial(vh)}{\partial y} &= 0 && \text{continuity}
 \end{aligned} \right\} \quad 2.1$$

$F_x$  is the wind stress in the along-shore direction (zero everywhere under the ice). Cross-shore velocity,  $v$ , is positive to the north, the along-shore velocity,  $u$ , is positive to the east,  $\eta$  is the sea level anomaly,  $r_b$  is the bottom friction coefficient, and  $f$  is the Coriolis parameter (taken as  $f = 1.37 \times 10^{-4} \text{ m s}^{-1}$  for  $\varphi = 70^\circ\text{N}$ ). Note the signs of the bottom and under-ice frictional stresses ( $-(r_{ice} + r_b)u/h$ ,  $-(r_{ice} + r_b)v/h$ ) are the same.

Following Csanady (1978) we assume the cross-shore stress,  $(r_{ice} + r_b)v/h$ , is small compared to the along-shore stress. The cross-shore momentum balance is then geostrophic:  $fu = -g \partial \eta / \partial y$ . Beneath the ice, the along-shore wind stress curl is zero (the ice edge boundary condition represents the effect of the wind stress curl at the ice edge). Taking the curl of the governing equations and neglecting the wind stress curl leads to the vorticity equation for the area under the landfast ice cover:

$$\frac{\partial \eta}{\partial x} = \underbrace{\frac{(r_{ice} + r_b)}{fs} \frac{\partial^2 \eta}{\partial y^2}}_{\text{Term 1}} + \underbrace{\frac{1}{fs} \frac{\partial(r_{ice} + r_b)}{\partial y} \frac{\partial \eta}{\partial y}}_{\text{Term 2}} \quad 2.2$$

Equation 2.2 is the ALW or under-ice vorticity equation. It describes the effects of bottom friction, rotation, a sloping bottom and spatial variability in the ice-ocean friction on the sea level anomaly beneath a landfast ice cover. The ALW vorticity shows how spatial variations in the ice-ocean friction affect the along-shore sea level slope,  $\partial \eta / \partial x$ .

The ALW vorticity equation is a parabolic differential equation, an advective-diffusive equation where the diffusion coefficient,  $\kappa = (r_{ice} + r_b)/fs$  may vary with position. In contrast, Csanady's (1978) ATW vorticity equation is a diffusion equation,

$$\frac{\partial \eta}{\partial x} = \frac{r_b}{fs} \frac{\partial^2 \eta}{\partial y^2}$$

with a constant diffusion coefficient,  $\kappa = r_b/fs$ . Term 1 of the ALW

vorticity equation is diffusive-like and describes vorticity changes due to the joint effects of a sloping bottom, rotation and under-ice and bottom friction. As in the ATW, diffusion is proportional to the cross-shore divergence of the along-shore geostrophic velocity. Hence under-ice friction can cause along- and cross-shore variation in the cross-shore divergence of the along-shore geostrophic transport. Term 2, which is advective-like, is the cross-shore gradient in ice friction multiplied by the along-shore geostrophic transport. The sign of  $\partial(r_{ice} + r_b)/fs \partial y$  is assumed positive for our setting since landfast ice roughness in the ABS generally increases with offshore distance (Tucker et al., 1979), which we mimic by increasing  $r_{ice}$  with distance offshore. The ALW vorticity equation shows that variations in the ice-ocean friction coefficient induce frictional torques on the water column.

In mid-latitude studies of wind-driven shelf circulation, the wind stress is often applied over the length of the shelf (e.g. as in Gill and Schumann, 1974, where the wind stress is applied as a boundary condition at the coast). Thus, in the ice-free case, steady state develops at the coast shortly after the onset of wind forcing (in shallow water) and propagates offshore with increasing time (towards deeper water). Since ice covers our domain, forcing must be applied elsewhere; in Chapter 1, we considered a geostrophic

inflow along the western boundary, upstream (in the Kelvin wave sense) of the domain. Herein we specify the forcing by prescribing the sea level at the offshore landfast ice-edge, i.e., the northern boundary of the model domain. In the landfast ice-covered case, the forcing signal then propagates shoreward from the ice-edge. The boundary condition at the coast is that there is no flux through the coast i.e.  $vh = 0$  at  $y = 0$ . When combined with the along-shore momentum equation in eq. 2.1, the coastal constraint implies that  $\partial\eta/\partial y = 0$  at  $y = 0$  (where we have set  $h = 0$  at  $y = 0$  and used the cross-shore momentum balance to set  $u = -(g/f)\partial\eta/\partial y$ ).

In the absence of along-shore variations in ice or winds ( $\partial\eta/\partial x = 0$ ) and a constant sea level at the ice edge ( $\eta = \eta_0$  at  $y = L$ ), a simple solution to the ALW vorticity equation is easily found. In this case the ALW vorticity equation, eq. 2.2, reduces to:

$$\frac{\partial}{\partial y} \left[ \frac{(r_{ice} + r_b)}{fs} \frac{\partial\eta}{\partial y} \right] = 0 \quad 2.3$$

To proceed, we assume that the friction coefficient varies in the cross-shelf direction as  $(r_{ice} + r_b) = C_1(C_2 + C_3y)^2$ , a parameterization that allows us to solve the ALW vorticity equation and which mimics the offshore increase in ice roughness, i.e. under-ice friction increases to a maximum at the ice edge. Integration of eq. 2.3 yields:

$$\eta = \frac{-fsC}{C_1C_3(C_2 + C_3y)} + c \quad 2.4$$

where  $C$  and  $c$  are integration constants. Application of the coastal constraint implies that  $C = 0$  so that  $\eta = \eta_0$  everywhere beneath the ice cover. Hence, in the absence of along-



shore changes in ice or winds, the ALW vorticity equation predicts that nearshore currents beneath landfast ice (driven by a surface stress curl across the ice edge) eventually decay to zero. Note that in the case of constant  $r_{ice}$ , the ALW vorticity equation reduces to the ATW vorticity equation. In this simplest of scenarios the solution is identical for both vorticity equations; no flow under the ice. Gammelsrod et al. (1975) obtained this result for their flat bottomed marginal ice zone setting, although their domain was infinite in extent and had no coast. This steady state results from transport towards the ice edge in both the surface and bottom boundary layers.

While this solution to the steady state ALW vorticity equation is particularly simple, numerical results show that the time evolution of under-ice currents is interesting and the cross-shore sea level slope is inversely related to the magnitude of the ice-ocean frictional coupling. This dependence is obvious from equations 2.3 and 2.4, which suggest that the under-ice sea level (and the cross-shore sea level slope) depends upon cross-shore variations in friction and the magnitude of the friction coefficient. Numerical results discussed next show that this is indeed the case and we can use the steady state ALW vorticity equation to help understand time dependent numerical models of along- and cross-shore variations of friction on the under-ice circulation.

## ***2.3 Numerical model results***

### **2.3.1 Model description**

To further elucidate the physics of ocean circulation beneath landfast ice, simple process-oriented numerical experiments were conducted with the Regional Ocean

Modeling System (ROMS; Song and Wright, 1998; Shchepetkin and McWilliams, 2005). ROMS is a finite difference, free surface model with stretched terrain following coordinates in the vertical ( $s$ -coordinate, Song and Haidvogel, 1994) used to solve the primitive equations. The  $s$ -coordinate is desirable when dealing with continental shelf topography and allows for increased resolution in the top and bottom boundary layers. The time stepping scheme is split between the fast (vertically-averaged) and slow (baroclinic) modes. Sensitivity studies (to ice parameters) were conducted with ROMS configured to solve just the vertically-averaged (2D) mode. ROMS variables are defined on a staggered "Arakawa C" grid (Arakawa and Lamb, 1977).

To study boundary layer transport under a landfast ice cover and to investigate exchange across the ice edge, we configured ROMS to solve the full set of coupled primitive equations for an unstratified water column beneath a landfast ice cover. For the three dimensional (3D) experiments we use the Mellor-Yamada level 2.5 (Mellor and Yamada, 1982) mixing scheme, where eddy diffusivity is calculated based upon the local flow and stratification. We used 40  $s$ -levels with the vertical levels stretched to maintain resolution in both the surface and the bottom boundary layers.

We tested the sensitivity of the results to horizontal resolution and found that the cross-shore sea level slope was insensitive to a 0.5 or 1 km resolution, but that a 0.5 km resolution was useful in studying the circulation near the ice edge in the 3D experiments. Therefore we used a resolution of 500 m and 1 km in the cross- and along-shore directions, respectively, in the 3D experiments and a uniform 1 km grid in the 2D

experiments. The non-linear advective terms are retained in both the vertically-averaged and 3D experiments.

As with the ALW vorticity equation, landfast ice enters the model experiments only through a surface stress that is linearly related to the under-ice velocity and we ignore changes in ice thickness. In the 3D experiments,  $\bar{\tau}_{surf} = -r_{ice} \bar{u}_{surf}$ . In the vertically-averaged numerical experiments surface stress is linearly related to the depth-averaged under-ice transport. Landfast ice extent is prescribed by choosing the spatial extent of  $r_{ice}$  and by applying a spatially uniform upwelling wind stress (an easterly,  $0.1 \text{ N m}^{-2}$  wind stress of  $\sim 7 \text{ m s}^{-1}$  ramped up over two days) everywhere  $r_{ice} = 0$ .

Figure 2.1B is a cartoon of the numerical model geometry. The bathymetry is again similar to the ABS and the bottom depths and slope are the same as in the analytical ALW solution although  $h_0$  is 0.1 m in the numerical model. The ROMS “WET\_DRY” option is employed to allow the sea level to drop below the coastal wall depth. The model domain is a 600 km long shelf, oriented east-west ( $0 < x < 600 \text{ km}$ ), with the coastal wall along the southern boundary. The cross-shore boundaries are periodic and no gradient conditions apply on all variables at the northern (or offshore) boundary. The cross-shore extent of the domain is 200 km (with the coast at  $y = 0$  and  $0 < y < 200 \text{ km}$ ). We ignore along-shore variations in topography and coastline orientation so that the modeled flows result only from physical processes associated with the imposed forcing and the under-ice stress parameterizations.

To mimic the cross-shore increase in under-ice roughness, we set

$$r_{ice} = C_1 (C_2 + C_3 y)^2 \text{ (in contrast to the ALW vorticity equation here the surface and}$$

bottom stresses are now specified separately; with  $r_b = 10^{-4}$ ). The range of values for  $C_1$ ,  $C_2$ ,  $C_3$ , and ice width considered is listed in Table 2.1 and the under-ice friction coefficients for different cases are shown in Figure 2.2. We refer to the 2D case with  $C_1=10^{-2}$ ,  $C_2= 10^{-1}$  and  $C_3=10^{-6}$  as the basic ALW-like numerical simulation. We contrast the variable under-ice friction coefficient experiments with ATW-like numerical simulations in which the under-ice friction coefficient does not vary across the shelf. We refer to the case where  $r_{ice} = 10^{-4} \text{ m s}^{-1}$  as the basic ATW-like numerical simulation. In the basic ALW-like numerical simulation, we examine small cross-shore variations in  $r_{ice}$  such that  $r_{ice} \sim r_b$ .

For most experiments, the ice edge parallels the coast (with landfast ice covering the area inshore of the 20 m isobath, so that in the basic case, wind stress is applied seaward of  $y \geq 26.5 \text{ km}$ ). Other experiments consider various ice widths. Note since the variables are discrete, for consistency we must somewhat arbitrarily define the location of the ice edge and in the basic case we take the ice edge to be  $y = 25.5 \text{ km}$ , one grid point shoreward of the first grid point over which the wind stress acts.

### 2.3.2 The basic vertically averaged experiments

The basic ALW- and ATW-like results shown in Figure 2.3 are similar to previous studies of ice edge upwelling (e.g. Gammelsrod et al., 1975 and others), which we comment on, but do not show in detail. Under upwelling winds and in the absence of along-shore variations in the under-ice friction coefficient, sea surface height is a minimum at the ice edge. The transition from immobile landfast ice to wind-driven flow

at the ice edge imposes a surface stress curl at the ice edge, which drives ice edge upwelling. Sea level at the ice edge decreases nearly linearly with time during the 10 day period considered. After 10 days the sea level at the ice edge is  $\sim -1.3$  m. Offshore of the ice edge, the sea level increases with distance. This results in a westward-flowing (downwind) ice-edge current jet (of  $\sim -1$  m s<sup>-1</sup> after 10 days). Note that in the basic cases, since there are no along-shore variations,  $\partial\eta/\partial x = 0$ .

For comparing the basic ALW- and ATW-like models we present the sea level differences between the coast and the ice edge (Figure 2.3A) and sea level anomaly as a function of distance from the coast (Figure 2.3B) after 10 days for the region under the landfast ice only. For only the basic ALW-like simulation we show the cross-shore sea level slope at the coast and at the ice edge (Figure 2.3C) and the along-shore velocity (Figure 2.3D) at the coast and the ice edge, all as a function of time.

The panels in Figure 2.3 suggest that the basic adjustment proceeds as follows. At  $t = 0$  upwelling winds initiate a decrease in sea level at the ice edge and the developing cross-shore sea level slope between the coast and the ice edge drives an upwind (eastward), under-ice geostrophic current. The ice and seabed induce frictional stresses on the along-shore flow that impels an offshore (towards the ice edge) cross-shore transport. Hence, adjustment propagates inshore from the ice edge. From Figure 2.3A, the maximum cross-shore sea level slope magnitude occurs at 2.5 days for the ALW-like model (2.75 days for the ATW-like model) when the forcing signal reaches the coast. Afterwards the cross-shore sea level slope decreases as the coastal sea level decreases more rapidly than the ice edge sea level. We define the frictional adjustment time,  $t_f$ , to be

the time between  $t = 0$  and when the cross-shore sea level reaches its maximum magnitude.

Figure 2.3B shows that the cross-shore sea level slope depends upon the form of the under-ice friction coefficient, which exerts its largest influence on coastal sea level. For the case of constant friction (the ATW-like model) the coastal sea level is  $O(10^{-3} \text{ m})$  higher than for the variable friction coefficient, ALW-like model, although the ice edge sea level is identical in both cases.

Figure 2.3C shows that throughout the 10-day run, the magnitude of the cross-shore sea level slope is a minimum at the coast and largest at the ice edge. The time evolution of the along-shore upstream geostrophic velocity (Figure 2.3D) reflects the time and spatial variation of the cross-shore sea level slope. Initially the along-shore upstream velocity increases everywhere (but most rapidly near the ice edge). After frictional adjustment, the along-shore under-ice velocity decreases. The smallest along-shore velocities ( $<0.01 \text{ m s}^{-1}$ ) are at the coast, and the largest velocities (maximum  $\sim 0.03 \text{ m s}^{-1}$ ) are at the ice edge. By day 10, the cross-shore sea level slope between the coast and the ice edge is  $-1.1 \times 10^{-7}$ , resulting in a mean along-shore geostrophic velocity of  $0.008 \text{ m s}^{-1}$ .

Before considering numerical experiments to examine how different values of the ice parameters affect the under-ice circulation and sea level we note that the terms included in the analytical vorticity equation are not the only important vorticity tendencies. Near the coast, the numerical experiments indicate that the cross-shore stress terms (neglected in the analytic treatment but retained in the appendix, e.g. see the second

of eq. A.2.2) are  $\sim$  two orders of magnitude larger than the along-shore stress terms. As shown in the appendix, the cross-shore stress contributes an extra term to the vorticity balance

$$0 = \frac{1}{sf} \frac{\partial}{\partial y} \left[ (r_{ice} + r_b) \frac{\partial \eta}{\partial y} \right] - \frac{r}{fh} \frac{\partial \eta}{\partial y} \quad 2.5$$

Cross-shore  
Stress Term, term 3

Eq. 2.5 shows that contribution of the cross-shore stress increases as the sea level at the coast decreases with time because this vorticity term is inversely proportional to depth,  $h$ . Moreover, the cross-shore stresses are negative at the coast (directed onshore) and so reduce transport away from the coast. Elsewhere, the cross-shore stress terms are small and their curl is negligible beneath the ice cover. The discontinuities evident in Figures 2.3C-D are due to the cross-shore stress terms and the ROMS “WET\_DRY” algorithm. At day 3.75 the sea level anomaly drops below the sea level at the grid point nearest the coast. As a result the cross-shore stress terms abruptly increase and this change is reflected in the cross-shore sea level slope and velocities. The numerical solution also includes the non-linear advective terms. These increase the offshore transport under the ice slightly so that the sea level everywhere under the ice is lower, by  $O(10^{-3} \text{ m})$  after 10 days, than for a comparable linearized experiment.

### 2.3.3 Three dimensional results

While vertically-averaged experiments are helpful in understanding the vorticity tendencies, the 3D results (which include the non-linear terms) allow a detailed examination of the under-ice velocity structure (Figures 2.4-2.7). Figure 2.4A (2.4B) is

the along-shore (cross-shore) velocity between the coast and 25.75 km offshore 10 days after the onset of the wind. (In these 3D results, the ice edge is 25.75 km offshore and the wind is applied 26.25 km from the coast, i.e., 0.5 km seaward of the area shown in Figures 2.4-2.7). The along-shore, under-ice flow is eastward (upwind) and geostrophic with velocities diminishing from  $\sim 0.06 \text{ m s}^{-1}$  near the ice-edge to less than  $0.01 \text{ m s}^{-1}$  within 10 km of the coast. Under-ice cross-shore velocities (Figure 2.4B) are offshore within the surface and bottom boundary layers and near the ice edge, but weakly onshore at mid-depths. Figure 2.4B suggests that the water that escapes from under the ice cover is derived mainly from within and slightly above the bottom boundary layer. Particle trajectories discussed below confirm this.

Figure 2.5A shows vertical profiles of the along- and cross-shore velocities over the 19 m isobath (24.75 km from the coast and 1 km inshore of the ice edge). The vertical profiles in Figure 2.5B are from the 10 m isobath, midway between the ice edge and the coast. Surface and bottom friction result in a parabolic along-shore velocity profile with a mid-depth maximum similar to pipe flow (e.g. Kundu and Cohen, 2008). Over the 10 m isobath (Figure 2.5B), the vertical  $u$  profile is nearly parabolic whereas at the 19 m isobath, the water is deep enough that the boundary layers do not overlap. Note, that the surface and bottom boundary layers are not symmetric because the bottom boundary is sloping whereas the surface boundary is nearly flat (although not completely because of the sea surface slope).

The maximum cross-shore velocities are just below (above) the surface (bottom) boundary layers. Over the 19 m isobath, the cross-shore velocity is small but onshore



(negative) between 7-15 m depth and offshore (positive) elsewhere. Nevertheless, the cross-shore transport is positive indicating that offshore boundary layer transport is not balanced by onshore transport in the interior. Over the 10 m isobath (Figure 2.5B) the cross-shore velocities are positive everywhere. Hence the vertically-averaged cross-shore transport is offshore everywhere inshore of the ice edge, which leads to a continuous drop in under-ice sea level throughout the 10-day period.

Seaward of the landfast ice edge the cross-shore velocity component in the bottom boundary layer is onshore ( $\sim 0.03 \text{ m s}^{-1}$ ). Hence at the ice edge, the bottom boundary layer cross-shore transports converge and feed upwelling shoreward of the ice edge. This results in a bottom to surface circulation cell that partially blocks offshore transport in the surface boundary layer. This is visible in the contours of vertical velocity,  $w$ , and cross-shore velocity,  $v$  spanning the ice edge (Figure 2.6A and B respectively). Slightly shoreward of the ice edge,  $w$  is positive but farther inshore, the offshore surface boundary layer transport under the ice encounters the upwelling front and is forced downwards and forms a vertical circulation cell. The convergence in the surface boundary layer is visible in Figure 2.6B at  $y = 25 \text{ km}$ . In the bottom boundary layer there is convergence at  $y \approx 25.5 \text{ km}$ . Seaward of the ice edge, surface transport is offshore and bottom boundary layer transport is onshore. Figure 2.6C shows the along-shore velocity across the ice edge. Inshore of the ice edge, the velocity is weakly upwind ( $\sim 0.06 \text{ m s}^{-1}$  maximum). Offshore of the ice edge, the velocity is downwind ( $\sim -1 \text{ m s}^{-1}$ ).

Neutrally buoyant (dynamically passive) particles reveal the complexity of cross-shore transport under the landfast ice cover. In general because of the increase in both the

along- and cross-shore velocity with increasing distance from the coast, particle displacement increases with distance offshore. Though not shown, by day-10 particles released 2 km from the coast move a maximum of 2 km farther offshore and 5 km eastward (in the surface and bottom boundary layers), whereas particles released in the surface and bottom boundary layer 12 (15) km from the coast move 2 (4) km offshore and 15 (20) km to the east while sinking by  $\sim 1$  m.

Particle displacement also depends upon the initial depth at which the particles are released. Particles released in the interior (slightly below or above the surface and bottom boundary layers where the cross-shore velocities are largest) are not necessarily displaced the most. Rather, displacement magnitude is largest for particles that cross the ice edge. Figure 2.7A shows a plane view of 10-day particle trajectories for particles released at  $x = 50$  km,  $y = 24$  km (or 2.25 km inshore of the ice edge) along the  $\sim 19$  m isobath. All the particles that cross the ice edge were released between 12-15 m depth, above the bottom boundary layer. These particles initially move offshore, eastward, and upwards until they enter the ice edge jet, where they are rapidly swept westward and offshore in the wind-driven surface layer. Overall, 75% of particles released 24 km offshore of the coast (at depths below 10 m) transit across the ice edge, while the remainder do not escape from beneath the ice.

Figure 2.7B shows the trajectories of particles in the cross-shore plane. These were released near  $y = 24$  km (and within the grey box). Again, the ice edge is located at  $y = 26.25$  km. Particles released within the black box do not cross the ice edge during the 10-day run but instead move out of the page. In contrast, particles initialized outside of

the black box cross the ice edge and then move into the page after escaping from the landfast ice zone and entering the ice edge jet. A very small number of particles released at the surface also cross the ice edge and enter the jet, whereas particles released just below the surface remain inshore of the ice edge and move  $\sim 23$  km eastward in 10 days. Initially these particles sink by  $\sim 2$  m and move offshore until they encounter the upwelling front inshore of the ice edge. Thereafter they move eastward (and slowly rise).

Particles released 21 km from the coast do not reach the ice edge during the 10 day period considered. Farther inshore, particles released at mid depths ( $> 6$  m and 18 km from the coast) move eastward with very little offshore movement. Overall, given the small current velocities near the coast, these models suggest that contaminants released in the nearshore environment would not travel far under a landfast ice cover and that exchange processes across the jet are limited.

### 2.3.4 Sensitivity results

We next examine the effects of various landfast ice parameters on the under-ice cross-shore sea level slope using vertically-averaged experiments. Figures 2.8-2.10 summarize the results after 10 days of a  $7 \text{ m s}^{-1}$  upwelling wind offshore of the ice edge and no along-shore variations in friction. We show the cross-shore sea-level slope ( $\Delta\eta / \Delta y$ ) between the coast and the ice edge and  $t_f$ , the time required to achieve the maximum cross-shore sea level slope. In constructing these figures we compute the sea level slope as simply the sea level difference between the coast and the ice edge divided by the 25 km width of the landfast ice zone (taking into account the grid staggering).

Figure 2.8A shows  $\Delta\eta/\Delta y$  for the ATW-like model for spatially constant  $r_{ice}$  (black circles) and for the ALW-like variable friction coefficient model (blue crosses) where  $r_{ice} = C_I (10^{-1} + 10^{-6} y)^2$ . For the ATW-like model the  $x$ -axis is the  $\log_{10}$  of  $r_{ice}$ , so that  $\log_{10}(r_{ice}) = -4$  is the basic ATW-like numerical solution. For the ALW-like simulations the  $x$ -axis is the  $\log_{10}$  of  $C_I$ , so that for  $\log_{10}(C_I) = -2$ ,  $C_I = 10^{-2}$  and  $r_{ice} \sim 10^{-4}$  (the basic ALW-like numerical solution). Figure 2.8B shows  $t_f$  for both the ATW-like simulations (black circles) and for the ALW-like simulations (blue crosses), where the  $x$ -axes are the same as in Figure 2.8A. The basic ATW- and ALW-like numerical solutions are indicated by the boxed points.

In accordance with the simplified vorticity equation, eq. 2.4, the results show that as the under-ice friction coefficient increases, the magnitude of the cross-shore sea level slope decreases. The change in slope is associated with changes in  $t_f$ , which decreases as  $r_{ice}$  increases. In addition, the cross-shore sea level slope magnitude is consistently larger (though the difference is small) for the constant (ATW-like) friction coefficient compared to the variable (ALW-like) friction coefficient with similar overall magnitude. Hence, if  $r_{ice}$  increases seaward,  $t_f$  is less than for a constant  $r_{ice}$  of similar magnitude. The reason for this is discussed below in relation to the vorticity terms. The differences in cross-shore sea level slope seen among the experiments result primarily from variations in the coastal sea level. For example, for the constant  $r_{ice}$  (Figure 2.8A) the coastal sea level ranges between -1.3008 m ( $r_{ice} = 0$ ) and -1.3068 m ( $r_{ice} = 10^{-3}$ ), whereas sea level at the ice edge varies only between -1.3083 and -1.3085 m. Also the total transport across the

ice edge ( $T$ ,  $vh$  integrated over 10 days and over the length of the domain, 600 km) increases with the magnitude of  $r_{ice}$ ; in the basic ATW- (ALW-) like model  $T = 2.2442 (2.2452) \times 10^{10} \text{ m}^3$ . For  $r_{ice} \sim O(10^{-3} \text{ m s}^{-1})$   $T = 2.2474 \times 10^{10} \text{ m}^3$  for both the ATW- and ALW-like simulations, a difference of  $< 1 \%$ . Overall, cross-shore transport removes  $\sim 14 \%$  of the under-ice fluid volume over 10 days.

We next use the vertically-averaged experiments to examine the effect of changes in the magnitude of  $C_3$  on cross-shore sea level slope (Figure 2.9A) and  $t_f$  (Figure 2.9B). These parameters are plotted against the  $\log_{10}$  of  $C_3$  ( $r_{ice} = 10^{-2} (10^{-1} + C_3 y)^2$ ). The basic ALW-like numerical solution (where  $r_{ice} = 10^{-2} (10^{-1} + 10^{-6} y)^2$ ) is indicated by the rectangles. Overall, the effects of different gradients in  $r_{ice}$  are relatively small compared to the effects associated with changes in the magnitude of  $r_{ice}$ . The cross-shore sea level slope magnitude is inversely proportional to  $\partial r_{ice} / \partial y$ , i.e., the larger the gradient the smaller the cross-shore sea level slope. The frictional adjustment time,  $t_f$  decreases with an increase in  $\partial r_{ice} / \partial y$  as well. This is consistent with our simplified vorticity equation (eq. 2.4), which shows that a decrease in  $\partial r_{ice} / \partial y$  must be balanced by an increase in the cross-shore sea level slope. Once again the differences in  $\Delta \eta / \Delta y$  are primarily due to differences in coastal sea level. For the range of  $C_3$  shown in Figure 2.9, the coastal sea level varies between -1.3048 m and -1.3072 m for  $C_3 = 10^{-8}$  and  $C_3 = 10^{-5}$ , respectively. Total transport across the ice edge,  $T$  increases with the gradient in the ice-ocean friction coefficient. In the basic case  $T = 2.2452 \times 10^{10} \text{ m}^3$  and when  $C_3 = 10^{-5}$ ,  $T = 2.2474 \times 10^{10} \text{ m}^3$  (the same as for  $r_{ice} \sim O(10^{-3})$  shown in Figure 2.8).

In Figure 2.10 we examine how changes in landfast ice width affect the under-ice cross-shore sea level slope (blue curves) between the coast and the ice edge and coastal sea level (green curves). In Figure 2.10A,  $r_{ice} = 10^{-2} (10^{-1} + 10^{-6} y)^2$  (the basic ALW-like case) while in Figure 2.10B  $r_{ice} = 10^{-4} \text{ m s}^{-1}$  (the basic ATW-like case). Figure 2.10C is the same as Figure 2.10B, but for a flat ocean bottom with a constant depth of 20 m. Figures 2.10A and B indicate that the cross-shore sea level slope magnitude increases with increasing ice width. The change is linear for constant  $r_{ice}$  while for a variable  $r_{ice}$ , the cross-shore sea level slope approaches a constant value as ice widths exceed  $\sim 40$  km. The reason for the difference is described below in the discussion of the vorticity terms. Also,  $T$  is larger when the friction coefficient varies across the shelf than when the friction coefficient is constant (and the difference increases with ice width). When  $L = 72$  km,  $T = 3.6792 (3.6968) \times 10^{10} \text{ m}^3$  for the constant and variable  $r_{ice}$ , respectively, or  $\sim 1.5$  times  $T$  for the basic cases where  $L$  is 25 km.

Since the bottom depth at the ice edge increases as ice width increases, the upwelling response varies with ice width. For example, after day-10 the sea level at the ice edge is -1.5 (-0.8) m for a 7 (72) km wide ice cover. For the linearly sloping bottom considered herein, the relationship between sea level decrease at the ice edge and ice width is linear. In addition to changes in the depth of upwelling,  $t_f$  increases linearly with ice width (ranging from 2 - 4 days for a variable  $r_{ice}$  and 2 - 5.5 days for a constant  $r_{ice}$ ).

In contrast to the results shown in Figures 2.10A and 2.10B neither the depth of upwelling or  $t_f$  change with ice width for a flat bottom (Figure 2.10C). In this case  $t_f$  is 3.25 days over the range of ice widths considered. A comparison of Figures 2.10B and

2.10C shows that cross-shore sea level slopes are similar in both cases. But while the range in coastal sea level is nearly the same ( $\sim 0.6$  m) in both cases, the coastal sea level decrease in the flat bottom case exceeds that for the sloping bottom by  $\sim 0.7$  m. The reasons for this difference are that the sloping bottom opposes offshore transport from the coast and, in the case of a flat bottom, the depth at the coast is 20 m so that the cross-shore stress terms are unimportant.

Collectively, Figure 2.10 demonstrates that the change in cross-shore sea level slope and coastal sea level with ice width is primarily a function of time required to remove fluid from beneath the ice. When the ice is wide the sea level at the coast remains higher because more cross-shore transport and time are required to lower the coastal sea level (though the upwelling depth changes with ice width as well). The increase in cross-shore sea level slope with ice width is a result of the greater difference in sea level between the coast and the ice edge.

### 2.3.5 The vorticity terms

While the cross-shore sea level slope, coastal sea level and  $t_f$  concisely summarize the behavior of the solutions, the vorticity terms, which depend on the magnitude and distribution of  $r_{ice}$ , determine how these factors vary with changes in ice parameters and how the sea level and cross-shore sea level slope change with time. From the appendix the time-dependent vorticity balance, eq. A.2.4, is

$$\frac{f}{sg} \frac{\partial \eta}{\partial t} = \frac{1}{sf} \frac{\partial}{\partial y} \left[ (r_{ice} + r_b) \frac{\partial \eta}{\partial y} \right] - \underbrace{\frac{(r_{ice} + r_b)}{fh} \frac{\partial \eta}{\partial y}}_{\text{Term 3 due to cross shore stress}} \quad 2.6$$

where we ignore along-shore variations but include the cross-shore stress contribution (the last term on the right hand side), which we refer to as term 3. The first term on the right hand side involves both the diffusive-like and advective-like vorticity terms.

Figure 2.11A shows the cross-shore distribution of the diffusive-like vorticity term from the basic ATW solution ( $r_{ice} = 10^{-4}$ ) versus time. Figure 2.11B (C) is the cross-shore distribution of the diffusive-like (advective-like) vorticity term from the basic ALW solution through time. Note the spatial differences between the ATW and ALW diffusive terms. The ATW diffusive term expands farther offshore (with time) though the magnitude of the diffusive terms is largest near the coast. The diffusive ATW term has slightly larger magnitude ( $-3.9 \times 10^{-8}$  versus  $-3.5 \times 10^{-8}$ ) than the ALW diffusive term. The discontinuity visible at the coast at day 3.75 is due to the cross-shore stresses (shown in Figure 2.11D and discussed below) generated by the decreasing sea level at the coast, which affects the vorticity balance here. Although not shown, as the cross-shore gradient in  $r_{ice}$  increases, the ALW diffusive vorticity distribution becomes more constrained to the coast (and the maximum persists near the coast for a longer time period). The peak value in the diffusive term also occurs earlier for larger cross-shore frictional gradients (in accordance with the decrease in  $t_f$  with an increase in the ice friction gradient). Similar behavior is observed as the magnitude of  $r_{ice}$  increases (for both the ATW and ALW diffusive-like terms). While the shape of the distribution changes with variations in the ice parameters the magnitude of the diffusive term only decreases slightly ( $< 1.5 \times 10^{-8}$  over the range of  $r_{ice}$  considered).



In contrast to the diffusive vorticity terms, the advective-like vorticity term is largest at the ice edge and in the basic case its contribution to the vorticity balance is  $\sim 1/4$  that of the diffusive term ( $-1 \times 10^{-8}$  versus  $\sim -4 \times 10^{-8}$ ). Since the advective-like vorticity term varies with  $\partial r_{ice}/\partial y$ , an increase in the gradient of the friction coefficient increases the magnitude of this term and it achieves its maximum magnitude earlier.

Term 3, due to the cross-shore stress terms, is shown in Figure 2.11D (from the basic ALW-like simulation). Note that the sign of term 3 in Figure 2.11D is the same as the other vorticity terms; however, since in the vorticity balance the sign is opposite the other terms, term 3 buffers the other vorticity tendencies. At its maximum, term 3 is  $O(10^{-7})$  and about twice the magnitude of the diffusive-like terms. The magnitude of term 3 initially increases with time and then abruptly decreases (at day 3.75) as the coastal boundary shifts one grid point offshore (due to the ROMS “WET\_DRY” algorithm). The third term is similar in both the ATW- and ALW-like models. Hence the differences in cross-shore sea level slope and coastal sea level between the two models are primarily a result of differences in the diffusive-like vorticity term. The differences between the ALW and ATW diffusive terms are a result of the small but important differences in the overall vorticity balance introduced by the gradient in under-ice friction. Although not shown, the local vertical displacement,  $\frac{f}{sg} \frac{\partial \eta}{\partial t}$ , reflects the sum of the three vorticity terms; initially this term is large but slows after  $\sim t_f$  (2.5 days). Its spatial distribution varies as expected with the ice parameters and the  $t_f$ .

Interestingly, the distribution of the diffusive- and advective-like vorticity terms does not substantially change with ice width. However, for wider ice widths, the magnitude of the bottom stress vorticity term (term 3) is small because the sea level at the coast remains relatively high. The difference in cross-shore sea level slope noted between Figure 2.10 A and B can be understood from consideration of the vorticity terms 1 and 2 (the diffusive- and advective-like terms), which show that when the ice is wide, the diffusive vorticity term is small except near the coast (the distribution is similar to Figure 2.11 A and B). In contrast, the relatively smaller advective term is still small (and largest at the ice edge). As ice width increases, the influence of the diffusive term decreases (with distance from the coast) and the smaller advective term becomes important with increasing ice width. The effect is the smaller change in cross-shore sea level slope with increasing ice width visible in Figure 2.10 A (compared to 2.10B).

Overall, the numerical experiments show that the cross-shore sea level slope and the time-dependent response of the circulation beneath a landfast ice cover depend upon both the magnitude and the cross-shore profile of the  $r_{ice}$ . A larger diffusion coefficient or a greater cross-shore gradient in  $r_{ice}$  leads to a decrease in  $t_f$  and a smaller cross-shore sea level slope after 10 days (i.e., an increase in transport across the ice edge). These changes are a result of differences in the vorticity terms, which determine the change in coastal sea level and transport across the ice edge. The numerical simulations also show that ice width (and to a lesser extent the isobath that the ice edge occupies) is important. Finally, the cross-shore stress terms are substantial within  $\sim 5$  km of the coast and contribute to the vorticity balance under a landfast ice cover.

### 2.3.6 Along-shore variations in under-ice friction

We can surmise from the preceding results that along-shore differences in under-ice friction should lead to along-shore sea level slopes beneath landfast ice. We consider this by examining the response to a spatially uniform,  $7 \text{ m s}^{-1}$  upwelling wind offshore of the landfast ice for the case where the under-ice friction coefficient varies along the shelf according to:  $r_{ice} = [10^{-2} + 10^{-2} \sin(mx)]10^{-2}$ . (We have also run experiments in which  $r_{ice} = [C_0 + C_1 \sin(mx)](C_2 + C_3 y)^2$ , but these show only small differences compared to the case where  $r_{ice}$  varies only in the along-shore direction and so are not discussed.) The results are shown in Figure 2.12, with panels A-D based on  $m = \pi/75 \text{ km}^{-1}$  and panels E-H based on  $m = \pi/150 \text{ km}^{-1}$ . In both cases,  $0 < r_{ice} < O(10^{-4} \text{ m s}^{-1})$ . The resultant sea level pattern recalls the “shelf circulation cells” associated with a spatially periodic windstress along a coast (Csanady, 1981), with the cell wavelength a function of  $m$ . The pattern develops as a result of along-shore differences in transport due to the along-shore variations in  $r_{ice}$ . Near the ice edge, where  $\partial r_{ice} / \partial x$  is maximum (e.g. at  $x \approx 150 \text{ km}$  for  $m = \pi/75 \text{ km}^{-1}$  and  $x = 300 \text{ km}$  for  $m = \pi/150 \text{ km}^{-1}$ ) the cross-shore transport at the ice edge is a maximum. Whereas when  $\partial r_{ice} / \partial x$  is near zero (where  $r_{ice} = 0$  e.g. at  $x \approx 115 \text{ km}$  for  $m = \pi/75 \text{ km}^{-1}$  and  $x = 225 \text{ km}$  for  $m = \pi/150 \text{ km}^{-1}$ ), the cross-shore transport at the ice edge is negative (onshore) and relatively large. At the coast, the cross-shore transport changes sign near where  $r_{ice} = 0$ .

The development of along-shore currents with along-shore differences in ice can be understood by examination of the complete steady state under-ice vorticity balance which, from the appendix (eq. A.2.7), is

$$\frac{\partial \eta}{\partial x} = \frac{1}{gs} \left[ \underbrace{(r_b v)_x - (r_b u)_y}_{\text{Bottom Stress Curl}} + \underbrace{(r_{ice} v)_x - (r_{ice} u)_y}_{\text{Surface Stress Curl}} - \underbrace{(F_y)_x - (F_x)_y}_{\text{Wind Stress Curl}} \right] \quad 2.7$$

Along Shore  
Sea Level  
Slope

where the  $x, y$  subscripts denote partial differentiation. In the absence of along-shore changes in ice or winds  $\partial \eta / \partial x = 0$ , so for an along-shore sea level slope to develop either the wind or under-ice friction must vary along the shelf. Indeed, the vorticity balance indicates that sufficiently large  $(r_{ice} v)_x$  will establish an along-shore sea level slope and Figure 2.12 confirms this supposition. The numerical results show that near the ice edge, slightly up- and downstream of where  $\partial r_{ice} / \partial x$  is maximum,  $(r_{ice} v)_x$  and  $(r_{ice} u)_y$  are both  $O(10^{-7})$ .

The along-shore velocity,  $u$ , at the coast varies inversely with  $m$ ; the minimum  $u$  is  $\sim -0.03 \text{ m s}^{-1}$  for  $m = \pi/75 \text{ km}^{-1}$  and the minimum  $u$  is  $\sim -0.06 \text{ m s}^{-1}$  for  $m = \pi/150 \text{ km}^{-1}$ . This is consistent with eq. 2.7, which indicates that the along-shore sea level slope is proportional to the curl of the surface and bottom stresses and that  $u \sim 1/m$ . Additional experiments indicate that if the wavelength of the along-shore under-ice variations is  $< \sim 32 \text{ km}$  (the barotropic Rossby radius in 2 m of water), then  $u$  near coast is of the same order of magnitude as experiments with no along-shore variations in  $r_{ice}$ . Comparisons between the total transport across the ice edge between the experiments shown in Figure

2.12 show that this transport is also proportional to  $m$ ; for  $m = \pi/150 \text{ km}^{-1}$  ( $m = \pi/75 \text{ km}^{-1}$ ),  $T = 2.2412 (2.2422) \times 10^{10} \text{ m}^3$ . Further experiments show that as  $m$  increases  $T$  attains a constant value of  $2.2448 \times 10^{10} \text{ m}^3$ , which is less than the transport for  $r_{ice} = 2 \times 10^{-4} \text{ m s}^{-1}$  (where  $T = 2.2450 \times 10^{10} \text{ m}^3$ ). Recall that in the basic ATW-like case  $T = 2.2442 \times 10^{10} \text{ m}^3$  ( $T = 2.2474 \times 10^{10} \text{ m}^3$  when  $r_{ice} = 10^{-3} \text{ m s}^{-1}$ ).

There is also a time-varying response to steady winds when  $r_{ice}$  varies along-shore. However, the amplitude of the time-dependent along-shore sea level slope is two orders of magnitude less than the steady along-shore sea level slope ( $\sim 10^{-10}$  versus  $10^{-8}$ , Figure 2.12). This response has a period of  $\sim 3.5$  days and persists throughout the 10-day run.

### 2.3.7 Along-shore variations of ice width

Although the magnitude of along-shore changes in  $r_{ice}$  is unknown, along-shore variations in ice width occur on the Alaskan Beaufort shelf (Mahoney et al., 2007). The results of section 2.3.4 (Figure 2.10) suggest that if landfast ice width were to vary by 10 km over an along-shore distance of 100 km, along-shore flows of  $O(0.10 \text{ m s}^{-1})$  may result. Such differences in ice width are indeed observed.

Modeling along-shore changes in ice width proved difficult due to the introduction of  $2 \Delta x$  numerical noise at the ice edge and the problem was not resolved by neglecting the non-linear terms. An example of the sea level anomaly (m) and vertically-averaged along-shore velocity,  $u$  ( $\text{m s}^{-1}$ ) from a linearized experiment, in which ice width varies sinusoidally between 0 and 600 km along the coast, is shown in Figure 2.13.

Cross-shore velocities are not shown because noise at the ice edge obscures these signals. As in the case of a straight ice edge, there is a strong jet along the offshore edge of the ice. Although it is difficult to draw firm conclusions due to numerical noise, in aggregate, Figures 2.10 and 2.13 suggest that ice covers for which there are along-shore variations in width and/or bottom depth (at the ice edge), these along-shore differences should lead to an along-shore sea level slope sufficient to drive along-shore under-ice currents. The following results support this supposition.

We examined the case for an along-shore domain of 1200 km in which there is no ice for  $x < 700$  km (western portion of the domain) but a 20 km-wide landfast ice cover for  $x > 700$  km. Spatially uniform  $7 \text{ m s}^{-1}$  westward winds prevail wherever ice is absent. The under-ice response includes a large, slowly varying response and a smaller time-varying response. The mean response after 10 days of forcing (and with  $r_{ice} = r_b = 10^{-4} \text{ m s}^{-1}$ ) is shown in Figure 2.14. Upwelling develops along the western boundary of the landfast ice edge (marked by the dashed line at  $x = 700$  km) and sea level is a minimum at  $x = 700$  km,  $y = 0$  km (where  $\eta \sim -2$  m). The sea level distribution and velocities closely resemble the mound of water imposed at the western boundary of a landfast ice zone modeled in Chapter 1 of this thesis but because sea level is depressed at this location the under-ice along-shore transport is westward (and opposite to the case considered in Chapter 1). In addition to the along-shore sea level slope induced by the westward winds for  $x < 700$  km, there is a cross-shore sea level slope between the coast and the northern ice edge (at  $y = 20$  km). This slope is positive with sea level lower at the coast than at the ice edge. While the cross-shore sea level slope is a maximum at the ice edge and

minimum at the coast, it is always smaller than the along-shore sea level slope. For example, at  $x = 1000$  km,  $\Delta\eta/\Delta y = 4.25 \times 10^{-7}$  and  $\Delta\eta/\Delta x = 5.46 \times 10^{-7}$ .

The vertically-averaged along-shore velocity,  $u$ , (Figure 2.14B) decays rapidly to the east beneath the ice and along the northern boundary of the ice edge. Near the coast  $u$  at  $x = 700$  km is westward at  $\sim -1$  m s<sup>-1</sup> west of the ice edge, but at  $x = 800$  km (beneath the landfast ice)  $u$  is  $< 0.10$  m s<sup>-1</sup>. For constant  $r_{ice}$ , we found that  $u$  decreased to  $\sim 10\%$  of its value within  $\sim 100$  km of the western boundary, which is similar to the decay scale in Figure 2.14B (Chapter 1 of this thesis). Figure 2.14C shows that the under-ice vertically-averaged cross-shore velocity,  $v$ , is onshore everywhere. This is consistent with the generation of onshore boundary layer transport in both the under-ice and bottom boundary layers by the westward along-shore transport.

Overall, the effects of westward winds blowing parallel and transverse to this idealized landfast ice distribution establishes a sea level distribution that forces a westward under-ice flow over distances comparable to the  $\sim 500$  km length of the ABS (e.g., at  $x=1200$  km,  $u$  is  $\sim 0.007$  m s<sup>-1</sup>) and leads to a substantial sea level decrease far from the ice edge boundary that is transverse to the wind (e.g.,  $\eta \sim -1.8$  m at  $x = 1200$  km).

This ice distribution also includes a transitory response, which propagates under the ice as coastally trapped vorticity waves (Figure 2.15). The waves are generated by the abrupt surface stress curl at the western boundary of the landfast ice cover, similar to topographic waves generated at the edge of a storm (e.g. McCreary and Chao, 1985). The flow at the western boundary of the landfast ice adjusts by radiating waves eastward from

this discontinuity. The wave period, phase speed, and wavelength are  $\sim 3.5$  days,  $\sim 2.1$  m  $s^{-1}$  and  $\sim 635$  km, respectively. At the coast, the wave-associated sea level slopes are initially  $\sim 10^{-7}$  and velocity fluctuations are  $0.05$  m  $s^{-1}$ . The e-folding decay time scale for the waves is  $\sim 3.5$  days and so on the same order as the wave period.

## ***2.4 Discussion and conclusion***

Our model results suggest that a spatially-uniform upwelling-favorable wind blowing parallel to the edge of a landfast ice sheet of constant width over a linearly sloping bottom will force a coastal sea level set-down and a cross-shore sea level slope. Beneath the landfast ice, this slope drives an upwind geostrophic along-shore flow, which in turn forces offshore transport in both the surface and bottom boundary layers. Partial observational support for this result comes from Weingartner et al.'s (2009) measurements from the ABS shelf. In early winter, as the landfast ice sheet formed, they observed a strong ( $\sim 0.5$  to  $1$  m  $s^{-1}$ ) downwind, alongshore flow at the ice edge, but a weak ( $\ll 0.05$  m  $s^{-1}$ ) upwind flow beneath the landfast ice and within a few kilometers of this ice edge. In agreement with the model results, the observed under-ice along-shore velocity profile was parabolic (although they were unable to measure flow in the boundary layers). However, as winter progressed and the landfast ice edge expanded seaward, the wind- under-ice current relationship collapsed so that, in general, they found no significant correlation between offshore winds and under-ice currents. Our model results suggest several mechanisms that might lead to the dissolution of this relationship, including along-shore variations in under-ice friction and/or landfast ice width. Both



mechanisms can induce along-shore sea level slopes and under-ice currents that vary over spatial scales smaller than the length scale of the wind-forcing. Consistent with this suggestion, Weingartner et al. (2009) found that the along-shore de-correlation length scale of sub-inertial, under-ice, along-shore currents is  $< 200$  km as opposed to the  $> 300$  km de-correlation scale in ice-free conditions.

Other mechanisms, not included in our simple models, may also lead to the absence of a wind-under-ice current correlation. These include deep ice keels that block (Macdonald and Carmack, 1991) or channel the under-ice flow and/or variations in ice thickness that influence the water depth (and thus vortex stretching). Moreover, we have treated the landfast ice edge as an abrupt boundary, offshore of which the flow is driven by a uniform surface wind-stress. In fact, 3-day repeat satellite image analyses of ice motion by Morris et al. (1999) from the East Siberian Sea suggest there is a transition zone between the landfast and freely drifting ice, in which internal ice stresses are important, thereby reducing the efficacy of momentum transfer between the atmosphere and ocean. The presence of a transition zone would also alter the spatial variability in the under-ice friction coefficient and the effective ice width.

Weingartner et al. (2009) also reported near-coastal sea level fluctuations beneath the ABS landfast ice of 0.5 m or more during winter. Our models suggest that changes in sea-level develop due to cross-shore transports within the surface and bottom boundary layers. In the case of uniform along-shore conditions, these boundary-layer transports are not compensated for by a cross-shore interior flow. Consequently, circulation beneath the landfast ice can never attain steady state under such conditions. Hence, relatively large

fluctuations in sea level may occur. By weakening the tensile strength of the ice, large sea level fluctuations may contribute to landfast ice “breakout events”, in which portions of the landfast ice detach from shore and subsequently begin drifting (C. George and H. Eicken, *pers. comm.*). Such events would result in changes in the surface stress distribution and, by exposing nearshore waters to the atmosphere, promote ice and dense water formation. Breakout events also pose a risk to Arctic coastal residents who depend on landfast ice as a stable hunting platform (e.g. George et al., 2004).

Finally, Weingartner et al. (2009) observed sea level fluctuations that propagated eastward with a period of  $\sim 4$  days, a phase speed of  $\sim 1 \text{ m s}^{-1}$  and a wavelength of  $\sim 900$  km. The current fluctuations associated with these propagating features are  $\sim 0.03 \text{ m s}^{-1}$ . While these transitory disturbances may be associated with slope processes (Aagaard and Roach, 1990; R. Pickart *pers. comm.*), they may also be initiated by winds blowing transverse to the lateral boundary of the landfast ice zone (as discussed in section 2.3.7). The landfast ice distribution at the western boundary of the ABS is consistent with this response. Here the landfast ice terminates abruptly at the juncture of the ABS and the Chukchi Sea shelf which is covered seasonally by a broad expanse of drifting ice.

The idealized modeling approach adopted here explored how circulation in the landfast ice zone may evolve in response to wind forcing. We invoked simple (and perhaps naïve) ideas on variations in ice-ocean frictional coupling and ice width within the landfast ice zone - an approach necessitated by the dearth of guiding observations of these important features of the Arctic Ocean’s shelf seas. The results suggest that temporal and spatial gradients in these parameters translate into cross- and along-shore

pressure gradients that drive the under-ice circulation, which can be uncorrelated with the offshore wind field. These ice parameters change seasonally and synoptically due to landfast ice expansion (or reduction due to breakouts) and deformation processes within and along the edge of the landfast ice zone. The models and observations imply that landfast ice dynamics, which were not explicitly included herein, may effectively convert the long-wavelength forcing of the wind into shorter-scale ocean motions in the landfast ice zone.

## 2.5 Appendix

We begin with the time-dependent vertically-averaged momentum equations (e.g. Kundu and Cohen, 2008).

$$\begin{aligned}
 \frac{\partial u}{\partial t} - fv &= -g \frac{\partial \eta}{\partial x} - B_x - S_x + F \\
 \frac{\partial v}{\partial t} + fu &= -g \frac{\partial \eta}{\partial y} - B_y - S_y \\
 \frac{\partial(uh)}{\partial x} + \frac{\partial(vh)}{\partial y} &= -\frac{\partial \eta}{\partial t}
 \end{aligned}
 \tag{A.2.1}$$

where  $u$  and  $v$  are the along- and cross-shore velocities ( $\text{m s}^{-1}$ ), respectively,  $g$  is the acceleration due to gravity ( $\text{m s}^{-2}$ ),  $\eta$  is the sea level anomaly (m),  $h$  is the depth ( $h = sy$ , m),  $B$  and  $S$  are the surface and bottom stresses due to bottom and under-ice friction, respectively, and  $F$  is the wind stress. Note  $B$  and  $S$  both have the same sign.

Assuming that  $B$  and  $S$  are proportional to the under-ice transport, we have

$$\begin{aligned}
\frac{\partial u}{\partial t} - fv &= -g \frac{\partial \eta}{\partial x} - \frac{(r_{ice} + r_b)u}{h} + F \\
\frac{\partial v}{\partial t} + fu &= -g \frac{\partial \eta}{\partial y} - \frac{(r_{ice} + r_b)v}{h} \\
\frac{\partial(uh)}{\partial x} + \frac{\partial(vh)}{\partial y} &= -\frac{\partial \eta}{\partial t}
\end{aligned} \tag{A.2.2}$$

where  $r_{ice}$  ( $\text{m s}^{-1}$ ) is the linear under-ice friction coefficient,  $r_{ice} = r_{ice}(x,y)$ , and  $r_b$  ( $\text{m s}^{-1}$ ) is the linear bottom friction coefficient. Taking the curl of the momentum equations (noting that  $F$  is zero everywhere under the ice) leads to a time-dependent, under-ice vorticity equation:

$$\begin{aligned}
\frac{\partial \eta}{\partial x} &= \underbrace{\frac{\partial}{\partial t} \left[ \frac{h}{sf} \left( \frac{\partial^2 \eta}{\partial y^2} + \frac{\partial^2 \eta}{\partial x^2} \right) - \frac{f}{sg} \eta \right]}_{\text{Time variation in relative vorticity and stretching}} + \underbrace{\frac{1}{sf} \left( \frac{\partial(r_{ice} + r_b)}{\partial y} \frac{\partial \eta}{\partial y} + \frac{\partial(r_{ice} + r_b)}{\partial x} \frac{\partial \eta}{\partial x} \right)}_{\text{Advective-like vorticity term}} \\
&+ \underbrace{\frac{(r_{ice} + r_b)}{sf} \left( \frac{\partial^2 \eta}{\partial y^2} + \frac{\partial^2 \eta}{\partial x^2} \right)}_{\text{Diffusive-like vorticity term}} - \underbrace{\frac{(r_{ice} + r_b)}{fh} \frac{\partial \eta}{\partial y}}_{\text{Cross-shore Stress term}}
\end{aligned} \tag{A.2.3}$$

Along-shore sea level slope

In the absence of along-shore changes in ice or winds (and neglecting the time variation of vorticity stretching), A.2.3 reduces to:

$$\frac{f}{sg} \frac{\partial \eta}{\partial t} = \underbrace{\frac{1}{sf} \frac{\partial}{\partial y} \left[ (r_{ice} + r_b) \frac{\partial \eta}{\partial y} \right]}_{\text{Diffusive- and advective-like vorticity terms i.e. vorticity terms 1 and 2}} - \underbrace{\frac{(r_{ice} + r_b)}{fh} \frac{\partial \eta}{\partial y}}_{\text{Vorticity term 3}} \tag{A.2.4}$$

Time variation of sea level

A comparison of A.2.4 with A.2.3 shows that the cross-shore stress terms contribute to the vorticity balance through both the advective- and diffusive-like vorticity terms and vorticity term 3. However, in the absence of along-shore variations in  $r_{ice}$ , the cross-shore stress only contributes to the vorticity balance via term 3:  $(r_{ice} + r_b) / fh (\partial \eta / \partial y)$ . Thus in

the text (section 2.3.5), where we consider the vorticity balance for the case of no along-shore variations in ice, it is only necessary to consider a single extra vorticity term, term 3. This cross-shore stress term is inversely proportional to bottom depth and is important in the numerical results, since it partially determines the balance between the sea level slope and cross-shore transport. This term is absent in the analytical example discussed in section 2.2.

If instead we neglect the cross-shore stress terms as small (in eq. A.2.2) and assume  $\partial v / \partial t$  is negligible, the cross-shore momentum equation reduces to geostrophy and the time-dependent vorticity equation reduces to a time-dependent version of the ALW vorticity equation

$$\frac{\partial}{\partial t} \left[ \frac{f}{sg} \eta - \frac{1}{sf} \frac{\partial}{\partial y} \left( h \frac{\partial \eta}{\partial y} \right) \right] + \frac{\partial \eta}{\partial x} = \frac{1}{sf} \frac{\partial}{\partial y} \left( (r_{ice} + r_b) \frac{\partial \eta}{\partial y} \right) \quad \text{A.2.5}$$

A.2.5 can be further simplified by neglecting the time variation of vorticity stretching as small compared to the other terms (numerical results confirm this assumption) so that we have

$$\frac{f}{sg} \frac{\partial \eta}{\partial t} + \frac{\partial \eta}{\partial x} = \frac{1}{sf} \frac{\partial}{\partial y} \left[ (r_{ice} + r_b) \frac{\partial \eta}{\partial y} \right] \quad \text{A.2.6}$$

Equation A.2.6 is the time-dependent version of the ALW vorticity equation: at steady state, equation A.2.6 reduces to the ALW vorticity equation, eq. 2.2, given in the text.

A further useful diagnostic equation can be derived from the steady state form of A.2.2. Taking the curl of the steady state governing equations leads to:

$$\begin{aligned}
 \frac{\partial \eta}{\partial x} &= \frac{\left( (r_b v)_x - (r_b u)_y \right)}{g_s} + \frac{\left( (r_{ice} v)_x - (r_{ice} u)_y \right)}{g_s} - \frac{\left( (F_y)_x - (F_x)_y \right)}{g_s} \\
 \text{Along-Shore} & \quad \underbrace{\hspace{10em}} & \underbrace{\hspace{10em}} & \underbrace{\hspace{10em}} \\
 \text{Sea Level} & \quad \frac{\text{Bottom Stress Curl}}{\text{Bottom Slope}} & \quad \frac{\text{Surface Stress Curl}}{\text{Bottom Slope}} & \quad \frac{\text{Wind Stress Curl}}{\text{Bottom Slope}} \\
 \text{Slope} & & & 
 \end{aligned}
 \tag{A.2.7}$$

which shows that the along-shore sea level slope is balanced by the stress curls divided by the bottom slope. This is text equation 2.7.

## 2.6 References

- Aagaard, K., Roach, A.T., 1990. Arctic ocean-shelf exchange: Measurements in Barrow Canyon. *Journal of Geophysical Research* 95 (C10), 18163-18175.
- Arakawa, A., Lamb, V.R., 1977. *Methods of Computational Physics*. Academic Press.
- Clarke, A.J., 1978. On wind-driven quasi-geostrophic water movements at fast ice edges. *Deep Sea Research* 25 (1), 41-47.
- Csanady, G.T., 1978. The arrested topographic wave. *Journal of Physical Oceanography* 8 (1), 47-62.
- Csanady, G.T., 1981. Shelf circulation cells. *Philosophical Transactions of the Royal Society of London Series a-Mathematical Physical and Engineering Sciences* 302 (1472), 515-530.
- Fennel, W., Johannessen, O.M., 1998. Wind forced oceanic responses near ice edges revisited. *Journal of Marine Systems* 14 (1-2), 57-79.
- Gammelsrod, T., Mork, M., Roed, L.P., 1975. Upwelling possibilities at an ice edge: A homogeneous model. *Marine Science Communications* 1 (2), 115-145.
- George, J.C., Huntington, H.P., Brewster, K., Eicken, H., Norton, D.W., Glenn, R., 2004. Observations on shorefast ice dynamics in Arctic Alaska and the responses of the Iñupiat hunting community. *Arctic* 57 (4), 363-374.
- Gill, A.E., Schumann, E.H., 1974. The generation of long shelf waves by the wind. *Journal of Physical Oceanography* 4 (1), 83-90.
- Kundu, P.K., Cohen, I.M., 2008. *Fluid Mechanics*, 4th ed. Academic Press, Amsterdam; Boston.

- Macdonald, R.W., Carmack, E.C., 1991. The role of large-scale under-ice topography in separating estuary and ocean on an Arctic shelf. *Atmosphere-Ocean* 29 (1), 37-53.
- Mahoney, A., Eicken, H., Shapiro, L., 2007. How fast is landfast sea ice? A study of the attachment and detachment of nearshore ice at Barrow, Alaska. *Cold Regions Science and Technology* 47 (3), 233-255.
- McCreary, J.P., Chao, S.-Y., 1985. Three-dimensional shelf circulation along an eastern ocean boundary. *Journal of Marine Research* 43 (1), 13-36.
- McPhee, M.G., 1990. Small scale processes, in: Smith, W.C. (Ed.), *Polar Oceanography Part A Physical Science*. Academic Press, New York, pp. 287-334.
- Mellor, G.L., Yamada, T., 1982. Development of a turbulence closure model for geophysical fluid problems. *Reviews of Geophysics* 20 (4), 851-875.
- Morris, K., Li, S., Jefferies, M., 1999. Meso- and microscale sea-ice motion in the East Siberian Sea as determined from ERS-1 SAR data. *Journal of Glaciology* 45 (15), 370-383.
- Pickart, R.S., Moore, G.W.K., Torres, D.J., Fratantoni, P.S., Goldsmith, R.A., Yang, J., 2009. Upwelling on the continental slope of the Alaskan Beaufort Sea: Storms, ice, and oceanographic response. *Journal of Geophysical Research* 114 (C1), C00A13.
- Shchepetkin, A.F., McWilliams, J.C., 2005. The regional oceanic modeling system (ROMS): a split-explicit, free-surface, topography-following-coordinate oceanic model. *Ocean Modelling* 9 (4), 347-404.



- Shirasawa, K., 1986. Water stress and ocean current measurements under first-year sea ice in the Canadian Arctic. *Journal of Geophysical Research* 91 (C12), 14305-14316.
- Song, Y., Haidvogel, D., 1994. A semi-implicit ocean circulation model using a generalized topography-following coordinate system. *Journal of Computational Physics* 115 (1), 228-244.
- Song, Y.T., Wright, D.G., 1998. A general pressure gradient formulation for ocean models. Part II: Energy, momentum, and bottom torque consistency. *Monthly Weather Review* 126 (12), 3231-3247.
- Tucker, W.B., III, Weeks, W.F., Frank, M., 1979. Sea ice ridging over the Alaskan continental shelf. *Journal of Geophysical Research* 84 (C8), 4885-4897.
- Weingartner, T.J., Danielson, S.L., Kasper, J.L., Okkonen, S.R., 2009. Circulation and water property variations in the nearshore Alaskan Beaufort Sea (1999-2007). US Dept. of Interior, Minerals Management Service, Alaska Outer Continental Shelf Region, Anchorage, Alaska, p. 154.

## 2.7 Figures

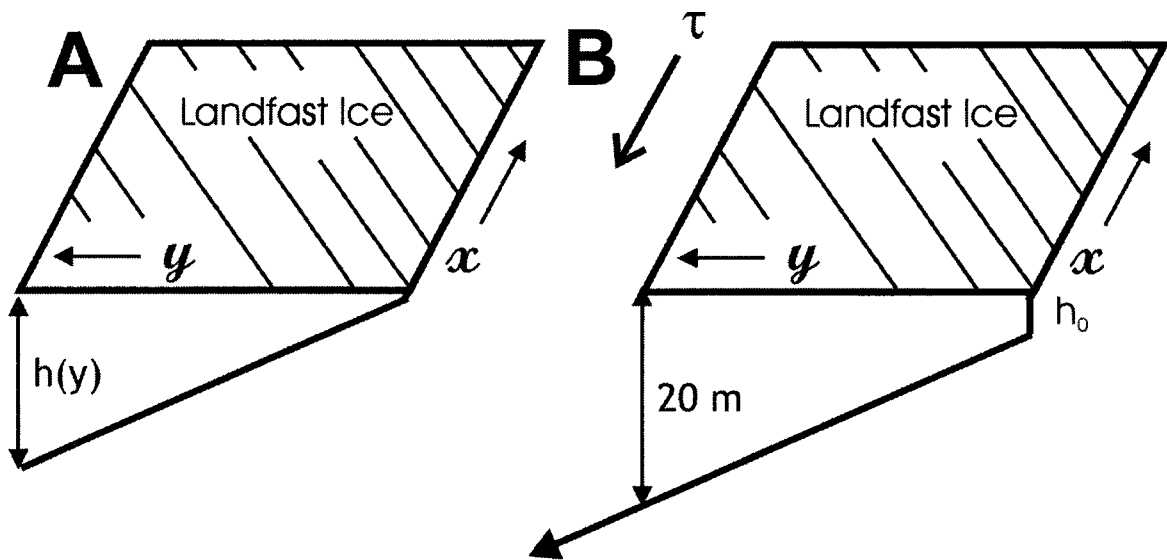


Figure 2.1. Coordinate systems. (A) The coordinate system for the analytic model, with the coast along  $y = 0$  and depth increasing linearly with distance offshore,  $h = sy$ . (B) The numerical model domain where  $h = h_0 + sy$  ( $h_0$  is the depth of the coastal wall). The bottom slope,  $s = 7.5 \times 10^{-4}$ , identical in both the analytical and numerical models, is comparable to the Alaskan Beaufort Sea shelf bottom slope. Whereas the analytical domain encompasses just the area under the landfast ice, the numerical domain includes the area offshore of the ice edge where a spatially uniform upwelling ( $0.1 \text{ N m}^{-2} \sim 7 \text{ m s}^{-1}$ ) wind blows parallel to the coast.

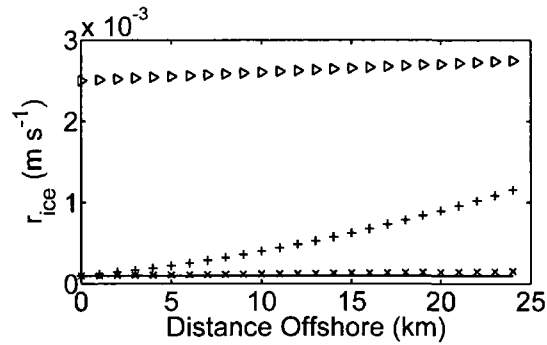


Figure 2.2. The ice-ocean friction coefficient,  $r_{ice} = C_1 (C_2 + C_3 y)^2$ . Crosses mark the basic case ( $C_1 = 10^{-2}$ ,  $C_2 = 10^{-1}$ ,  $C_3 = 10^{-6}$ ). Plus signs are for  $C_1 = 10^{-2}$ ,  $C_2 = 10^{-1}$ ,  $C_3 = 10^{-5}$ . Triangles mark the case with  $C_1 = 10^{-2}$ ,  $C_2 = 5 \times 10^{-1}$ ,  $C_3 = 10^{-6}$ . The solid line is the constant under-ice friction coefficient ( $r_{ice} = 10^{-4}$ ). The range of  $r_{ice}$  of  $10^{-4}$  and  $10^{-3}$  was investigated using numerical simulations.

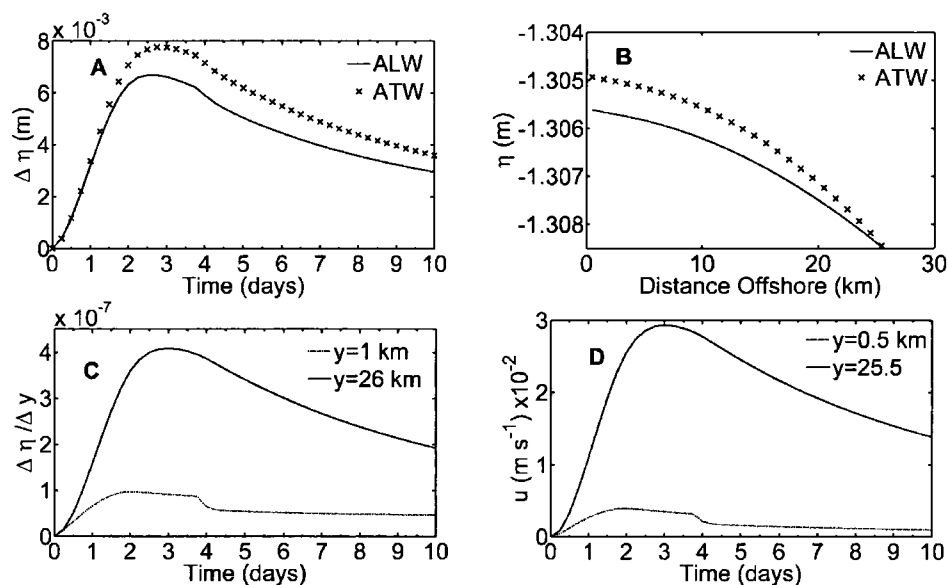


Figure 2.3. Numerical results. (A) Sea level difference between the coast and the ice edge for the basic ALW- and ATW-like simulations versus time. (B) The sea level between the coast and the ice edge after ten days for the basic ALW- and ATW-like simulations. (C) The cross-shore sea level slope near the coast ( $y = 1$  km) and near the ice edge ( $y = 26$  km) versus time from the basic ALW-like simulation. (D) The along-shore velocity,  $u$ , near the coast and the ice edge from the basic ALW-like simulation. Note the  $y$ -location of  $\Delta \eta / \Delta y$  and  $u$  differ because of the staggered grid.

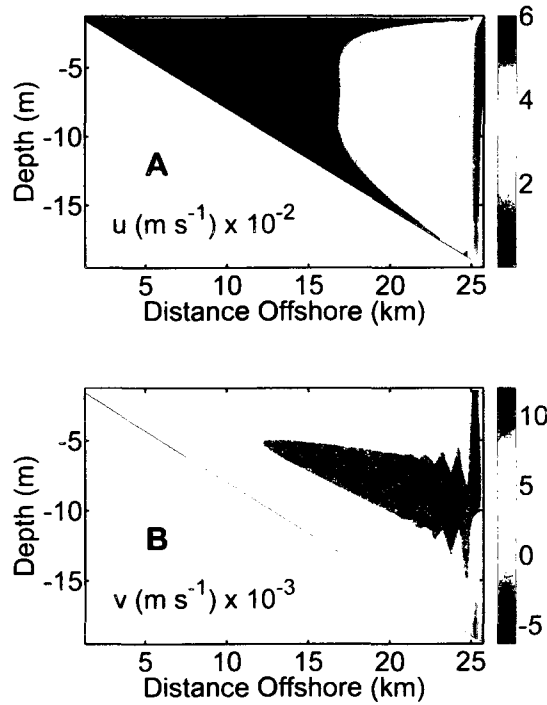


Figure 2.4. Under-ice velocities. The cross-shelf distribution after 10 days of (A) along-shore velocity ( $\text{m s}^{-1}$ ) inshore of the ice edge (positive velocities imply flow out of the page) and (B) cross-shore velocity ( $\text{m s}^{-1}$ , positive velocities indicate offshore flow).

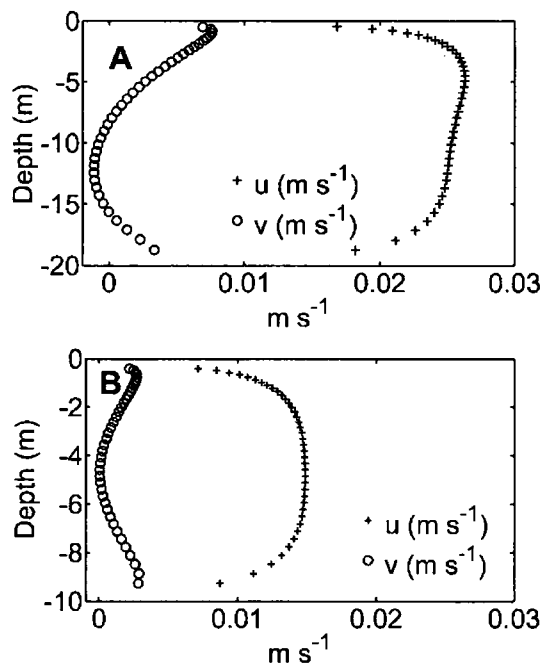


Figure 2.5. The under-ice boundary layer. Vertical profiles of the horizontal velocity components ( $\text{m s}^{-1}$ ) beneath the landfast ice cover after 10 days of upwelling-favorable wind stress. (A) over the 19 m isobath, (B) over the 10 m isobath. Note that the y-axes differ between A and B.

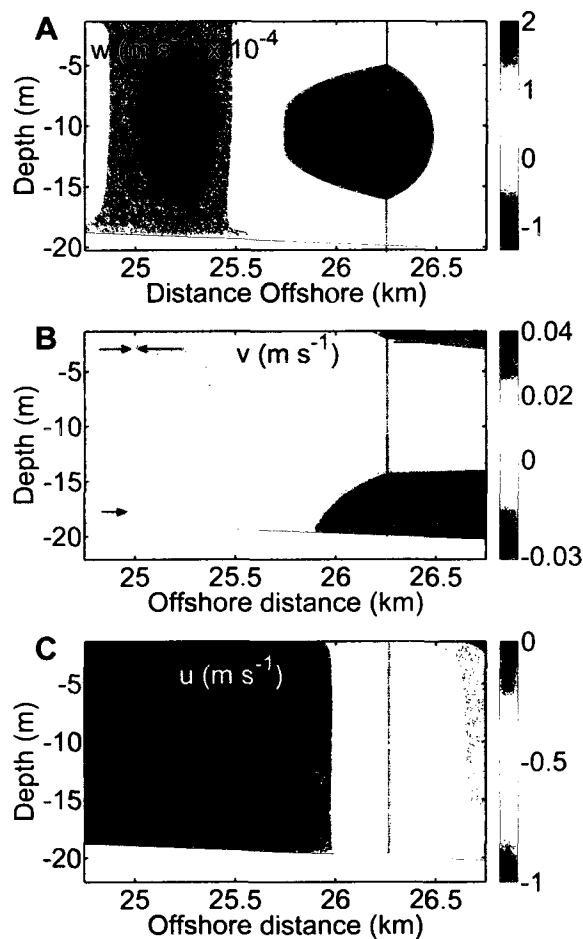


Figure 2.6. Currents near the ice edge. The cross-shelf distribution in the vicinity of the ice edge after 10 days for the basic 3-D experiment of the: (A) vertical velocity,  $w$ , (positive velocities are up), (B) cross-shore velocity,  $v$ , and (C) along-shore velocity,  $u$ . The vertical line indicates the grid point where the wind stress is applied (26.25 km from the coast). Arrows schematically represent the direction of flow in panel B and are not to scale. Not visible because of the contouring,  $u$  increases at  $x = 24.75$  km from  $0.02 \text{ m s}^{-1}$  to  $\sim 0.05 \text{ m s}^{-1}$  at  $x = 25.75$  km.

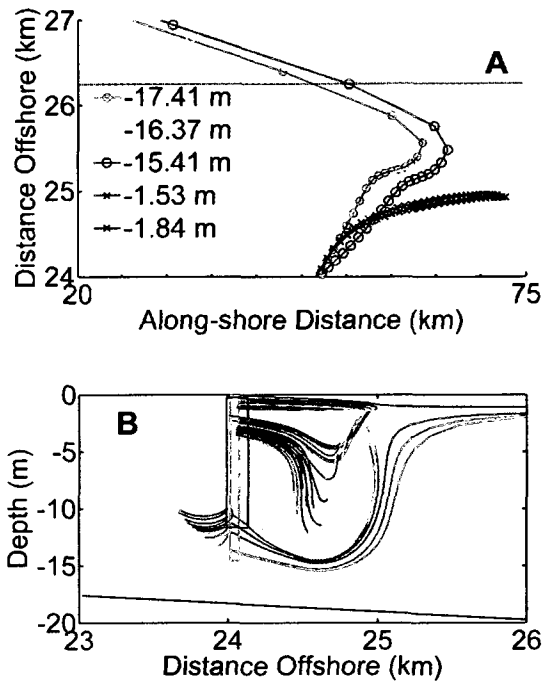


Figure 2.7. Particle trajectories. Particle trajectories (A) in the  $x$ - $y$  plane and (B) in the  $y$ - $z$  plane. In panel A, particles that cross the ice edge are denoted by circles and those that remain inshore of the ice edge are indicated by crosses. In panel A, the ice-edge is marked by the horizontal line at  $y = 26.25$  km, the release depth of the particles is indicated in the legend, and markers are spaced 0.25 days apart. In panel B, the particles were released within the small grey box  $\sim 24$  km from the coast. Particles released within the black rectangle do not transit the ice edge during the 10 day time period considered. The bottom is indicated by the sloping solid line in panel B.



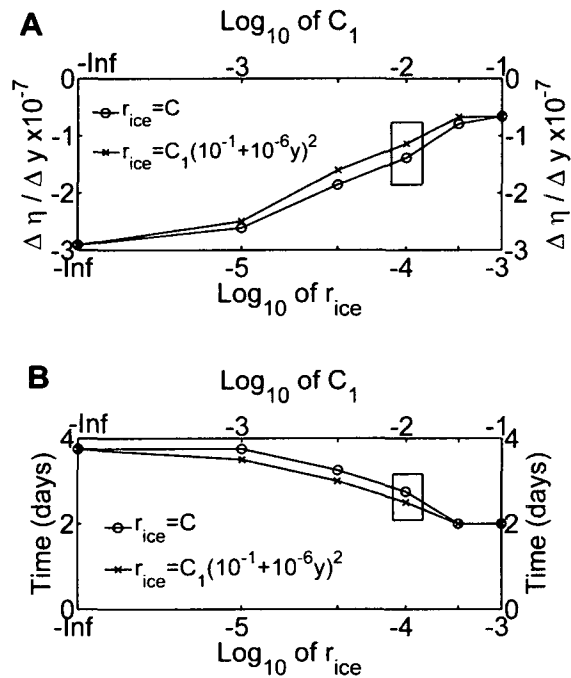


Figure 2.8. Cross-shore sea level slope and frictional adjustment time versus the magnitude of the ice-ocean friction coefficient. (A) The black circles denote the cross-shore sea level slope versus the  $\log_{10}$  of the under-ice friction coefficient (for  $r_{ice} = \text{constant}$ ). The blue crosses denote the cross-shore sea level slope versus the  $\log_{10}$  of  $C_1$  (for  $r_{ice} = \text{variable}$ ) after 10 days. (B) The black circles denote the frictional adjustment time ( $t_f$ ) versus the  $\log_{10}$  of the under-ice friction coefficient (for  $r_{ice} = \text{constant}$ ). The blue crosses denote  $t_f$  versus the  $\log_{10}$  of  $C_1$  (for  $r_{ice} = \text{variable}$ ). The basic numerical ALW and ATW-like experiments are enclosed in the rectangles.

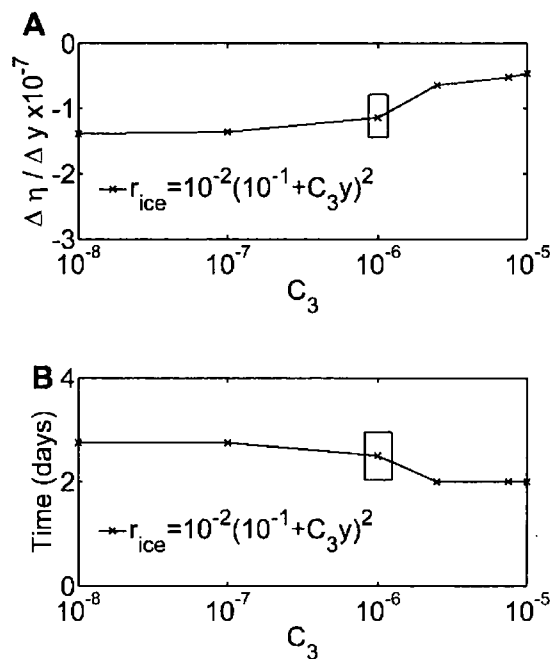


Figure 2.9. Cross-shore sea level slope and frictional adjustment time as functions of cross-shore variability in the ice-ocean friction coefficient. The effect of cross-shore variability of  $r_{ice}$  on (A) cross-shore sea level slope and (B) on  $t_f$ . Results are from 10 days. The basic numerical-ALW result is indicated by the rectangle.

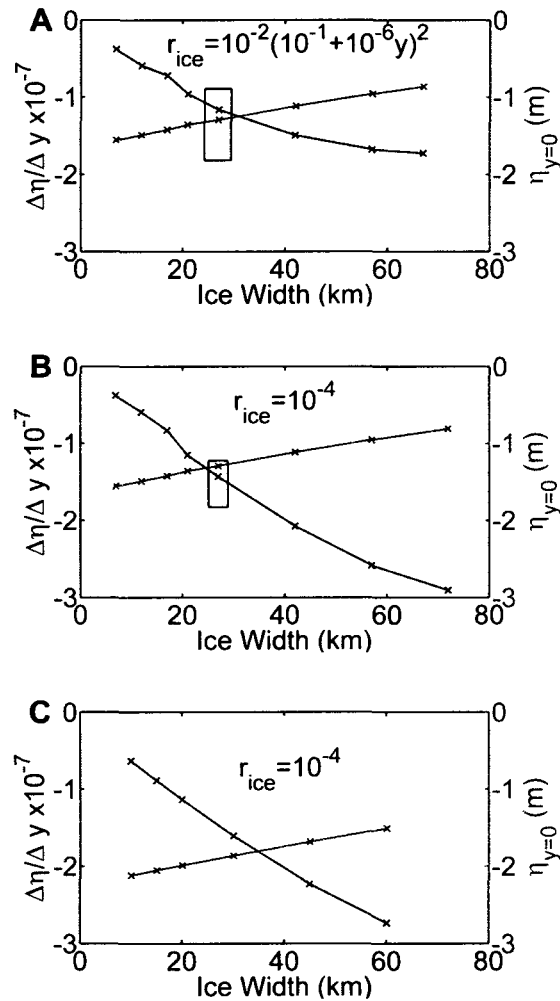


Figure 2.10. Effect of ice width on the cross-shore sea level slope. The cross-shore sea level slope versus ice width (blue) and coastal sea level versus landfast ice width (green) for: (A)  $r_{ice}$  = variable and (B)  $r_{ice}$  = constant. The basic model with  $L = 25$  km is indicated by boxed values. (C) The cross-shore sea level slope (blue) and sea level at the coast (green) versus ice width for a flat bottom ocean and  $r_{ice}$  = constant.

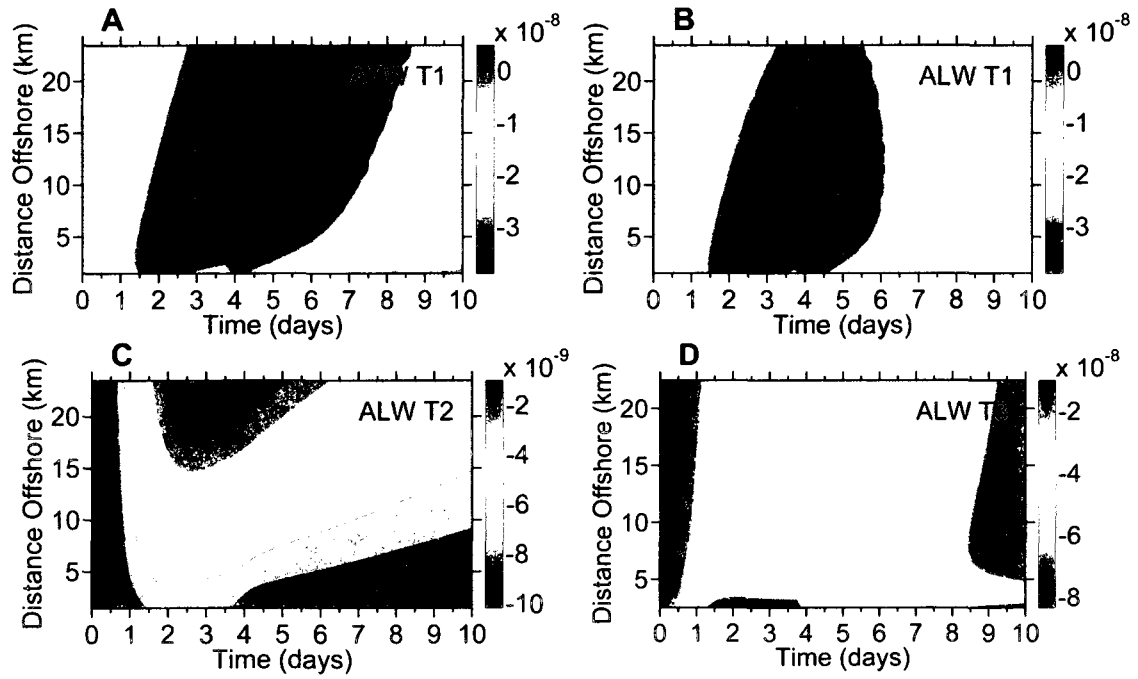


Figure 2.11. The under-ice vorticity terms. (A) The diffusive-like ATW vorticity term for  $r_{ice} = 10^{-4}$ . Panels B-D are from the basic ALW-like numerical simulation and are the: (B) diffusive-like vorticity term (term 1), (C) advective-like vorticity term (term 2), and (D) cross-shore stress vorticity term, (term 3). Terms 1 through 3 refer to the expressions in text equation 2.6.

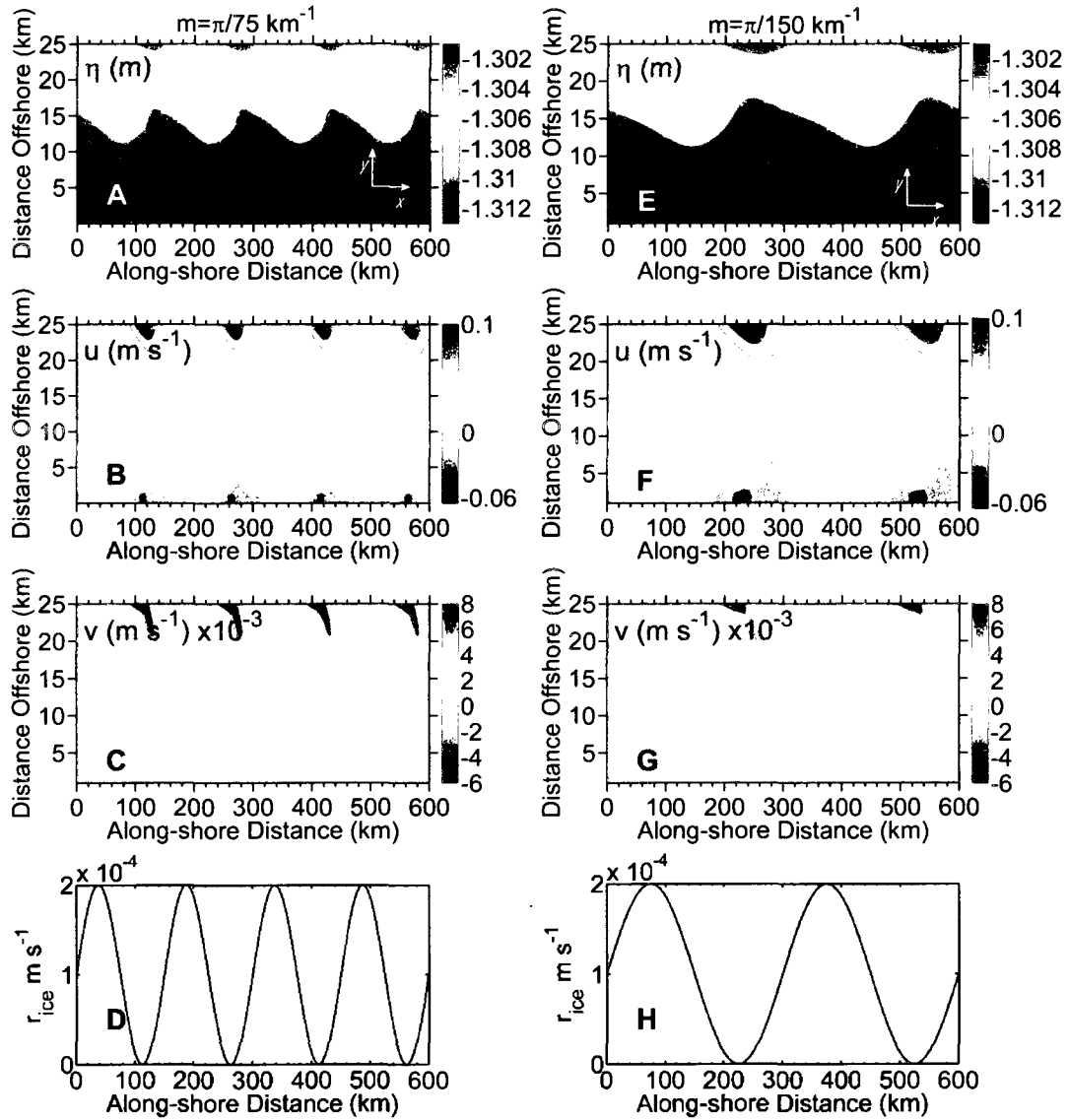


Figure 2.12. The effect of along-shore variations in  $r_{ice}$  on under-ice circulation. The along- and cross-shore distributions of: (A) sea level anomaly, (B) vertically averaged  $u$  (positive velocities eastward), (C) vertically averaged  $v$  (positive velocities northward). Panel (D) shows the along-shore distribution of  $r_{ice}$  for  $r_{ice} = [10^{-2} + 10^{-2} \sin(mx)]10^{-2}$  with  $m = \pi/75 \text{ km}^{-1}$ . Companion plots to panels A-D, panels E- H are for  $m = \pi/150 \text{ km}^{-1}$ .

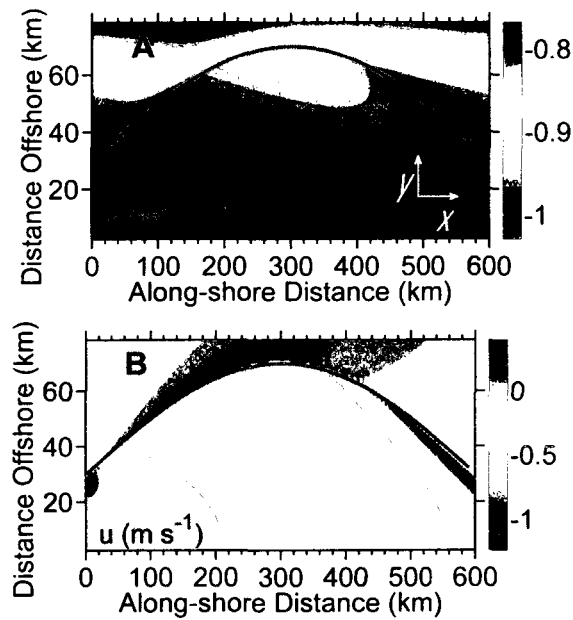


Figure 2.13. The effect of along-shore variations in the ice width on under-ice circulation. (A) Sea level anomaly from a linearized experiment with ice width increasing with along-shore distance. (B) Vertically averaged along-shore velocity. The ice edge is marked by the dashed line with ice covering the area inshore of the ice edge. A spatially uniform  $7 \text{ m s}^{-1}$  upwelling wind is applied everywhere there is no ice.

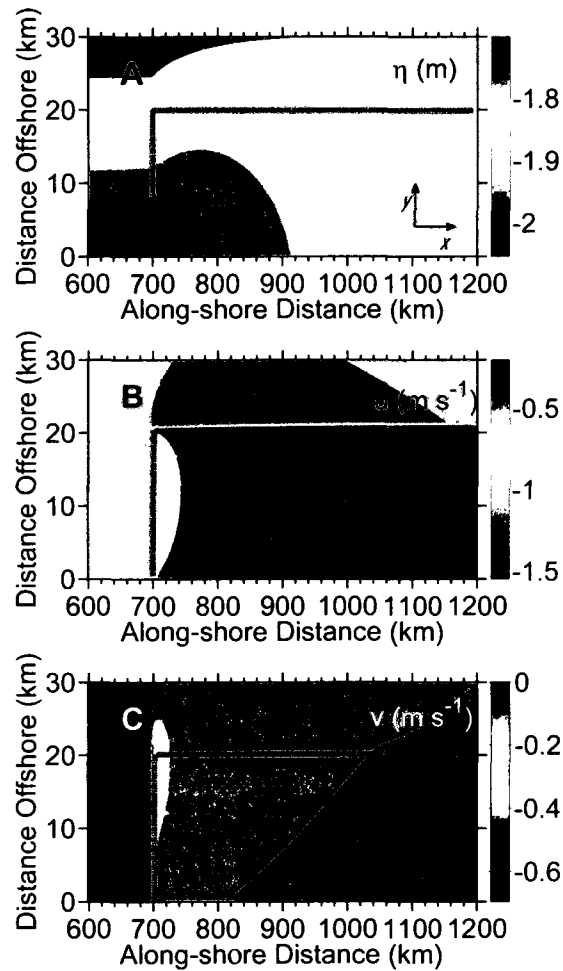


Figure 2.14. The effect of along-shore changes in ice coverage on under-ice circulation. The response after 10 days to a  $7 \text{ m s}^{-1}$  upwelling (westward) wind stress blowing parallel to the ice edge at  $y \geq 20 \text{ km}$  and  $x > 700 \text{ km}$  and transverse to the landfast ice edge at  $x < 700 \text{ km}$ . The ice edge is marked by the dashed line. (A) Sea level anomaly, (B) vertically averaged  $u$ , and (C) vertically averaged  $v$ .

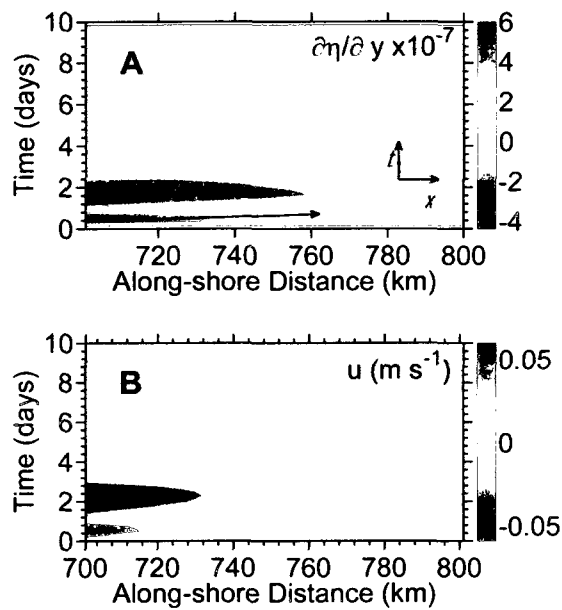


Figure 2.15. An under-ice vorticity wave. (A) The along-shore sea level slope at the coast as a function of along-shore distance and time and (B) the associated along-shore velocity variations. The black line in A indicates the progression of the crest of the wave along the coast with time.



## 2.8 Tables

Table 2.1. Range of ice parameters considered.

	$C_1$	$C_2$	$C_3$	$m=2\pi/M$ (M, km)	Ice Width ( $L$ , km)
Base (Analytic)	$2 \cdot 10^{-2}$	$10^{-1}$	$10^{-6}$	NA	25
Numerical	$10^{-3}-10^{-1}$	$10^{-3}-10^{-1}$	$10^{-5}-0$	M=200-1200	10-75
Range of $r_{ice}$ considered	$0 - 10^{-3} \text{ m s}^{-1}$				

## **Chapter 3 The spreading of a buoyant plume beneath a landfast ice cover<sup>1</sup>**

### ***Abstract***

To demonstrate the effect of an immobile landfast ice cover on buoyant discharge idealized numerical simulations were conducted with the Regional Ocean Modeling System. The model is configured to resemble the seasonally frozen Colville River, which flows onto the Alaskan Beaufort Shelf. For comparison, simulations were conducted both with and without an ice cover; without an ice cover, the intense stratification typical of Arctic shelf seas means a “surface advected plume” forms and the downstream coastal current is slim. When a finite width ice cover is applied, a surface plume forms and the change in stress across the ice edge leads to convergence at the ice edge, which inhibits cross-shore movement of the plume in the far field coastal current domain. When ice covers the entire domain, the river influence extends  $> 45$  km ( $> 9$  times the local Baroclinic Rossby Radius of 5 km) offshore of the mouth of the inlet and the downstream coastal current is very wide  $\sim 35$  km.

### ***3.1 Introduction***

The massive river discharges entering the Arctic Ocean play important roles in stratifying this basin and in the global hydrologic balance (Aagaard and Carmack, 1989). The vast, shallow, and seasonally ice-covered circumpolar continental shelves act as the Arctic

---

<sup>1</sup> Kasper, J.L., Weingartner, T.J., Chapter 3 The spreading of a buoyant plume beneath a landfast ice cover, prepared for submission to Continental Shelf Research.

Ocean's estuaries (Macdonald and Carmack, 1991; Eicken et al., 2005) and thus control the disposition of the discharge and its dissolved and suspended loads. Much of our understanding of the fate of runoff into the ocean derives from studies on mid-latitude continental shelves. Much of this should be transferable to arctic shelves except during winter and early summer when shelf sea ice, and particularly the immobile landfast ice that covers the inner shelf, interacts both dynamically and thermodynamically with the buoyant plumes generated by river discharges. For example, such plumes affect melting patterns, alter ice albedo (Searcy et al., 1996), and can be channeled or blocked by under-ice topography (Macdonald et al., 1987; Macdonald and Carmack, 1991). We expect that the spreading plume is frictionally coupled to the underside of the ice and that this affects the behavior of the plume as it moves over the shelf. If the coupling is sufficiently strong then the anti-cyclonic bulge near the river mouth may not follow the scales Yankovsky and Chapman (1997, hereafter YC97) derived for ice-free conditions. Herein, we neglect many of these complexities and only consider how the presence of a uniformly thick, immobile landfast ice sheet, frictionally-coupled to the ocean, affects the spreading of an under-ice buoyant plume. This study, while heuristic (and perhaps naïve), allows simple comparisons between the buoyant plumes of arctic shelves with their better-understood mid-latitude counterparts. Our results may also provide some information on the expected cross-shelf and temporal scales of motion of the plumes. There are only a few observations of under-ice plumes from the Alaskan Beaufort Sea (e.g. Walker, 1973; Reimnitz, 2002; Alkire and Trefry, 2006). While these show that the plumes are very

shallow and strongly stratified, there is virtually no information on temporal and spatial variations in the plume's structure.

Our approach consists of idealized numerical experiments in which the landfast ice is parameterized as a surface stress over all, or portions, of a shelf that receives a temporally-varying buoyant coastal influx. The applied river discharge mimics that of small arctic rivers, such as the Colville River (Figure 3.1), on Alaska's North Slope. As with all true arctic rivers, the Colville discharge ceases from mid-October through mid-May when its watershed is frozen. Runoff increases abruptly in late May/early June during the spring freshet when ~ 85% of the annual discharge occurs during a 2-week period. Thereafter its discharge diminishes rapidly through summer and more slowly into fall. Of particular interest to us is the spring freshet, since this occurs when landfast ice is still intact. On an annual basis, the freshet also carries the largest concentrations of dissolved and suspended terrigenous materials (Trefry et al., 2009); hence, the spreading of under-ice plumes bears crucially on the biogeochemistry of arctic shelves. Landfast ice is also a pervasive feature of the Mackenzie and Eurasian shelves, which in addition to the spring pulse receive a steady river discharge throughout winter, and to some extent our results apply to these shelves as well.

The model configuration mimics the Alaskan Beaufort Sea shelf in terms of the river discharge (timing and magnitude, Figure 3.1), bottom slope, ice cover, and density of the ambient shelf water during the spring freshet. Landfast ice, which is anchored in place along the 2 m isobath and extends offshore to the 20 m isobath (Reimnitz, 2002), covers the inner portion of most arctic shelves from October through June. On the

Alaskan Beaufort Sea shelf, the landfast ice edge is typically 20 - 30 km offshore, although it can extend 40 km or more (Mahoney et al., 2007). In contrast, the landfast ice edge of the East Siberian Sea can be  $\sim 100$  km offshore (Morris et al., 1999). In May, at the conclusion of the freezing season, inner shelf waters are at their maximum density,  $\rho$ , of  $\sim 1025 \text{ kg m}^{-3}$  (Weingartner et al., 2009). Since tidal currents are weak ( $\sim 0.02 \text{ m s}^{-1}$ , Kowalik and Proshutinsky, 1994) and rivers debouche directly onto the shelf, the density of the inflowing river water at the coast is  $1000 \text{ kg m}^{-3}$ .

Measurements of the ice-ocean drag coefficient show that ice roughness affects the strength of the frictional coupling between landfast ice and the ocean. Shirasawa (1986) measured the quadratic ice-ocean drag coefficients beneath landfast ice in the Canadian Archipelago and found that these varied from  $5 \times 10^{-3}$  (for smooth ice) to  $9 \times 10^{-3}$  for rough ice. Based on these values, the linear ice friction coefficient,  $r_{ice}$ , varies between  $10^{-4}$  and  $10^{-3} \text{ m s}^{-1}$ . McPhee (1990) reports a similar range for pack ice over the basin and noted that the drag coefficient can vary substantially over short distances. He attributed these variations to form drag (pressure drag) associated with deep ice keels and internal waves.

For an ice-free setting, Garvine (1999) found that if the plume Kelvin number of a buoyant inflow is greater than 1 then rotation is of first-order importance in the plume's dynamics and advective terms are negligible. As defined by Garvine (1995), the plume Kelvin number is  $K = \gamma L / Rd$ , where  $\gamma$  is the "slimness" of the coastal current,  $L$  is the along-shore scale of the buoyant plume, and  $\gamma L$  is the cross-shore width of the coastal current, so that the plume Kelvin number is the ratio of the coastal current width to the

Baroclinic Radius of deformation ( $Rd$ ). Because of the dearth of observations of the Colville River it is not possible to use Garvine's (1999) definition of the plume Kelvin number. Though based on the inlet Kelvin number (e.g. Huq, 2009),  $K = W/Rd$  where  $W$  is the inflow width, we expect rotation to be important. For the Colville River,  $W$  is  $\sim 50$  km and  $Rd = \sqrt{g'\delta} / f$ , where  $g'$  is the reduced gravity,  $\delta \approx 2$  m is the inlet depth, and  $f$  is the Coriolis parameter ( $f = 1.37 \times 10^{-4} \text{ s}^{-1}$ , for  $\varphi = 70^\circ \text{ N}$ ). We find that  $Rd \approx 5$  km, so  $K = 9.8$ . (Note that even for an inlet width of 10 km, the approximate width of the East Channel of the Colville River where most of its discharge enters the shelf,  $K > 4$ .)

For  $K > 4$ , Garvine (1999) found that the coastal current downstream from the inflow is slim compared to the along-shore scale of the plume (i.e. the coastal current is narrow and/or extends for large along-shore distances). It is not clear if this  $K > 4$  criterion applies to ice-covered shelves, since Ingram (1981) found that under-ice plume areas tend to be greater than plume areas in ice-free conditions. However, Ingram's (1981) research and subsequent work on under-ice plumes (e.g. Granskog et al., 2005; Li and Ingram, 2007) were obtained from settings where  $K < 1$  and hence rotation is likely unimportant in these systems. Nevertheless, we find (Chapter 1 of this thesis) that a rotating, lateral inflow onto a shelf migrates farther offshore (and does not extend as far downstream) under landfast ice compared to the ice-free setting.

Herein we examine a suite of numerical experiments and evaluate the differences in buoyant plume behavior due to the inclusion of a surface stress induced by the interaction between the plume and immobile landfast ice. Section 3.2 describes the numerical model configuration. The results of various experiments that include a river

inflow onto a shelf that has no ice cover, a partial ice cover, and is entirely covered by ice are presented in section 3.3. Section 3.4 summarizes and concludes the paper.

### ***3.2 Model description***

We use the Regional Ocean Modeling System (ROMS; Song and Wright, 1998; Shchepetkin and McWilliams, 2005) to explore some of the processes that control buoyancy-forced flows beneath a landfast ice cover. ROMS is a finite difference, free surface model, which uses stretched, terrain-following coordinates in the vertical ( $s$ -coordinate, Song and Haidvogel, 1994) to solve the primitive equations governing fluid motion. The  $s$ -coordinate model is desirable when dealing with continental shelf topography and allows for increased resolution in the top and bottom boundary layers. For turbulent closure, we employ the Mellor-Yamada level 2.5 (Mellor and Yamada, 1982) mixing scheme, where eddy diffusivity is calculated based upon the local flow and stratification. The domain is a rectangle 200 km long (west to east,  $0 < x < 200$  km) and 100 km wide ( $0 < y < 100$  km). The southern boundary ( $y = 0$ ) is a straight coastline and depth,  $h$ , increases linearly offshore ( $h = h_0 + sy$ ), where  $h_0 = 2$  m is the depth at the coast. The bottom slope,  $s = 7.5 \times 10^{-4}$ , approximates that of the ABS. Cartoons of the model domain and river forcing are given in Figures 3.2A-C. To resolve the thin boundary layers under the ice and near the bottom, we use 20 vertical levels (1/10 m resolution at the coast), and we tune the  $s$ -coordinate so that there is increased resolution in the surface and bottom boundaries layers (e.g. Hedstrom, 2000).

To ascertain the effect of a landfast ice cover on a coastal river influx, we conducted a series of idealized numerical experiments. In experiment 1 the shelf is ice-

free. In experiment 2, landfast ice is included as a surface stress and partially covers the shelf: there is ice from the coast offshore to the 20 m isobath (26 km offshore) where it ends abruptly. In experiment 3, landfast ice covers the entire domain. We parameterize the stress of the ice on the ocean surface as  $\tau_{ice} = -r_{ice}\bar{u}_{surf}$ , where  $u_{surf}$  is the surface velocity. We also include linear bottom stress,  $\tau_b = -r_b\bar{u}_b$ . Note, both the surface and bottom stresses have the same sign and except where explicitly noted,  $r_{ice} = 10^{-4} \text{ m s}^{-1}$  and  $r_b = 3 \times 10^{-4} \text{ m s}^{-1}$ .

The river discharges directly onto the shelf between  $x = 75 \text{ km}$  and  $125 \text{ km}$  (at  $y = 0$ ). The freshwater density,  $\rho$ , is  $1000 \text{ kg m}^{-3}$  and the discharge evolves through time as a skewed Gaussian (Figure 3.2). The ambient shelf water density is  $1025.7 \text{ kg m}^{-3}$ . We focus on a one-month period during which the river discharge varies from  $0$  to  $6000 \text{ m}^3 \text{ s}^{-1}$  and then decreases. About 1 month after discharge commences the ice cover is almost entirely melted and thereafter we expect the plume dynamics to be controlled by ambient winds (Weingartner et al., 2009).

### 3.3 Results

Contours of the surface density anomaly,  $\Delta\rho$  ( $\rho - 1000$ ,  $\text{kg m}^{-3}$ ) at days 10, 20 and 30 days are shown for the ice-free (Figures 3.3A-C), partially ice-covered (Figures 3.3D-F), and completely ice-covered (Figures 3.3G-I) experiments. There are several striking differences among the experiments. First, the offshore extent of the plume increases with increasing ice width and offshore broadening of the plume continues even after discharge begins to decrease on day 10. Second, the density gradient across the front at the plume's



offshore edge is strongest under-ice-free conditions and weakest when ice covers the entire offshore domain. Third, the anti-cyclonic bulge centered near  $x = 80$  km,  $y = 10$  km in the ice-free case is broader and displaced eastward (downstream in the Kelvin wave propagation sense) when ice is present. Fourth, the meanders along the offshore plume boundary evident in the ice-free case are suppressed when ice is present.

From YC97 the diameter of the anti-cyclonic bulge near the river mouth for a surface-advected plume is:

$$y_s = \frac{2(3g'h_0 + v_i^2)}{f(2g'h_0 + v_i^2)^{1/2}} \quad 3.1$$

where  $v_i$  is the inlet velocity (a maximum of  $0.06 \text{ m s}^{-1}$  for our inflow),  $h_0$  is the inlet depth (2 m) and  $f$  is the Coriolis parameter. For both  $v_i = 0.06 \text{ m s}^{-1}$  (the inlet velocity at peak discharge) and  $v_i = 0.02 \text{ m s}^{-1}$  (the inlet velocity at day 30),  $y_s$  is  $\sim 21$  km and in both cases  $y_s$  is  $\sim 4$  times  $Rd$  (5 km). This is consistent with the ice-free experiment where the maximum offshore distance of the bulge is  $\sim 20$  km (at  $x = 80$  km) on day 10 (Figure 3.3A). In contrast, when ice is present (Figures 3.3D and G), the density front is slightly farther offshore ( $\sim 3$  km) by day 10 and shifted downstream to  $x = 120$  km. However, by day 30, the  $\Delta\rho = 25 \text{ kg m}^{-3}$  contour is nearly 60 km offshore in experiment 3 compared to only 30 km in the ice-free case. In the partially ice-covered experiment 2, the same density contour extends 33 (36) km offshore on day 20 (30) and  $\sim 7$  (10) km offshore of the ice edge. The distance between the ice edge and the distance to the offshore front (7 km on day 20) is the YC97 scale for the values of the bulge just inshore

of the ice edge where  $\Delta\rho \approx 15 \text{ kg m}^{-3}$ ,  $v \sim 0.035 \text{ m s}^{-1}$  and  $h_0 = 2 \text{ m}$  is the bulge depth at the ice edge.

Note that the YC97 scaling is derived by assuming that the radial momentum balance of the freshwater bulge is between the radial change in the azimuthal velocity, Coriolis and the pressure gradient, which is a function of the radial thinning of the plume. YC97 refer to this as the cyclostrophic balance whereas Horner-Devine (2009) refers to it as the gradient wind balance. For an unsteady freshwater discharge, the time dependent terms in the momentum balance are initially important. However Yankovsky, et al. (2001, hereafter YHM01), and Horner-Devine (2009) show that YC97 adequately describes the initial scale of unsteady anti-cyclonic bulges as well. This indicates that the radial momentum balance of the anti-cyclonic bulge in experiment 1 and in the portion of the bulge offshore of the ice edge in experiment 2 is close to the gradient wind balance.

Beneath the landfast ice cover, the bulge's radius is greater than the bulge in the ice-free case. The increase in plume area is due to the boundary layer circulation induced by ice-ocean friction. This is suggested by the contours of the surface along- and cross-shore velocities,  $u_{surf}$  and  $v_{surf}$  shown in Figures 3.4 and 3.5, respectively (as in Figure 3.3 with the rows being different ice covers and the columns different times.).

Figures 3.4 and 3.5 indicate that in the absence of ice, the near-shore circulation west of the river mouth ( $x < 75 \text{ km}$ ) is upstream and offshore. At the offshore edge of the plume ( $x = 80 \text{ km}$ ,  $y = 20 \text{ km}$ ) the circulation turns downstream and onshore. The anti-cyclonic turning (and its subsequent time evolution) in the ice-free case conforms to the behavior of the surface-advected plume generated by a time-varying river discharge

described by YHM01. In both the ice-covered experiments 2 and 3 the surface circulation is also anti-cyclonic, but the flow around the bulge near the river mouth is much weaker. For example, on day 10 at  $x = 74$  km,  $y = 3$  km,  $u_{surf} = -0.3$  m s<sup>-1</sup> and  $v_{surf} = 0.15$  m s<sup>-1</sup> in the ice-free case but for both the partial and total ice-covered cases the corresponding values are 0.08 m s<sup>-1</sup> and  $< 0.01$  m s<sup>-1</sup>, respectively. Note also that in experiment 2, the maximum along-shore  $u_{surf} \sim 0.45$  m s<sup>-1</sup> occurs seaward of the ice edge and is part of a buoyancy-forced ice edge jet. The maximum  $u_{surf}$  moves  $\sim 40$  km downstream over 10 days, so that by day 20 the maximum is at  $x = 160$  km and on day 30 it is at  $x = 200$  km. This feature and the effect of the ice edge are discussed in more detail later.

Although an ice cover reduces the surface velocities, we show later that consistent with a frictional under-ice boundary layer, velocity maxima under an ice cover are subsurface and the vertical current profiles differ between experiments. Because of the surface friction, positive  $v_{surf}$  induces westward transport within the under-ice boundary layer, i.e., transport is to the right (left) of the direction of the stress (velocity). Thus for an anti-cyclonic surface advected buoyant plume, a landfast ice cover and rotation lead to an increase in the offshore spreading of the plume. Further, since the vertically integrated transport in the under-ice boundary layer is proportional to the internal fluid velocity, the effects of the frictional ice cover are strongest where the velocities are greatest, i.e., within fronts. Indeed from the surface density contours, we see that the frictional ice cover leads to diffuse fronts compared to the ice-free case.

Surface plots of vertical velocity,  $w$ , from experiments 1 (Figures 3.6A-C), 2 (Figures 3.6D-F) and 3 (Figures 3.6G-I) highlight the location of the offshore front that

marks the transition between fresh river water and ambient shelf water and where generally the vertical velocity is greatest. As with the surface contours shown previously, the intensity of the vertical velocity varies in time, space and with ice coverage. In experiment 1, the vertical velocity alternates between upwelling ( $10^{-6} \text{ m s}^{-1}$ ) inshore of the outer front, to downwelling ( $10^{-6} \text{ m s}^{-1}$ ) within the front, to upwelling ( $10^{-6} \text{ m s}^{-1}$ ) seaward of the front. This is similar to previous studies of river plumes, e.g., Figure 9 from Fong and Geyer (2001) shows the same pattern of up- and down-welling at the outer edge of a buoyant plume. Also Figure 4 in Chapman and Lentz's (1994) study of buoyant plumes controlled by bottom friction shows a similar pattern. In experiments 2 and 3, the up/down-welling pattern and magnitudes are similar to the ice-free experiment though the cross-shore scale is stretched: in experiment 1 the frontal circulation occupies  $\sim 2 Rd$  whereas in experiment 3 the frontal circulation is  $> 3 Rd$  wide.

In addition to the effect of the surface stress on the under-ice flow, the ice-edge has a pronounced influence on the flow and density fields. The change in surface stress across the ice edge reduces offshore spreading of the under-ice plume when compared to the case of complete ice coverage; outside of the ice cover, the bulge has a finite offshore extent (as described by the YC97 scale) and the importance of the Coriolis effect means the bulge circulation turns shoreward, whereas under the ice there is an offshore tendency due to the ice surface stress. This is apparent in Figures 3.4D-F and 3.5D-F. Seaward of the ice edge where the gradient wind balance holds,  $v_{surf}$  changes direction and is onshore seaward of the ice edge for  $x > 110 \text{ km}$ . The effect of the along-shore change in the sign of  $v_{surf}$  on the under-ice density field is evident in Figure 3.3, where the density anomaly

spreads offshore less when ice width is finite (Figures 3.3D-F) than for the case of complete ice coverage (Figures 3.3G-I).

Note also that the along-shore flow is sheared across the ice edge. Shoreward of the ice edge,  $u$  (Figures 3.4D-F) is positive and small compared the offshore flow while seaward of the ice edge  $u$  positive and greater than inshore of the ice edge. The cross-shore shear in  $u$  is consequence of the transition between ice (where the surface stress slows the along-shore flow) and ice-free. Furthermore, the cross-shore flow (Figures 3.5D-F) diverges near  $x = 80$  km,  $y = 26$  km (the upstream edge of the anti-cyclonic bulge). Here  $v = 0.067$  (0.11)  $\text{m s}^{-1}$  shoreward (seaward) of the ice edge (on day 30). Downstream, where the offshore anti-cyclonic bulge circulation is directed shoreward (i.e. near  $x = 150$  km,  $y = 26$  km) the cross-shore flow is convergent at the ice edge with  $v = -0.05$  (-0.01)  $\text{m s}^{-1}$ , shoreward (seaward) of the ice edge on day 30. Figures 3.6D-F show that there is an area of alternating up- and down-welling where the cross-shore flow converges and diverges at the ice edge. The total width of the ice edge up/down-welling cell is  $\sim 1 Rd$  (5 km). Cross-sections of vertical velocity (shown later) show that the vertical circulation near the ice edge is shallow and at depths  $> 3$  m there is downwelling.

For a vertically averaged inflow, in Chapter 1, we showed that the change in surface stress across the ice edge leads to cross-shore shear in the along-shore velocity and divergence/convergence in cross-shore transport similar to that noted above. In the present study, the change in surface stress across the ice edge and interaction of the offshore flow field with the under-ice circulation leads to the divergence/convergence in the cross-shore velocity across the ice edge and the complex vertical circulation at the ice

edge. Since density determines the circulation in the present study, there are additional variables to consider than in the simpler linearized vertically averaged study of Chapter 1. The ice edge effect is discussed further in regards to the momentum and density balances.

In addition to modifying the near field circulation in the anti-cyclonic bulge, an ice cover changes the far field response to a time-dependent river discharge as well: while a downstream coastal current is present in all experiments (c.f. Figures 3.4 - 3.6) the ice cover changes the offshore extent of the coastal current and the momentum balance of the coastal current. The coastal current domain is taken as the area downstream (in the Kelvin wave sense) of where the anti-cyclonic bulge circulation is shoreward (c.f. Garvine, 1987), i.e., the area downstream of the bulge within which the flow is primarily directed downstream. In experiment 1 at  $x = 200$  km, the coastal current width is  $\sim 10$  km on day 10 and 20 km by day 30. Thus the plume Kelvin number,  $K = \gamma L / Rd$  is between 2 and 4 and as expected from Garvine's (1999) results the cross-shore scale of the coastal current  $\ll$  the along-shore scale and, within the coastal current, the momentum balance is nearly geostrophic (although local acceleration is important initially). Since our domain only extends 200 km east-west we can only say that along-shore scale of the coastal current (the distance between the eastern edge of the river mouth and the eastern boundary) is  $> 75$  km.

In the presence of ice, the coastal current spreads offshore in much the same manner as discussed in Chapter 1 of this thesis for the case of a lateral inflow. The under-ice stress opposes the downstream tendency of the coastal current that is then deflected offshore by the Coriolis acceleration. Thus within the coastal current of the ice-covered

experiments presented here, as well as in Chapter 1, ice-ocean friction, Coriolis, and the pressure gradient are all important in the along-shore momentum balance (i.e., the along-shore momentum balance within the plume is the same as in a bottom Ekman layer). Furthermore, in experiment 2, convergence at the ice edge limits the offshore spreading of the coastal current in comparison to experiment 3. Overall, by day 10 the coastal current has not formed in either ice-covered experiment. By day 30 the width of the coastal current is  $\sim 30$  km ( $6 \times Rd$ ) in experiment 2 and 40 km wide ( $8 \times Rd$ ) in experiment 3. In both experiments 2 and 3, the width is greater than expected based on Garvine's 1999 results and the slimness of the coastal current,  $\gamma$ , is not  $\ll 1$ . Note since our domain is likely short compared to the along-shore extent of the coastal current, we cannot state definitively that  $\gamma$  is  $\ll 1$  for entire coastal current domain. Also in experiment 2, the energetic frontal feature offshore of the ice edge (noted above) propagates along the ice edge as it is prevented from approaching the coast by offshore flow under the ice cover.

Fong and Geyer (2001) examined the response of a river plume to upwelling winds (an external surface stress) and found that upwelling winds tend to move a buoyant plume away from the coast and lead to thinning of the plume. In the present study, under-ice stress leads to an increase in the offshore spreading of the plume, similar to Fong and Geyer's findings, however, the under-ice plume is thicker in the presence of ice-ocean friction than in the absence of this friction. Hence, the comparison between an external surface stress, such as wind, that provides energy for mixing and an internal surface stress

such as an immobile ice cover that removes energy through friction is not exactly analogous.

Figure 3.7 summarizes the effect of the ice and ice edge on spreading of the under-ice plume in terms of the plume area versus ice width. We computed the plume area on day 30 over the region of the sea surface circumscribed by the  $\Delta\rho = 25 \text{ kg m}^{-3}$  isopycnal between  $0 < y < 100 \text{ km}$  and  $0 < x < 200 \text{ km}$  (thus encompassing both the anti-cyclonic bulge and the coastal current). The figure compiles experimental results for a variety of ice widths after 30 days of model run time. Over the time period examined, plume area increases with ice width for ice widths  $< \sim 60 \text{ km}$ .

In addition to changing the offshore spatial extent of a freshwater discharge, a landfast ice cover alters the along-shore freshwater flux,  $F$  ( $10^3 \text{ m}^3 \text{ s}^{-1}$ ), defined (per Whitney and Garvine, 2005) as:

$$F = \int \left( \frac{S_a - S}{S_a} u \right) da$$

where  $S_a$  is the ambient shelf salinity (32),  $u$  is along-shore velocity and  $da = dzdy$  is the element of area. The integral is taken from the coast to the offshore boundary,  $0 \leq y \leq 100 \text{ km}$  and from the surface to the bottom.

Figure 3.8 shows  $F$  at  $x = 200 \text{ km}$  along with the river discharge. There is a delay between the river influx and  $F$  at the eastern boundary. In the absence of ice the delay is  $\sim 6$  days, whereas when ice is present the delay is 10 days. From Figure 3.8 we calculate that the plume propagates eastward from the downstream bank of the river ( $x = 125 \text{ km}$ ) to  $x = 200 \text{ km}$  at  $\sim 0.14 \text{ m s}^{-1}$  in the absence of ice and at  $\sim 0.08 \text{ m s}^{-1}$  when ice is present.



We expect that the freshwater plume should propagate at the speed of a gravity current nose and from Lentz and Helfrich (2002), the speed of a gravity current nose is  $c_p = c_w(1+c_w/c_a)$  where  $c_w = (2qg')^{1/4}$ , and  $c_a = sg'/f$  where  $g'$  is the reduced gravity within the nose of the plume and  $q$  is the transport within the nose ( $g' = 0.23 \text{ m s}^{-2}$  and  $s = 7.5 \times 10^{-4}$  in all 3 experiments). For experiment 1 (2 and 3), the nose speed predicted by the Lentz and Helfrich (2002) formula is 0.18 (0.14)  $\text{m s}^{-1}$ .

For both the ice-free and the ice-covered experiments, the speed calculated using the Lentz and Helfrich (2002) formula is greater than the speed of the freshwater calculated using Figure 3.8. Though in all three experiments, surface plots of the density (such as those in Figure 3.3) show that the nose speed between 160 and 200 km is the same as the value obtained using the Lentz and Helfrich (2002) formula. Thus, the difference between the theoretical speed (the 2002 Lentz and Helfrich speed) and the speed of the freshwater (calculated from Figure 3.8) is a consequence of the indirect pathway that the freshwater takes from the river mouth, i.e., the freshwater propagates farther than the 75 km between the eastern edge of the river mouth and the eastern boundary, whereas the difference in nose speed between the ice-free and ice-covered experiments is due to differences in the nose transport,  $q$ . In experiment 1 (2 and 3)  $q \approx 34$  (11)  $\text{m}^3 \text{ s}^{-1}$ . The differences in transport between the ice-free and ice-covered experiments are due to differences in mixing introduced by the inclusion of the ice cover. Mixing is discussed at the end of this section, in regards to the density balance.

In the absence of ice,  $F$  is initially greater (by more than order of magnitude) than in the ice-covered cases, although by day 25 all values of  $F$  are of the same order of

magnitude. In all experiments a substantial fraction of the 30-day cumulative freshwater discharge remains upstream of the eastern boundary,  $x = 200$  km. In the ice-covered cases only 22% of the total discharge escapes through the eastern boundary, while for the ice-free case the downstream flux removes 50% of the cumulative discharge. Note also that while  $F$  is the same for the partial and completely ice-covered cases prior to day 24, beyond this time  $F$  under partially ice-covered conditions exceeds that of the other cases. The increase after day 24 for the partially ice-covered case is due to the arrival at the eastern boundary of the pulse of the strong along-shore flow at the ice edge noted above. In summary, a landfast ice cover increases the upstream and offshore freshwater transport so that the downstream along-shore freshwater flux is delayed and substantially smaller than when ice is absent.

Figure 3.9 depicts the integrated transport stream-function ( $\text{m}^3 \text{s}^{-1}$ ) for experiment 1 (Figures 3.9A-C), experiment 2 (Figures 3.9D-F) and experiment 3 (Figures 3.9G-I) at 10, 20 and 30 days, respectively. In experiment 1, the anti-cyclonic bulge develops quickly and is clearly visible by day 10 near the river mouth at  $x = 90$  km,  $y = 10$  km. Thereafter the bulge intensifies, grows, and by day 30 has moved 20 km downstream and offshore by 10 km. After discharge relaxes, YHM01 refer to the bulge as an eddy. A second bulge, corresponding to the “secondary bulge” that YHM01 found, is centered at  $x = 130$  km,  $y = 10$  km on day 30 (Figure 3.9C). In experiment 1, the downstream coastal current is very narrow; it is  $< 10$  km wide at day 10 and broadens to between 15 and 20 km by day 30.

In contrast to the ice-free experiment, circulation patterns are less distinct and develop more slowly in both experiments 2 and 3. In experiment 2, a distinctive bulge only appears by day 20 but it is centered at  $x = 100$  km,  $y = 15$  km and farther downstream and offshore than in experiment 1. No “secondary bulge” develops in this case, although the areal extent of the single bulge is similar to that of the primary and secondary bulges of experiment 1, and the total transport within the bulge in experiment 2 is less than in experiment 1. Finally, there is no distinct coastal current evident when ice is present, but instead a diffuse downstream transport between the coast and slightly offshore of the ice edge. The stream-function differences between experiments 2 and 3 are smaller than those between experiments 1 and 2 and the gradient of the positive transport contours is greater in experiment 2 (Figures 3.9D-F) than in experiment 3 (Figures 3.9G-I), though the magnitude of positive transport is similar.

In all three experiments a sea level set down develops with time such that the sea level at the closed offshore boundary (the northern boundary is a wall) is (relatively) low and the sea level at the coast is (relatively) high. The magnitude of the sea level difference increases with time and distance from the coast. Further, the magnitude of the sea level difference varies among the experiments and the cross-shore sea level slope is greatest in experiment 2 and smallest in experiment 1. The cross-shore sea level slope leads to positive (eastward) along-shore transport in all three experiments. On day 30 experiment 1, the sea level slope accounts for an average geostrophic along-shore velocity between  $60 < y < 100$  km of  $0.03 \text{ m s}^{-1}$  whereas on day 30, experiment 2 (3) this cross-shore sea level slope accounts for an average geostrophic along-shore velocity of

0.06 (0.04)  $\text{m s}^{-1}$  for the same area. The magnitude of the set down is dependent on the amount of freshwater mixed offshore and the total freshwater retained in the domain. In experiment 3, freshwater is mixed farther offshore than in experiment 2 with the result that the cross-shore sea level slope is less in experiment 3 than experiment 2. Since in experiment 1 less freshwater is retained within the domain overall than in experiments 2 and 3, the result is the smallest cross-shore sea level slope among the three experiments.

These sea level differences between and among experiments are reflected in the stream-function contours and the differences are most notable offshore, where the stream-function are negative. The result of the sea level set down is that in experiment 1, the magnitude of the (negative) integrated transport at  $y = 70$  km increases the least with time (between 10 and 30 days, Figures 3.9A-C) among the experiments and the total negative transport is the smallest in magnitude, whereas in experiment 2 (Figures 3.9D-F), the total (negative) transport increases the most with time and is the greatest after 30 days among the experiments.

Other notable differences between the stream-function are that in experiment 2 due to the increase in transport seaward of the ice edge (associated with the buoyant jet mentioned previously), the 4000 contour is farther offshore (note the protuberance of the transport contour at  $x = 140, y = 20$  km) than in experiment 3. Also note that by day 30, the 0 contour is farther offshore in panel F (experiment 2) than in panel I (experiment 3). This difference is due to the fact that for  $t > 24$  days,  $F$  is slightly larger and increasing for experiment 2, whereas in experiment 3,  $F$  is decreasing slowly with time.

Since the anti-cyclonic circulation and the increased downstream and offshore displacement of the bulge under an ice cover are so clear in the stream-function contours, it is pertinent to note that Nof and Pichevin (2001) found that the location of the center of an anti-cyclone due to a buoyant outflow is related to the radius of the bulge; they found that an anti-cyclonic bulge moves offshore and downstream with time, because as the bulge grows it pushes itself away from the coastal wall, while at the same time the center of the anti-cyclone shifts downstream. In the present study, the increase in bulge width due to under-ice friction means the center of the anti-cyclone is necessarily farther offshore and downstream compared to the ice-free scenario.

To further explore the time-dependency of the flow, described in detail for the ice-free scenarios by YHM01, we contoured the surface values of  $\Delta\rho = 25 \text{ kg m}^{-3}$  at 5-day intervals for each experiment (Figures 3.10A-C). The offshore position of this contour increases with time and ice width so that the plume area is minimum for no ice and maximum for complete ice coverage. In all three experiments, the plume is initially small and increases in area with time. This is similar to what YHM01 found. Indeed Figure 3.10A is comparable and similar to their Figure 3.6. Note also that in experiment 3 the position where the plume width is greatest shifts downstream with increasing time. This is a consequence of the downstream shift of the bulge center with time as the bulge grows.

Figure 3.10D presents the results of Figures 3.10A-C in a slightly different manner: on the  $y$ -axis is the distance from the coast to the  $\Delta\rho = 25 \text{ kg m}^{-3}$  contour (at  $x = 130 \text{ km}$ ) versus time for the three experiments. The width of the plume asymptotes for

experiments 1 and 2 at  $\sim 20$  and  $\sim 40$  km, respectively, whereas in experiment 3, plume width continues to expand to  $> 50$  km during the 30 day time period considered at a linear rate of  $\sim 1.5$  km per day. Note that this trend continues up to 40 days (the simulations were run for 10 days longer than the 30 days shown here, 40 day data not shown). Also not shown, in simulations of steady discharge ( $Q = 6,000 \text{ m}^3 \text{ s}^{-1}$ ) conditions that mimic larger Arctic rivers that flow year round under an ice cover, a steady coastal current forms under-ice-free and partial ice coverage (i.e., the width of the plume asymptotes as it does in the variable discharge cases shown). When ice coverage is complete, plume width increases up to 60 days (the maximum length of the additional experiments) at  $\sim 1.5 \text{ km d}^{-1}$  and exceeds 50 km by day 30.

Additional circulation details are evident in cross-sections of density (Figures 3.11A-F), and the along- (Figures 3.12A-F), cross-shore (Figures 3.13A-F), and vertical velocities (Figures 3.14A-F) for the various experiments. The sections are constructed at  $x = 100$  km (the midpoint of the river mouth). In the ice-free experiment the density sections show two distinct fronts by days 20 and 30 (Figures 3.11B-C). The inner front is at  $y \approx 5$  km and the more diffuse, offshore front is at  $y = 15$  km on day 20 and  $y = 20$  km on day 30. The offshore front is the outer edge of buoyant water that has circulated around the anti-cyclonic bulge near the river mouth and the inner front is the inner edge of the anti-cyclonic bulge.

Two fronts are also apparent in experiment 2 on day 20 (Figure 3.11E), with one centered near  $y = 10$  km and one at  $y \sim 35$  km, both of which are part of the diffuse anti-cyclonic bulge circulation, which has been modified by the presence of the ice and the ice

edge. These fronts are more clearly separated from one another by day 30 (Figure 3.11F). In contrast, the cross-shore density gradient in experiment 3 (Figures 3.11G-I) is nearly uniform and the only clear indication of a front is at the offshore edge of the plume.

Plume depth is also slightly greater in the presence of ice. For example, in experiment 1, day 30, the  $\Delta\rho = 25 \text{ kg m}^{-3}$  contour intersects the bottom at the  $\sim 7 \text{ m}$  isobath whereas in experiments 2 and 3, this contour intersects the bottom at the  $\sim 8 \text{ m}$  isobath on day 30. Cross-shelf sections of density from different locations along the coast show that the plume depth under an ice cover exceeds the depth of the ice-free plume elsewhere as well suggesting that the ice cover leads to both deepening and widening of the river plume. Also there is a slight steepening of the density contours near the surface under the ice cover compared to the ice-free experiment. This and the deepening of the under-ice plume are discussed at the end of this section.

Cross-shore sections of the velocity components highlight some of the features of the under-ice flow that are difficult to see in the cross-shore density sections. In experiment 1, the along-shore velocity maxima in Figures 3.12A-C, coincide with the density fronts (Figures 3.11A-C) so that eastward velocities are largest at the surface ( $0.4 \text{ m s}^{-1}$ ) and decrease with depth (to near zero slightly above the bottom boundary layer where the velocity is upstream) and time (to  $\sim 0.2 \text{ m s}^{-1}$  on day 30). Note the dashed black contour lines are the  $\Delta\rho = 11$  (shoreward) and  $23$  (seaward)  $\text{kg m}^{-3}$  contour lines. These two contours are included in all of the cross-shore velocity profiles. The  $\Delta\rho = 23 \text{ kg m}^{-3}$  contour tracks the outer edge of the outer front. Rather than tracking frontal structure, the  $\Delta\rho = 11 \text{ kg m}^{-3}$  tracks the offshore spreading and at later times contraction

of the nearshore density contours with time. When ice is present (experiments 2 and 3), due to under-ice friction the maximum under-ice along-shore velocities are  $\sim 0.5$  m below the surface. For example, on day 10, in both experiments 2 and 3 under the ice cover the maximum eastward (positive, downstream) along-shore velocity is located at  $y = 11.5$  km and is  $0.13 \text{ m s}^{-1}$ . It is apparent from the figures that the under-ice  $u_{max}$  migrates offshore and the velocity magnitude decreases with time so that by day 30  $u_{max}$  is  $\sim 45$  km offshore in experiment 3 and has decreased by  $0.04 \text{ m s}^{-1}$  to  $0.09 \text{ m s}^{-1}$ . In experiment 2, the under-ice  $u_{max}$  eventually merges with the energetic flow offshore of the ice edge (in both the bulge and downstream) and the offshore migration of the under-ice velocity maximum is impeded by the flow field offshore of the ice edge.

While the change in position and magnitude of the along-shore velocity maximum with time are important, another pertinent feature of the cross-shore sections of along-shore velocity is the depth (and distance from the coast) at which the along-shore velocity reverses from positive (directed downstream) to negative. YC97 use this depth (and distance from the coast) to distinguish between buoyant plumes controlled by bottom friction, intermediate plumes and surface trapped plumes. YC97 found that the isobath at which the along-shore flow reverses from downstream to upstream is given by

$h_b = \sqrt{2Qf / g'}$ , where  $Q$  is the inflow volume ( $\text{m}^3 \text{ s}^{-1}$ ). For our parameter values ( $Q = 6000 \text{ m}^3 \text{ s}^{-1}$ ) this depth is  $\sim 3$  m, which is greater than the depth at which the along-shore velocity reverses in all three experiments:  $u$  reverses from positive to negative at the coast in Figure 3.12 on day 10 at depths  $< \sim 2$  m in all three experiments indicating that in all experiments the plume is surface trapped.



The depth at which the along-shore velocity reverses at the coast shoals with increasing time (Figure 3.12 days 20 and 30) until on day 30, along-shore velocity at the coast is negative (upstream) at all depths in all experiments and  $u$  reverses (from upstream to downstream) farther offshore. In experiment 1 the cross-shelf extent of this shoaling downstream flow (that is part of the bottom boundary layer discussed later) is narrow and extends less than 2 km from the coast at the surface on day 30, compared to the ice-covered experiments where the near coast surface flow is entirely upstream up to 8 km from the coast on day 30 (experiment 3).

The separation of the downstream flow from the coast with time was described for a similar ice-free case by YHM01, who found that as river discharge decreases, the anti-cyclonic bulge forms a closed eddy in which the transport increases with time. The nearshore upstream flow visible in the cross-shore contours is upstream transport within this eddy. The development of the eddy in our experiments is clearly visible in the stream-function contours shown previously (Figure 3.9), from which we see that the upstream shift in position and increased along- and cross-shore extent of the eddy under an ice cover accounts for the differences in the width of the nearshore upstream flow visible in the cross-shelf sections of  $u$ . The stream-function contours imply that the width of the nearshore upstream flow should vary with  $x$ -position, and indeed we find that this is the case. In all three experiments, the nearshore, upstream flow results in onshore bottom boundary layer flow near the coast that is visible in all the cross-shore velocity sections (Figures 3.12, 3.13 and 3.14).

Cross-shore sections of  $v$  (Figure 3.13) highlight the differences in the location and spatial scales of the anti-cyclonic bulge among the different experiments. In experiment 1 (Figures 3.13A-C) nearshore ( $y < \sim 8$  km)  $v$  is positive (offshore) whereas farther offshore ( $y > 8$  km),  $v$  is onshore, i.e., the cross-section cuts across the portion of the anti-cyclonic bulge in which the circulation in the outer portion of the bulge is shoreward. As with  $u$ , outside of the bottom boundary layer,  $v$  is greatest at the surface and decays with depth. In comparison, in both experiments 2 and 3  $v$  is offshore everywhere. The downstream shift and increased lateral expanse of the anti-cyclonic bulge under an ice cover visible in the surface contours of density (Figure 3.3), velocity (Figures 3.4 and 3.5) and integrated transport (Figure 3.9) explain the differences in cross-shore velocity between experiments noted at the location ( $x = 100$  km) where the cross-shore sections shown in Figures 3.11-3.14 were constructed. Note also that the under-ice  $v_{max}$  in experiments 2 and 3 (day 10) are  $\sim 0.08$  m s<sup>-1</sup> and located at  $y = 8.5$  km (3 km shoreward of the under-ice  $u_{max}$  noted above) at a depth of 0.04 m. Similar to the under-ice  $u_{max}$ , the under-ice  $v_{max}$  moves offshore and decreases with time, so that on day 30 of experiment 3,  $v_{max} = 0.05$  m s<sup>-1</sup>, 45 km from the coast.

As in the along-shore velocity profiles, the cross-shore movement of  $v_{max}$  in experiment 2 is complicated by the ice edge and at the along-shore position at which this cross-shore profile is constructed,  $v$  is convergent across the ice edge (day 20): shoreward of the ice edge  $v$  is offshore at  $\sim 0.06$  m s<sup>-1</sup>, while seaward of the ice edge it is offshore at  $\sim 0.03$  m s<sup>-1</sup>. The convergence across the ice edge at this location leads to weak, shallow downwelling at the ice edge (described in more detail below).

Cross-sections of the vertical velocity,  $w$ , (Figures 3.14A-I, constructed at  $x = 100$  km) show that similar to previous studies of buoyant plumes (e.g. Chapman and Lentz, 1994; Fong and Geyer, 2001), in the ice-free experiment the direction of vertical circulation varies across the fronts. For example in experiment 1, seaward of the outer front (where outside of the nearshore bottom boundary layer, the vertical circulation is most intense) the vertical circulation alternates between strong downwelling ( $10^{-5} \text{ m s}^{-1}$ ) to upwelling with increasing offshore distance. Although we do not show the entire vertical extent, the vertical circulation here extends from the surface to the bottom. The vertical circulation is present on each day shown, though it weakens and moves offshore with time coincident with the offshore movement and radial spreading of the anti-cyclonic bulge. The surface and cross-shore contours of density anomaly and velocities, shown previously, show there is slight decrease in the density gradient and a lessening of along- and cross-shore velocities at this location with time, from which we expect a weakening of the vertical circulation. In addition to this deep and strong vertical circulation, inshore and near the inner front, moderate downwelling is present on all three days. The vertical velocity profiles highlight the fact that in the ice-free experiment, the outer front is closer to shore than in the ice-covered cases and thus in shallower depths. Hence, interaction with the bottom limits the depth of the downwelling in the ice-free experiment.

In experiment 2, the ice edge impacts the vertical circulation as well:  $w$  alternates between down- and up-welling shoreward of the ice edge; between  $24.5 \text{ km} < y < 26.5 \text{ km}$   $w$  alternates between  $-10^{-6} \text{ m s}^{-1}$  and  $+10^{-6} \text{ m s}^{-1}$  and  $-10^{-6} \text{ m s}^{-1}$  over these three grid

points. The ice edge vertical circulation is driven by the patterns of convergence and divergence in the cross-shore velocities noted earlier (in the descriptions of Figures 3.5 and 3.13), interacting with the pressure gradient offshore of the ice edge. (The pressure gradient offshore of the ice edge is discussed later, in regards to the momentum balance). As a consequence of the along-shore variations in along- and cross-shore flow near the ice edge, the direction of the vertical circulation varies with along-shore distance. At this location ( $x = 100$  km), seaward of the ice edge, within  $1 R_d$  (4 km) of the ice edge  $w$  is  $-10^{-6} \text{ m s}^{-1}$  (downwards). As in experiment 1, farther offshore (seaward of the outer front) the vertical circulation alternates between strong downwelling ( $10^{-5} \text{ m s}^{-1}$ ) and upwelling at increasing offshore distance. As in experiment 1, this vertical circulation extends to the bottom. In comparison to experiment 1, the vertical circulation is farther offshore and in deeper water; hence, in experiment 2 the downwelling extends deeper than in experiment 1. Note there is no area of stronger vertical circulation associated with the inner front in experiment 2.

In experiment 3, the vertical circulation is most intense on day 10 and very weak on day 30, when instead of narrow bands of intense vertical circulation there are broad areas of alternately weak up- ( $10^{-7} \text{ m s}^{-1}$ ,  $5 < y < 40$  km), down- (between  $10^{-7}$  and  $10^{-6} \text{ m s}^{-1}$ ,  $40 < y < 60$  km) and up-welling ( $10^{-8} \text{ m s}^{-1}$ , seaward of  $y = 60$  km). Comparison of these cross-shelf sections of vertical velocity with the previous figures shows the changes in vertical circulation with time, position and between experiments are due to differences in and among the experiments noted above, i.e., the anti-cyclonic bulge evolves differently in each experiment.

The results presented so far show that the time-dependent circulation under an ice cover is profoundly four dimensional varying in all directions and in time. Summarizing the momentum and density balances and how the terms change with time within dynamically different areas of the plume succinctly is difficult. Nevertheless, the momentum and density balances are very useful in understanding all aspects of the flow. As in the previous figures we summarize the momentum balances from the coast offshore at  $x = 100$  km. This approach allows us to describe how the momentum and density balances evolve with time from unsteady (day 10) to a quasi steady state (day 30) with the presumption that we capture the time-dependent quantities as they propagate downstream from small  $x$  towards large  $x$  and farther offshore with time. In the ice-free experiment within the inner front, the cross-shore momentum balance is geostrophic with a positive pressure gradient ( $-p_y / \rho_0 > 0$ ) at the surface balancing Coriolis. The signs reverse with depth, and within the bottom boundary layer vertical viscosity becomes important ( $> 0$ ). This balance holds throughout the 30 days. Between the inner and outer fronts the cross-shore momentum balance is geostrophic and substantial terms are confined to within several meters of the surface. Within the outer front, Coriolis and pressure gradient largely balance each other (at the surface); however, on day 10,  $uv_x$  is of the same sign as Coriolis and contributes to the balance (both are negative). The importance of horizontal advection decreases with time and on day 30, the balance within the outer front is geostrophic.

Under an ice cover, the cross-shore momentum balance is somewhat simpler. During the entire 30 day period, everywhere ice is present the cross-shore momentum

balance is the same as for a bottom Ekman layer and is between Coriolis, the pressure gradient and vertical viscosity due to under-ice friction. Coriolis ( $< 0$ ) and the pressure gradient ( $> 0$ ) are maximal at the surface and vertical viscosity ( $< 0$ ) has a subsurface maximum. With the exception of the nearshore bottom boundary layer, large order of magnitude terms are constrained to the top several meters (as are sizable along- and cross-shore velocities). In experiment 2, in the outer front (offshore of the ice edge) the cross-shore momentum balance is geostrophic.

The along-shore momentum balance is more complicated; in the ice-free experiment 1 within the inner front all terms contribute to the balance at the surface except horizontal viscosity and the local acceleration. Coriolis and  $wu_z$  (both  $> 0$ ) balance the remaining terms. Near the bottom vertical viscosity ( $> 0$ ) balances Coriolis ( $< 0$ ). This balance holds during the 30 day time period considered. In the outer front the balance is nearly geostrophic. The horizontal ( $uu_x < 0$  and  $vu_y > 0$ ) and vertical ( $< 0$ ) advection terms are important near the surface, though they are smaller than either Coriolis ( $< 0$ ) or the pressure gradient ( $> 0$ ) by an order of magnitude and by day 30 the advective terms are insubstantial.

Within the inner front ( $y \approx 12$  km on day 10) of experiment 3, the along-shore momentum balance is amongst vertical viscosity, the pressure gradient (both  $< 0$ ) and Coriolis acceleration. The vertical viscosity and Coriolis terms are a maximum at  $z \sim -0.32$  m and the pressure gradient decays with depth. Over time, the front moves offshore and weakens. Consequently, all terms in the momentum balance become smaller; however, the pressure gradient force weakens more rapidly than friction and Coriolis

acceleration at this location ( $y = 12$  km) so that by day 30, only an Ekman balance remains. The outer front in experiment 3 is similar to the inner front and the balance is primarily between vertical viscosity ( $< 0$ ) and Coriolis ( $> 0$ ), though the pressure gradient ( $< 0$ ) is  $\sim 1/4$  the magnitude of vertical velocity and Coriolis.

The balance of the inner front in experiment 3 is in contrast to the balance in experiment 2, where the pressure gradient is positive and opposite in sign from experiment 3. The sign reversal in experiment 2 (compared to experiment 3) is the result of the buoyancy front offshore of the ice edge. The pressure gradient due to the buoyant water offshore of the ice edge pushes on the under-ice flow and constrains the offshore tendency of the under-ice frictional boundary layer. This is similar to what we found in Chapter 1 though in the previous chapter we used vorticity arguments to explain the "ice edge effect." In contrast to experiment 3, in experiment 2, while the overall magnitude of the momentum terms decreases with time, the pressure gradient term under the ice cover remains as important as the remaining terms.

At the ice edge on day 10 all terms are important though the balance becomes geostrophic with increasing time. In addition, horizontal viscosity is substantial where the buoyant jet offshore of the ice edge converges on the ice edge. The location where horizontal viscosity at the ice edge is important moves eastward with time, as the buoyant feature where the velocities (and horizontal velocity shears) are maximum propagates downstream along the ice edge with increasing time. In the outer front  $uu_x$  and the pressure gradient (both  $< 0$ ) balance  $vu_y$  and Coriolis. In addition, within the outer front vertical viscosity is  $\sim 1/4$  of the remaining terms though still of the same order of

magnitude. Local acceleration is important initially though is unimportant by day 30 at this location ( $x = 100$  km).

While the momentum terms are interesting and important, the most pressing question is what happens to the freshwater? Figure 3.8 (freshwater flux versus time) shows that under an ice cover the downstream transport of freshwater is less than the comparable ice-free experiment despite widening of the under-ice plume; under an ice cover there is approximately 28% less downstream freshwater transport after 30 days. In part, this is due to a decrease in along-shore velocity. But that is rather a specious and circular argument since the velocity is related to the density structure. The cross-shore density profiles show deepening of the under-ice plume (i.e., freshening at depth) compared to the ice-free experiment and weakening of the density gradients under an ice cover. So the freshwater retained is mixed down and spreads farther offshore.

Since temperatures in the model are constant and near the freezing point, the equation of state depends only on salinity. Hence the salinity balance analysis is identical to the density balance. A consistent feature of the under-ice salinity balance is that salinity diffuses upward within  $\sim 1$  m of the surface at a rate of  $\sim 10^{-5} \text{ s}^{-1}$ . For example, on day 30 of experiment 3 there is positive vertical diffusion between the coast and  $\sim 50$  km offshore (at  $x = 100$  km). Vertical diffusion decreases with increasing depth and is insubstantial below about 1 m. For the ice-free experiment vertical diffusion is positive and prominent ( $\sim 10^{-4} \text{ s}^{-1}$ ) only in the inner front, elsewhere vertical salinity diffusion is barely above the background level of  $10^{-6} \text{ s}^{-1}$ . Vertical diffusion of salinity reaches a



similar magnitude in the inner front in the ice-covered experiments as well, and in all cases this is because the velocity shears are largest within this front.

As noted above, surface friction results in the largest under-ice velocities being slightly below the surface. Consequently, less dense subsurface water is transported beneath denser surface water, resulting in convective mixing within the plume. As a result the salinity balance within the plume is quite complicated. Following the ROMS output convention, the signs of the salinity balance terms are as follows,

$$S_t = uS_x + vS_y + wS_z + (AS_z)_z$$

where  $S_t$  is the salinity rate of change,  $uS_x$  is the along-shore advection of salinity,  $vS_y$  is the cross-shore advection of salinity,  $wS_z$  is the vertical advection of salinity, and  $(AS_z)_z$  is the vertical diffusion of salinity.

Figure 3.15 shows  $wS_z$  and  $vS_y$  at  $x = 100$  km on day 30 of experiment 3, i.e., the figure is a snapshot of these salinity balance terms when the along-shore velocity is a maximum at this location. The dashed contours are the 23 and 25  $\text{kg m}^{-3}$   $\Delta\rho$  contours, where the  $\Delta\rho = 23 \text{ kg m}^{-3}$  contour coincides with the offshore edge of the frontal along-shore velocity maximum (and is one of the two contours included in the cross-shore profiles of velocity shown previously). The figure shows that there is an inner ( $y \sim 42$  km) and outer ( $y \sim 60$  km) edge to the front. At the edges,  $wS_z$  and  $vS_y$  are the dominant terms in the salinity balance and both are  $10^{-4} \text{ s}^{-1}$ . Between these points the freshening at the surface is relatively large as is  $(S_t)_z$ . The interleaving with depth (over a few grid points) of positive and negative values of  $wS_z$  and  $vS_y$  is a result of the variations with depth of the velocity structure and this interleaving is entirely absent when there is no ice.

It is these variations with depth (which are indicative of convection) along with vertical diffusion that lead to the slight steepening of the density contours under the ice cover suggested by Figure 3.11, and it is these processes (diffusion and convection) that contribute to the overall deepening of the under-ice plume.

Figure 3.16 is a companion plot to Figure 3.15. The figure is a plot of the salinity balance terms within the uppermost 10 m at  $x = 100$  km and  $y = 46$  km from the coast (from experiment 3), i.e., within the plume and between the edges of the front highlighted in Figure 3.15. The figure shows that at this location, within the front, all terms in the salinity balance, except horizontal diffusion, are important at depths  $< 6$  m. Salinity decreases with time above 6 m depth and most rapidly  $\sim 1$  m below the surface where diffusion is negative and of the same order as  $S_t$ . Within the front, along-shore advection ( $uS_x$ ) leads to freshening whereas cross-shore advection ( $vS_y$ ) contributes to salinification. Note both  $u$  and  $v$  are positive. Vertical advection of salinity contributes to freshening at the surface, salinification between 0.9 and 1.5 m depths and freshening at deeper depths. Overall in experiment 3 there is no balance between the cross-shore and vertical transport of salinity as in Chapman and Lentz (1994) and hence there is no steady configuration. The result is that the under-ice plume moves continuously offshore in experiment 3.

In experiments 1 and 2 the density balances are as follows. In experiment 1 horizontal (both along- and cross-shore) and vertical advection of salinity are important within both the inner and outer fronts. Vertical diffusion of salinity is only substantial at the inner edge of the nearshore front. In experiment 2, within the inner front, vertical and cross-shore advection of salinity as well as vertical diffusion are substantial. In the outer

front, offshore of the ice edge, horizontal (both along- and cross-shore) and vertical advection balance one another. In both experiments 1 and 2, everywhere there is no ice the salinity budget is a balance amongst the vertical and along- and cross-shore advection terms and in contrast to experiment 3, the plume only spreads a finite distance offshore.

We also examined the sensitivity of the plume area to the magnitude of  $r_{ice}$ , which was  $= 10^{-4} \text{ m s}^{-1}$  in the preceding experiments. Shirasawa (1986) suggests that since the magnitude of the ice friction coefficient depends upon the roughness of the ice topography, the ice-ocean drag coefficient can vary by an order of magnitude. Based upon his values for a quadratic under-ice friction coefficient, the linear ice friction coefficient,  $r_{ice}$ , may be as large as  $10^{-3} \text{ m s}^{-1}$  (Chapter 1). We have examined how the area occupied by the plume at the surface varies in response to changes in  $r_{ice}$  (Figure 3.17) for a landfast ice cover that extends 26 km offshore. These experiments were forced with the same discharge as before. We evaluated the plume area (as per Figure 3.7) after 30 days. Our results suggest that the plume area is only weakly sensitive to  $r_{ice}$  and that even weak frictional coupling between the buoyant plume and the ice leads to an increase in cross-shore spreading of the plume in comparison to the ice-free case. However, the magnitude of  $r_{ice}$  is less important than the difference between ice-free and ice-covered cases.

Finally, we examined the sensitivity of the plume area to a cross-shore gradient in  $r_{ice}$ , (i.e.,  $r_{ice} = 10^{-2}[10^{-1}+Cy]^2$  such that the ice-ocean friction coefficient varied between  $10^{-4}$  at the coast and  $\sim 10^{-3}$  at the ice edge for the largest value of  $C$  used). The cross-shore increase in the ice friction coefficient is meant to mimic the increase in ice

roughness with distance from the coast typical of the Alaskan Beaufort landfast ice (Tucker et al., 1979). The plume area was insensitive to changes in  $C$ .

These sensitivity results are similar to those of Chapman and Lentz (1994), who found that a bottom advected plume was only weakly sensitive to the magnitude of the bottom friction coefficient. Instead, since the location where a bottom advected front is trapped is determined by the balance between cross-shelf buoyancy flux and vertical diffusion (Chapman and Lentz, 1994), the distance a bottom advected front moves offshore is extremely sensitive to the vertical mixing scheme (Chapman, 2002).

### ***3.4 Discussion and summary***

In conducting these experiments it is worth recalling that we have ignored channeling or blocking of under-ice flows by ice topography (Macdonald et al., 1987; Macdonald and Carmack, 1991) and only heuristically examined the effects of the offshore increase in ice ridging on under-ice flow (Tucker et al., 1979). Furthermore, at the same time the rivers are breaking up, landfast ice is melting and contributing a surface buoyancy flux (Dean et al., 1994; Weingartner et al., 1999). In addition under-ice plumes are thought to contribute to the melting of landfast ice (Searcy et al., 1996). The addition of a surface buoyancy flux over the shelf will alter the ambient salinity field and result in a time-dependent increase in near surface stratification. Both effects may alter the dynamics of the plumes examined here. We also have ignored the effects of winds offshore of the ice edge. We showed (Chapter 2 of this thesis) that upwelling winds along an ice edge lead to offshore transport in both the under-ice and bottom boundary layer.

Hence, upwelling winds offshore of the landfast ice edge should enhance cross-shore spreading of an under-ice buoyant plume.

Despite these simplifications our results have bearing on the Russian Arctic shelf seas where the large Siberian rivers are important to maintaining the Arctic's thermohaline structure (Bjork, 1989; Melling, 1993). While in the Canadian Beaufort, under-ice topography at least partially blocks offshore transport of river water throughout winter (Macdonald and Carmack, 1991), the landfast ice of the Kara, Laptev, and East Siberian Seas is typically smooth (Eicken et al., 2005; Divine et al., 2004). In the Laptev Sea landfast ice extends from 15 to 200 km across the shelf (Eicken et al., 2005). On average landfast ice covers the inner portion of the Laptev Sea shelf out to about the 25 m isobath and covers ~ 27% of the shelf area (Mahoney et al., 2007). In the Kara Sea landfast ice typically extends to the 10 m isobath in the western portion of the sea (~ 10 % of the shelf area) and to between the 20 and 30 m isobaths (~ 25% of the shelf area) in the eastern portion of the sea. Occasionally landfast ice can extend offshore of the 100 m isobath in the eastern Kara shelf and occupy > 50% of the shelf area (Divine et al., 2004). The winds are primarily upwelling-favorable in winter over large portions of these Eurasian shelf seas (Dmitrenko et al., 2005) and thus we expect winds will enhance the offshore transport of under-ice plumes generated by the year-round flows of the rivers that discharge onto these Eurasian shelves. Our results, which show a continual widening of the river plume (for complete/wide ice covers) under both steady and unsteady discharge conditions, suggest that even if the ice cover is > 100 km wide, fresh river discharge from the Lena, Kolyma and Indigirka will likely be transported across the

landfast ice zone and into the ice edge flaw lead. That transport should impact the quantity and the density of the water formed in the flaw leads between pack and landfast ice. Since this dense water is believed to be important in ventilating the Arctic Ocean, the landfast ice zone and its influence on the spreading of buoyant plumes needs to be properly incorporated in ocean climate models.

Although we have considered a simple landfast ice zone shelf setting, our results suggest that the YC97 scaling does not apply to this region. Our results show that there are two mechanisms by which under-ice flows interact with an immobile landfast ice cover. As is the case for idealized homogenous (both vertically averaged and unstratified) experiments of mean flow (Chapter 1 and Chapter 2 of this thesis), the first mechanism is due to the effects of a surface stress, which spreads the buoyant plume farther offshore than in the ice-free experiment. The second effect arises when the landfast ice is narrow enough that the buoyant plume can leak offshore of the ice edge. When this occurs offshore spreading of the plume beyond the ice edge is limited (and seaward of the ice edge the plume obeys the YC97 scaling) and a buoyant, narrow, along-shore jet develops along the ice edge. When ice covers the entire domain, the anti-cyclone near the river mouth extends  $> 9$  times the local baroclinic Rossby radius from the river mouth, or more than 45 km and on the order of reported values for the Colville River plume (Reimnitz, 2002). Further, the time evolution of the plume is similar to that described in YHM01, though under complete ice coverage, the anti-cyclonic bulge spreads more than the ice-free bulge and never reaches an equilibrium radius. An immobile landfast ice cover leads to a decrease in downstream freshwater flux versus time (a 28% reduction after 30 days)

despite the fact that the coastal current is wider and slightly deeper ( $\sim 1$  m) when ice is present. Overall, these experiments show that a floating landfast ice cover induces changes in buoyancy-driven flow and profoundly modifies the along- and cross-shore flow field through time in comparison to buoyancy-forced coastal currents in ice-free settings.

### ***3.5 References***

- Aagaard, K., Carmack, E.C., 1989. The role of sea ice and other fresh water in the Arctic circulation. *Journal of Geophysical Research* 94 (C10), 14485-14498.
- Alkire, M.B., Trefry, J.H., 2006. Transport of spring floodwater from rivers under ice to the Alaskan Beaufort Sea. *Journal of Geophysical Research* 111 (C12), C12008.
- Bjork, G., 1989. A one-dimensional time-dependent model for the vertical stratification of the upper Arctic Ocean. *Journal of Physical Oceanography* 19 (1), 52-67.
- Chapman, D.C., 2002. Sensitivity of a model shelfbreak front to the parameterization of vertical mixing. *Journal of Physical Oceanography* 32 (11), 3291-3298.
- Chapman, D.C., Lentz, S.J., 1994. Trapping of a coastal density front by the bottom boundary layer. *Journal of Physical Oceanography* 24 (7), 1464-1479.
- Dean, K.G., Stringer, W.J., Ahlnas, K., Searcy, C., Weingartner, T., 1994. The influence of river discharge on the thawing of sea ice, Mackenzie River Delta: albedo and temperature analyses. *Polar Research* 13 (1), 83-94.
- Divine, D.V., Korsnes, R., Makshtas, A.P., 2004. Temporal and spatial variation of shore-fast ice in the Kara Sea. *Continental Shelf Research* 24 (15), 1717-1736.
- Dmitrenko, I., Kirillov, S., Eicken, H., Markova, N., 2005. Wind-driven summer surface hydrography of the eastern Siberian shelf. *Geophysical Research Letters* 32 L14613.
- Eicken, H., Dmitrenko, I., Tyshko, K., Darovskikh, A., Dierking, W., Blahak, U., Groves, J., Kassens, H., 2005. Zonation of the Laptev Sea landfast ice cover and its importance in a frozen estuary. *Global and Planetary Change* 48 (1-3), 55-83.



- Fong, D.A., Geyer, W.R., 2001. Response of a river plume during an upwelling favorable wind event. *Journal of Geophysical Research* 106 (C1), 1067-1084.
- Garvine, R.W., 1987. Estuary plumes and fronts in shelf waters: A layer model. *Journal of Physical Oceanography* 17 (11), 1877–1896.
- Garvine, R.W., 1995. A dynamical system for classifying buoyant coastal discharges. *Continental Shelf Research* 15 (13), 1585-1596.
- Garvine, R.W., 1999. Penetration of buoyant coastal discharge onto the continental shelf: A numerical model experiment. *Journal of Physical Oceanography* 29 (8), 1892-1909.
- Granskog, M.A., Ehn, J., Niemelä, M., 2005. Characteristics and potential impacts of under-ice river plumes in the seasonally ice-covered Bothnian Bay (Baltic Sea). *Journal of Marine Systems* 53 (1-4), 187-196.
- Hedstrom, K.S., 2000. Technical manual for a coupled sea-ice/ocean circulation model (version 2) / Katherine S. Hedström. US Dept. of Interior, Minerals Management Service, Alaska Outer Continental Shelf Region, Anchorage, Alaska, p. 130.
- Horner-Devine, A.R., 2009. The bulge circulation in the Columbia River plume. *Continental Shelf Research* 29 (1), 234-251.
- Huq, P., 2009. The role of kelvin number on bulge formation from estuarine buoyant outflows. *Estuaries and Coasts* 32 (4), 709-719.
- Ingram, R.G., 1981. Characteristics of the Great Whale River Plume. *Journal of Geophysical Research* 86 (C3), 2017-2023.

- Kowalik, Z., Proshutinsky, A.I.U., 1994. The Arctic Ocean tides, in: Nansen, F., Johannessen, O.M., Muench, R.D., Overland, J.E. (Eds.), *The Polar Oceans and Their Role in Shaping the Global Environment : The Nansen Centennial Volume*. American Geophysical Union, Washington, DC, USA, pp. 137-158.
- Lentz, S., Helfrich, 2002. Buoyant gravity currents along a sloping bottom in a rotating frame. *Journal of Fluid Mechanics* 464 251-278.
- Li, S.S., Ingram, R.G., 2007. Isopycnal deepening of an under-ice river plume in coastal waters: Field observations and modeling. *Journal of Geophysical Research* 112 (C7), C07010.
- Macdonald, R.W., Carmack, E.C., 1991. The role of large-scale under-ice topography in separating estuary and ocean on an Arctic shelf. *Atmosphere-Ocean* 29 (1), 37-53.
- Macdonald, R.W., Wong, C., Erickson, P., 1987. The distribution of nutrients in the Southeastern Beaufort Sea: Implications for water circulation and primary production. *Journal of Geophysical Research* 92 (C3), 2939-2952.
- Mahoney, A., Eicken, H., Shapiro, L., 2007. How fast is landfast sea ice? A study of the attachment and detachment of nearshore ice at Barrow, Alaska. *Cold Regions Science and Technology* 47 (3), 233-255.
- McPhee, M.G., 1990. Small scale processes, in: Smith, W.C. (Ed.), *Polar Oceanography Part A Physical Science*. Academic Press, New York, pp. 287-334.
- Melling, H., 1993. The formation of a haline shelf front in wintertime in an ice-covered Arctic sea. *Continental Shelf Research* 13 (10), 1123-1147.

- Mellor, G.L., Yamada, T., 1982. Development of a turbulence closure model for geophysical fluid problems. *Reviews of Geophysics* 20 (4), 851-875.
- Morris, K., Li, S., Jefferies, M., 1999. Meso- and microscale sea-ice motion in the East Siberian Sea as determined from ERS-1 SAR data. *Journal of Glaciology* 45 (15), 370-383.
- Nof, D., Pichevin, T., 2001. The ballooning of outflows. *Journal of Physical Oceanography* 31 (10), 3045-3058.
- Reimnitz, E., 2002. Interactions of river discharge with sea ice in proximity of Arctic deltas: a review. *Polarforschung* 70, 123-134.
- Searcy, C., Dean, K., Sringer, W., 1996. A river-coastal sea ice interaction model : Mackenzie River Delta. *Journal of Geophysical Research* 101 (C4), 8885-8894.
- Shchepetkin, A.F., McWilliams, J.C., 2005. The regional oceanic modeling system (ROMS): a split-explicit, free-surface, topography-following-coordinate oceanic model. *Ocean Modelling* 9 (4), 347-404.
- Shirasawa, K., 1986. Water stress and ocean current measurements under first-year sea ice in the Canadian Arctic. *Journal of Geophysical Research* 91 (C12), 14305-14316.
- Song, Y., Haidvogel, D., 1994. A semi-implicit ocean circulation model using a generalized topography-following coordinate system. *Journal of Computational Physics* 115 (1), 228-244.

- Song, Y.T., Wright, D.G., 1998. A general pressure gradient formulation for ocean models. Part II: Energy, momentum, and bottom torque consistency. *Monthly Weather Review* 126 (12), 3231-3247.
- Trefry, J.H., Trocine, R.P., Alkire, M.B., Semmler, C.M., Savoie, M., Rember, R.D., 2009. Concentrations, composition, partitioning and dispersion pathways for suspended sediments and potential metal contaminants in the coastal Beaufort Sea. US Dept. of Interior, Minerals Management Service, Alaska Outer Continental Shelf Region, Anchorage, Alaska, p. 141.
- Tucker, W.B., III, Weeks, W.F., Frank, M., 1979. Sea ice ridging over the Alaskan continental shelf. *Journal of Geophysical Research* 84 (C8), 4885-4897.
- Walker, H.J., 1973. Spring discharge of an Arctic river determined from salinity measurements beneath sea ice. *Water Resources Research* 9 (2), 474-480.
- Weingartner, T.J., Danielson, S., Sasaki, Y., Pavlov, V., Kulakov, M., 1999. The Siberian coastal current: A wind- and buoyancy-forced Arctic coastal current. *Journal of Geophysical Research* 104 (C12), 29697-29713.
- Weingartner, T.J., Danielson, S.L., Kasper, J.L., Okkonen, S.R., 2009. Circulation and water property variations in the nearshore Alaskan Beaufort Sea (1999-2007). US Dept. of Interior, Minerals Management Service, Alaska Outer Continental Shelf Region, Anchorage, Alaska, p. 154.
- Whitney, M.M., Garvine, R.W., 2005. Wind influence on a coastal buoyant outflow. *Journal of Geophysical Research* 110 (C03014).

Yankovsky, A.E., Chapman, D.C., 1997. A simple theory for the fate of buoyant coastal discharges. *Journal of Physical Oceanography* 27 (7), 1386-1401.

Yankovsky, A.E., Hickey, B.M., Münchow, A.K., 2001. Impact of variable inflow on the dynamics of a coastal buoyant plume. *Journal of Geophysical Research* 106 (C9), 19809-19824.

### 3.6 Figures

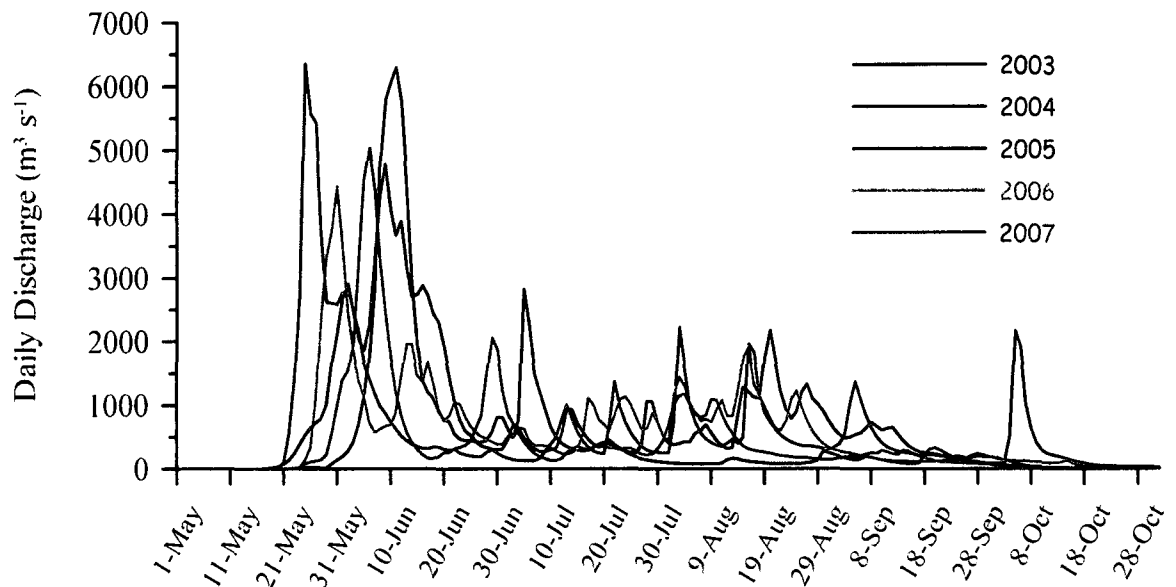


Figure 3.1. Mean daily discharge for the Colville River (2003-2007).

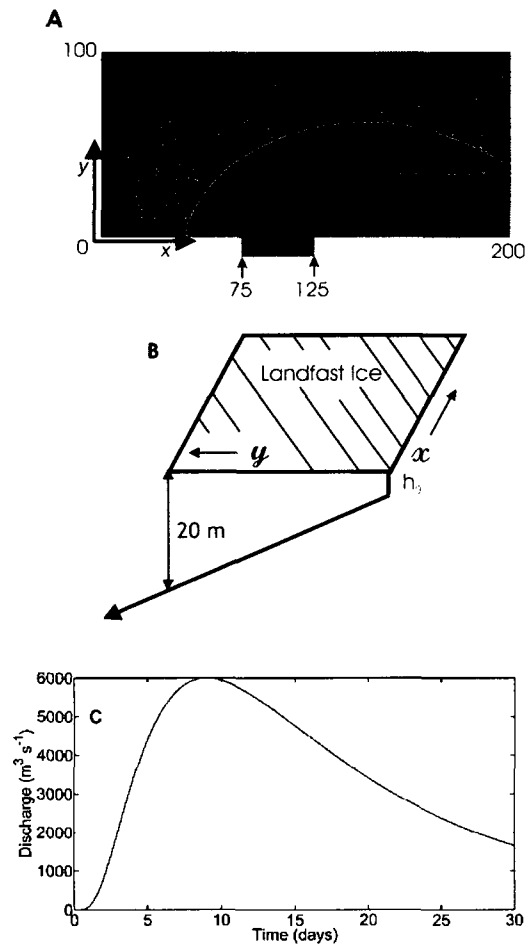


Figure 3.2. The numerical model domain and forcing. (A) A plan view schematic of the model domain. The river enters the domain through a 50 km wide gap in the southern coastline ( $75 < x < 125$  km,  $y = 0$ ). The dashed line indicates the edge of the landfast ice. Inshore of the dashed line there is ice. The cyan represents the region of river influence and blue signifies ambient shelf water. Along-shore distance,  $x$ , increases to the right (East) while cross-shore distance,  $y$ , increases toward the top of the page (North). (B) The cross-shelf view of the numerical domain. Bottom depth increases linearly with distance from the coast. (C) The idealized discharge curve.

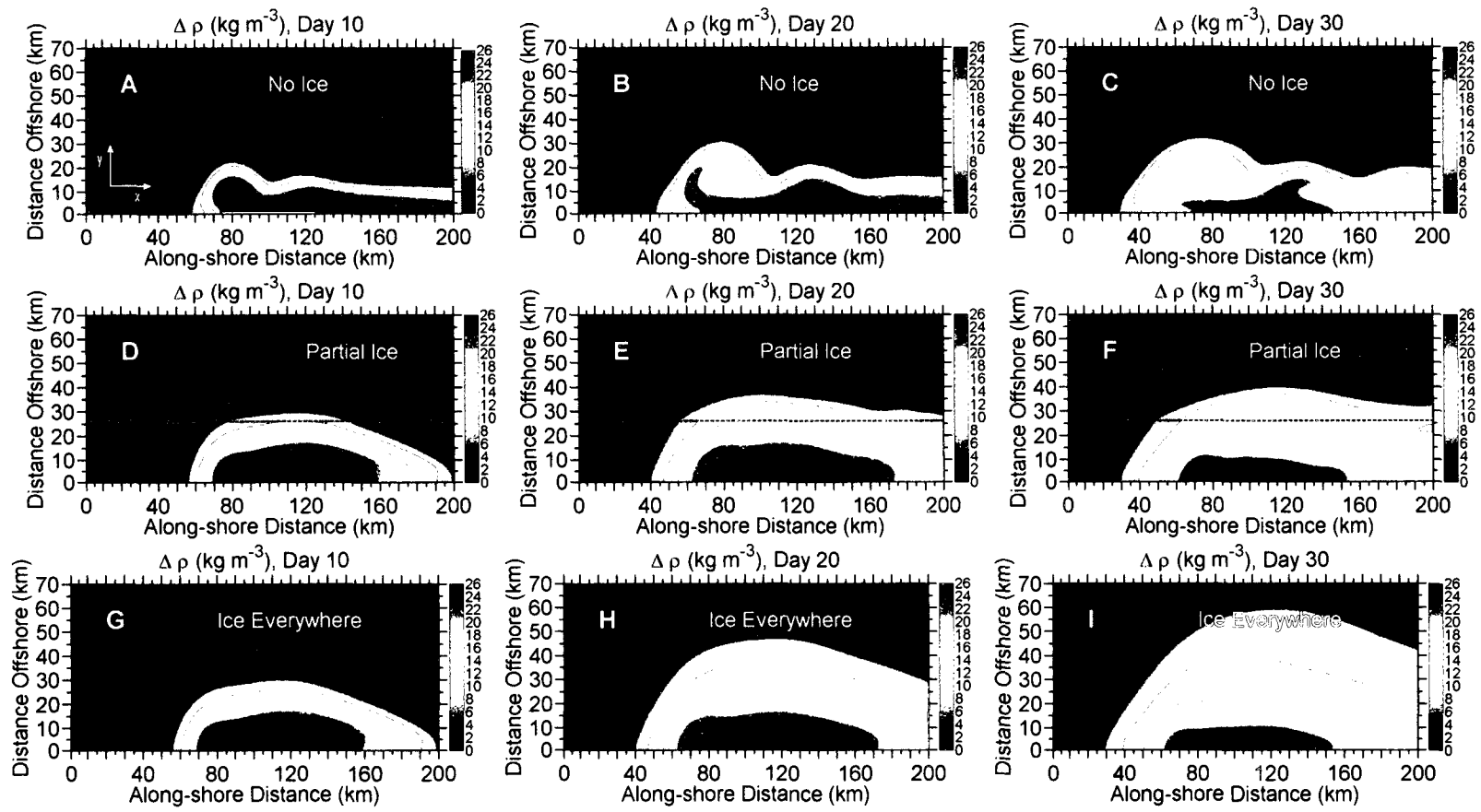


Figure 3.3. Density anomaly,  $\Delta\rho$  ( $\rho-1000$ ,  $\text{kg m}^{-3}$ ), at the surface.  $\Delta\rho$  after day 10 (A), 20 (B) and 30 (C) for experiment 1. The location of the river is marked by the white line between  $75 < x < 125$  along the coast in A. (D-F) The same except landfast ice covers the area inshore of the 20 m isobath (experiment 2). In this and subsequent figures, the ice edge is marked by the line 26 km from the coast. (G-I) The same except ice covers the entire domain (experiment 3).



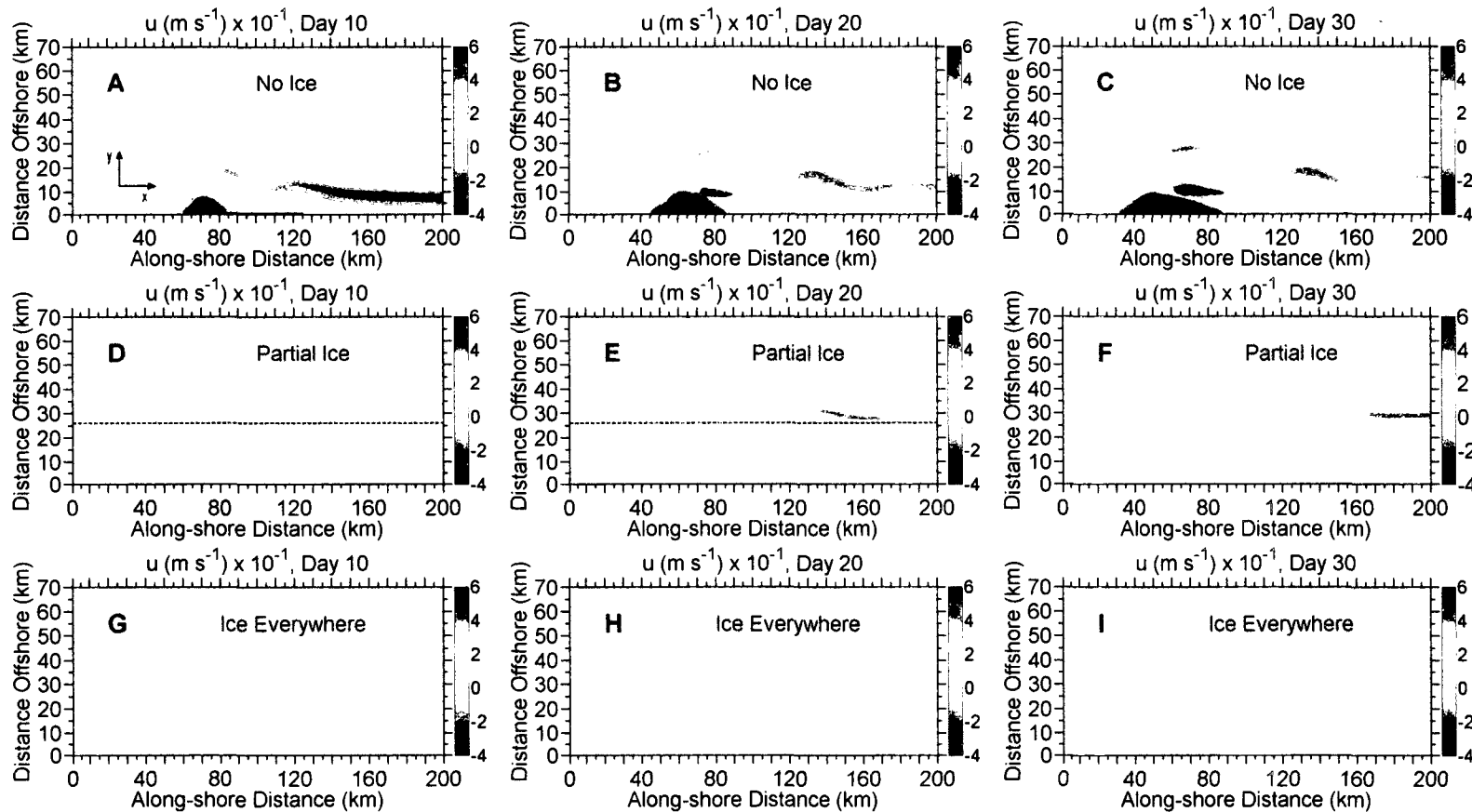


Figure 3.4. Along-shore velocity,  $u$  ( $\text{m s}^{-1}$ ) at the surface.  $u$  on day 10 (A), 20 (B) and 30 (C) for experiment 1 (positive to the right). The location of the river is marked by the black line between  $75 < x < 125$  along the coast in A. (D-F) The same except for experiment 2. (G-I) The same except for experiment 3.

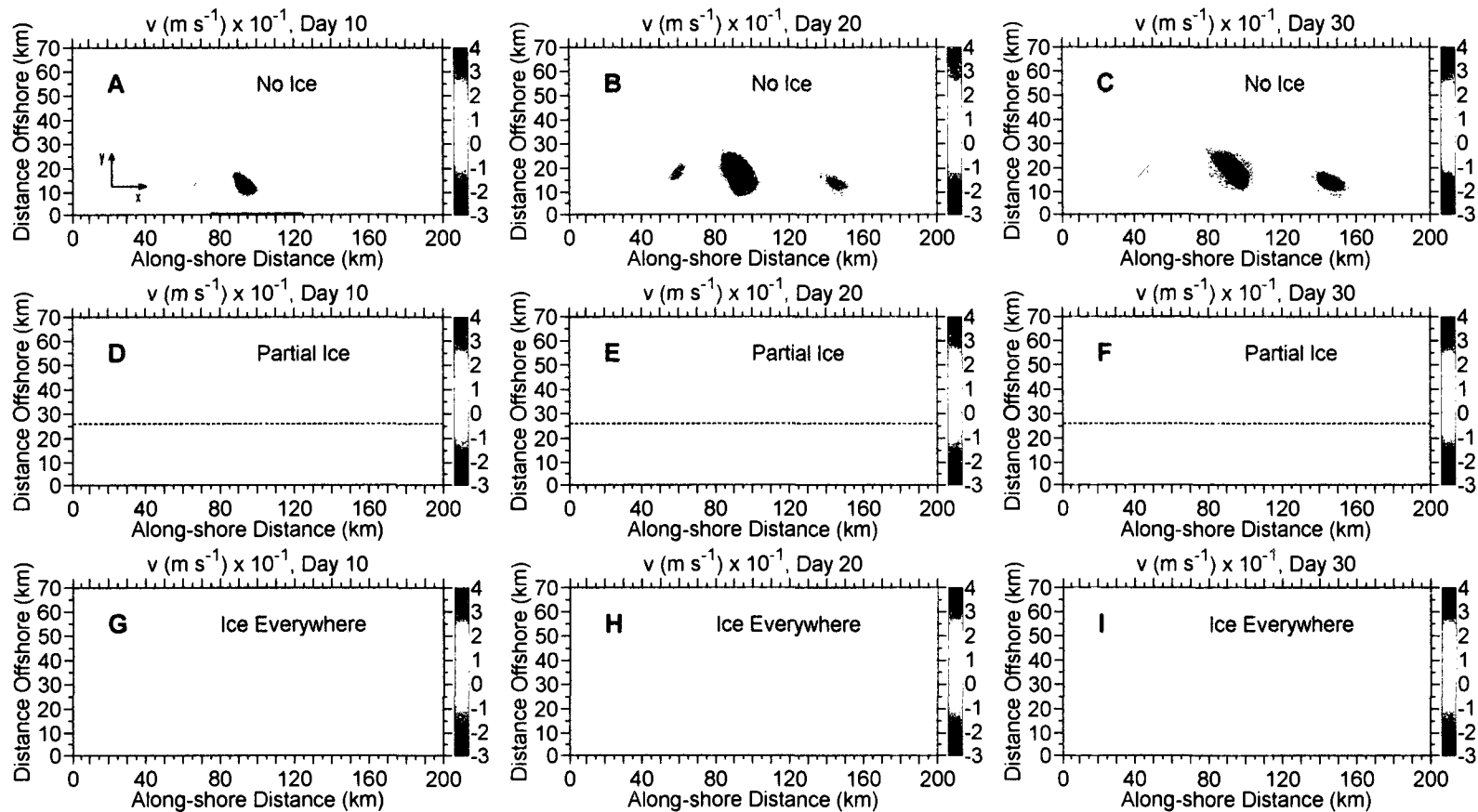


Figure 3.5. Cross-shore velocity,  $v$  ( $\text{m s}^{-1}$ ) at the surface.  $v$  on day 10 (A), 20 (B) and 30 (C) for experiment 1 (positive towards the top of the page). The location of the river is marked by the black line between  $75 < x < 125$  along the coast in A. (D-F) The same except from experiment 2. (G-I) The same except from experiment 3.

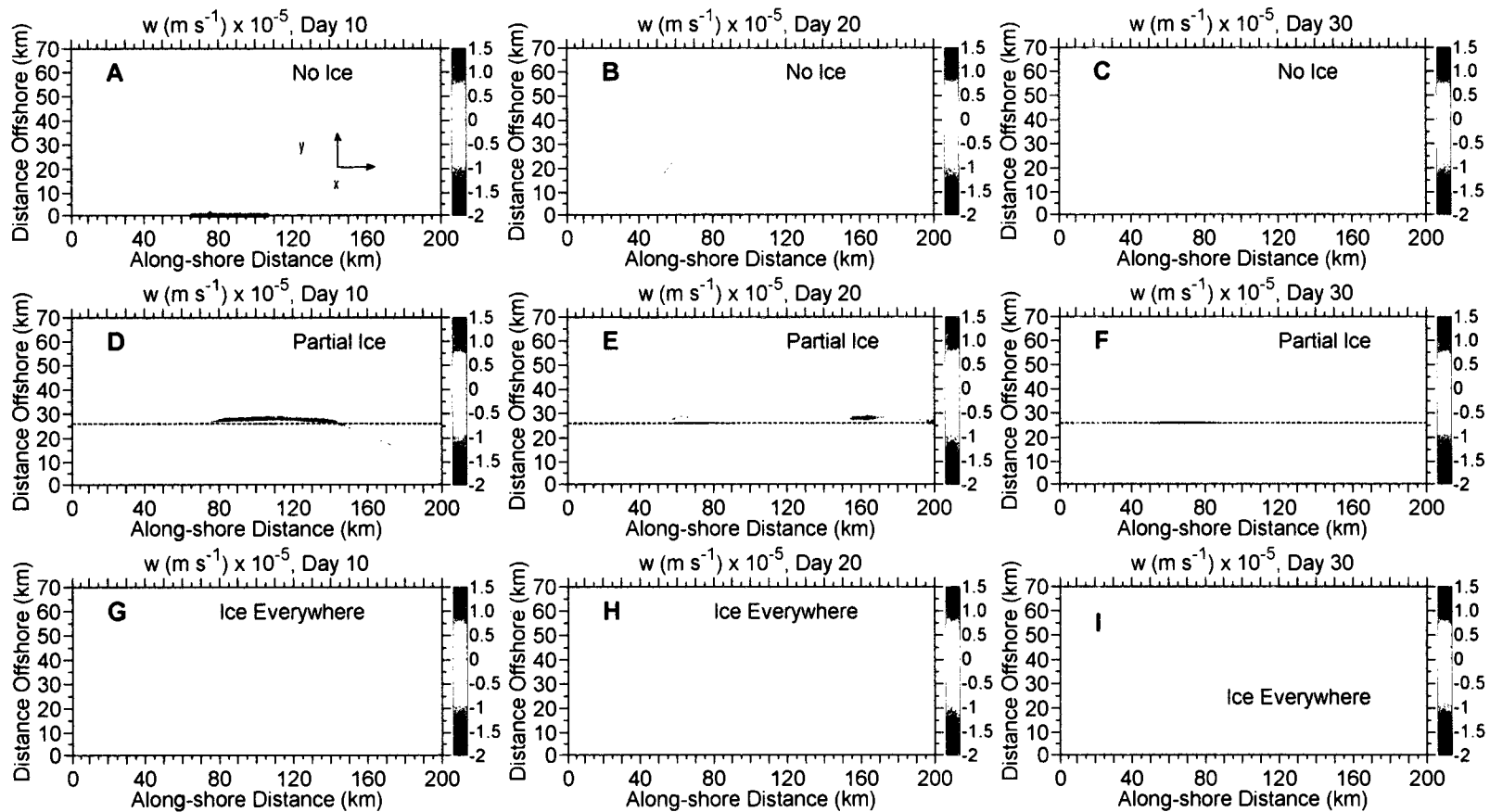


Figure 3.6. Vertical velocity,  $w$  ( $\text{m s}^{-1}$ ) at the surface.  $w$  on day 10 (A), 20 (B) and 30 (C) for experiment 1 (positive upwards).

The location of the river is marked by the black line between  $75 < x < 125$  along the coast in A. (D-F) The same except from experiment 2. (G-I) The same except from experiment 3.

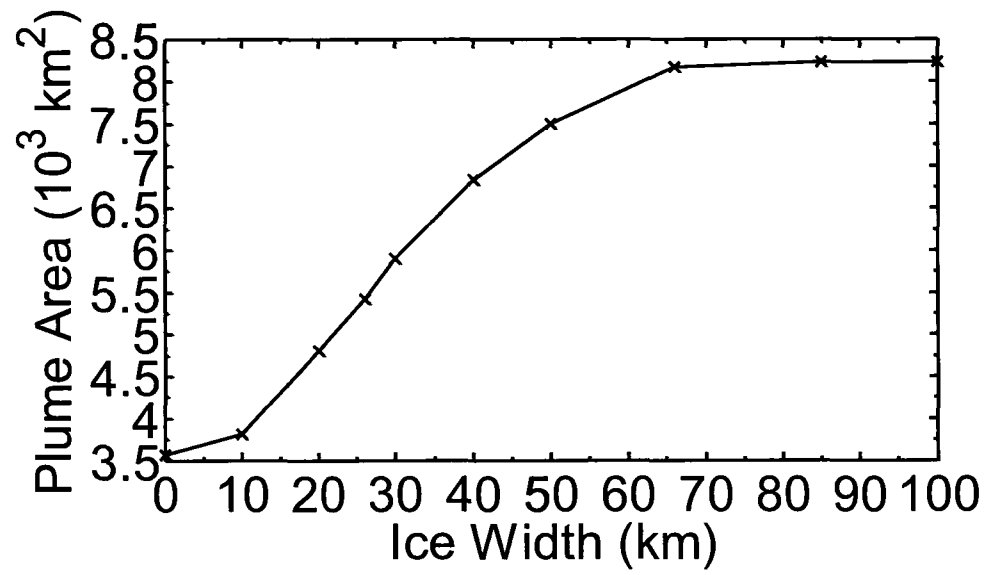


Figure 3.7. Plume area ( $10^3 \text{ km}^2$ ) on day 30 versus ice width (km).

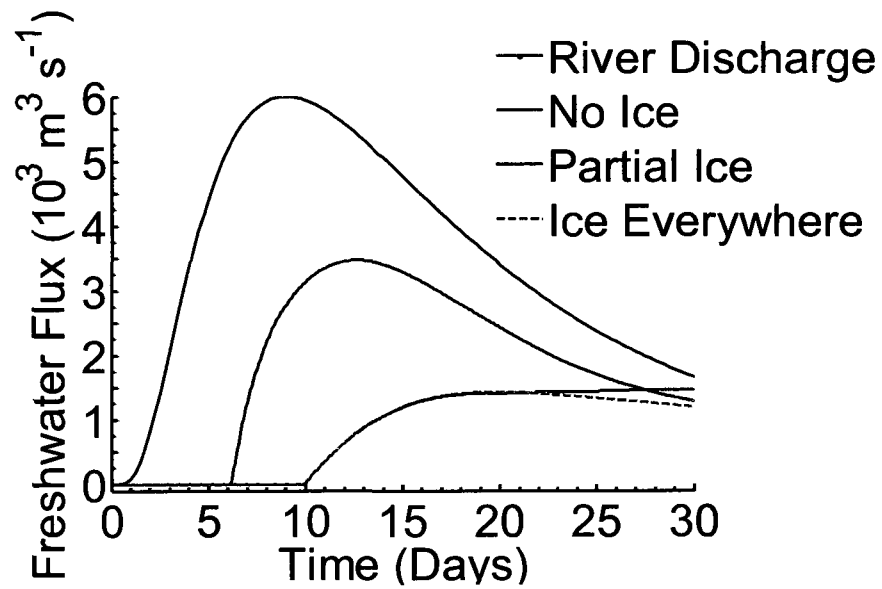


Figure 3.8. Freshwater flux,  $F$  versus time.  $F$  ( $10^3 \text{ m}^3 \text{ s}^{-1}$ ) is the volume of freshwater between  $y = 0$  km (the coast) and 100 km offshore (the Northern boundary of the domain) at  $x = 200$  km (the eastern boundary) versus time (days). For comparison, the freshwater flux contributed by the river is in blue.

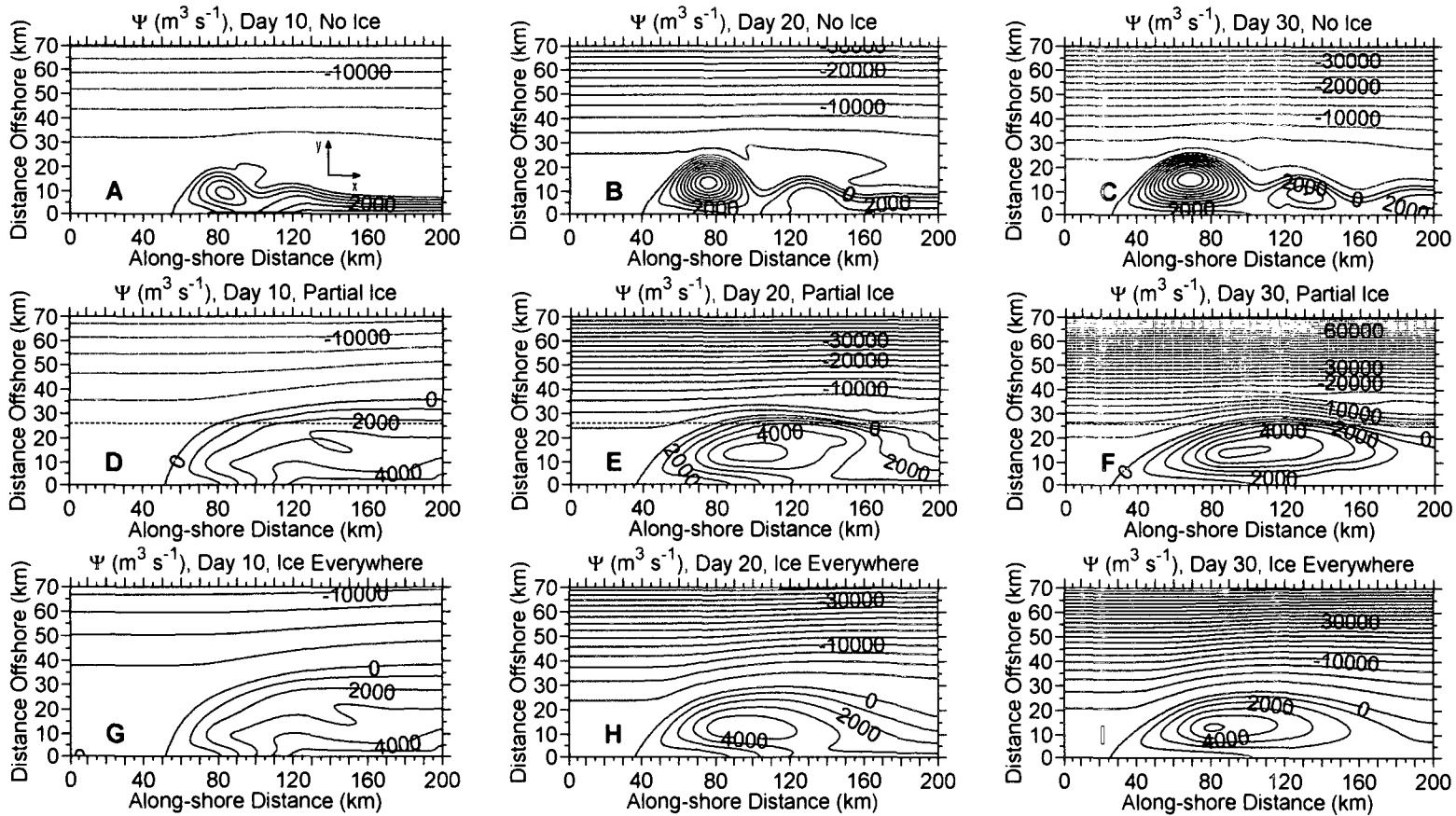


Figure 3.9. Integrated transport ( $\text{m}^3 \text{s}^{-1}$ ). Transport on 10 (A), 20 (B) and 30 (C) days for experiment 1. The location of the river is marked by the black line between  $75 < x < 125$  along the coast in A. (D-F) The same for experiment 2. (G-I) The same for experiment 3. Blue contours are negative and the contour interval is  $2500 \text{ m}^3 \text{ s}^{-1}$ . Black contours are positive and the contour interval is  $1000 \text{ m}^3 \text{ s}^{-1}$ .

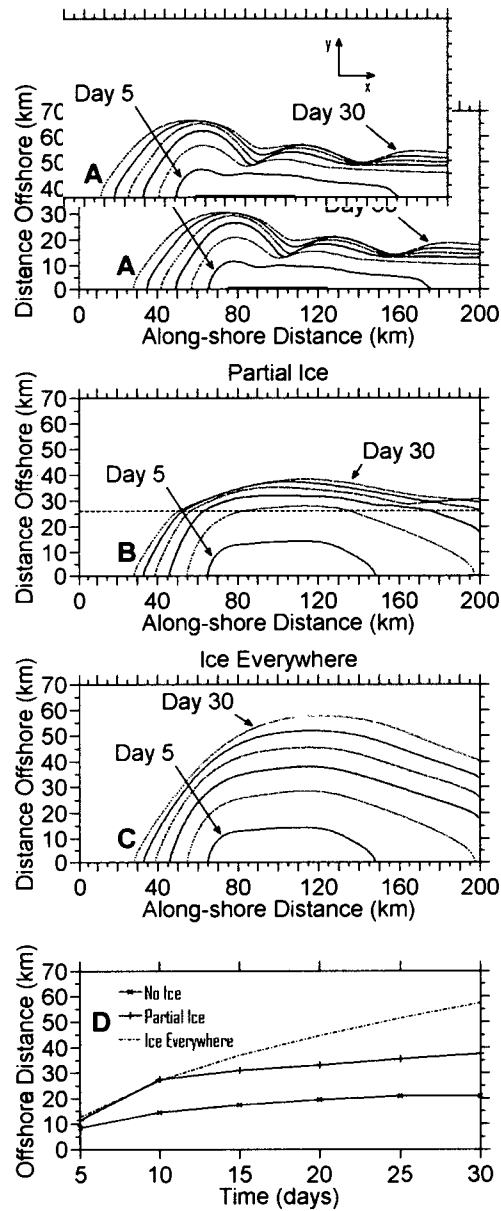


Figure 3.10. Location of the  $\Delta\rho = 25 \text{ kg m}^{-3}$  contour at 5 - 30 days (at 5 day intervals).

(A) experiment 1, (B) experiment 2 and (C) experiment 3. (D) Distance between the coast and the  $\Delta\rho = 25 \text{ kg m}^{-3}$  contour (at  $x = 130 \text{ km}$ ) versus time (days).

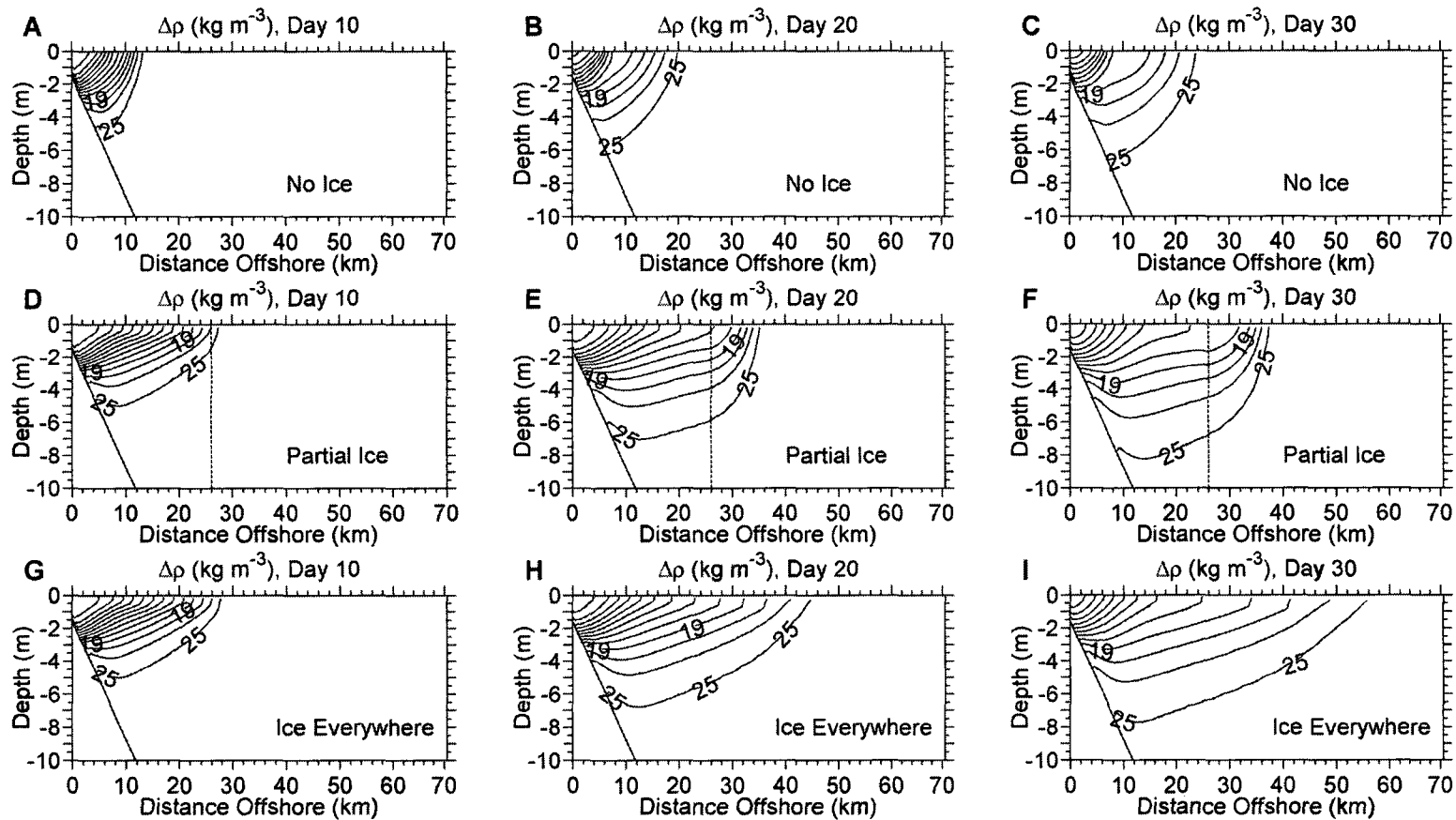


Figure 3.11. Cross-shelf sections of the density anomaly,  $\Delta\rho$  ( $\text{kg m}^{-3}$ ). Sections are from an along-shore distance,  $x = 100$  km at 10 (A), 20 (B) and 30 (C) days for experiment 1. (D-E) The same for experiment 2. (G-I) The same for experiment 3.



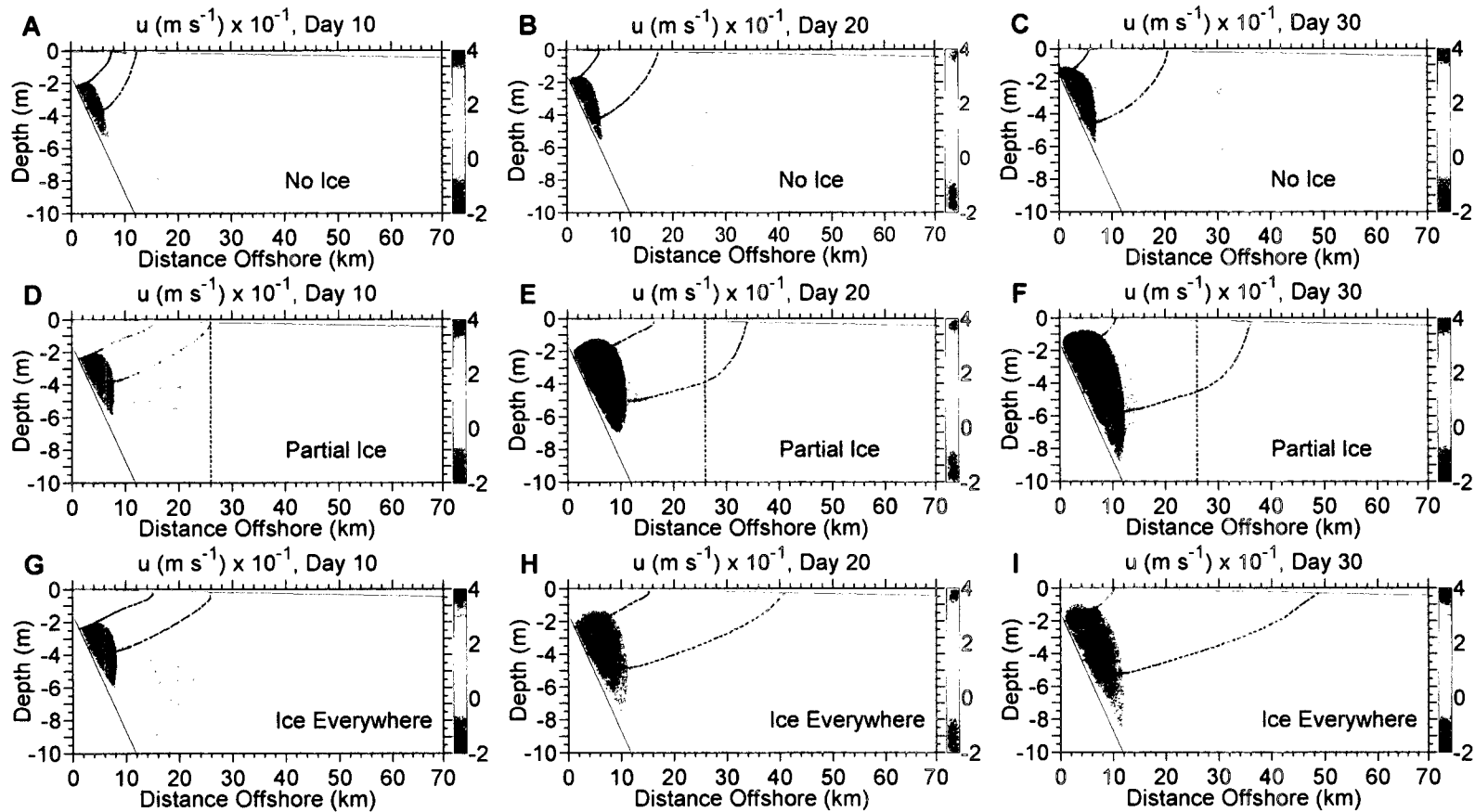


Figure 3.12. Cross-shelf sections of  $u$ , along-shore velocity ( $\text{m s}^{-1}$ ). Sections are from an along-shore distance,  $x = 100$  km at 10 (A), 20 (B) and 30 (C) days for experiment 1. Positive  $u$  are directed out of the page. The black lines are the  $\Delta\rho = 11$  (inshore) and 23 (offshore) ( $\text{kg m}^{-3}$ ) contours. (D-E) The same for experiment 2. (G-I) The same for experiment 3.

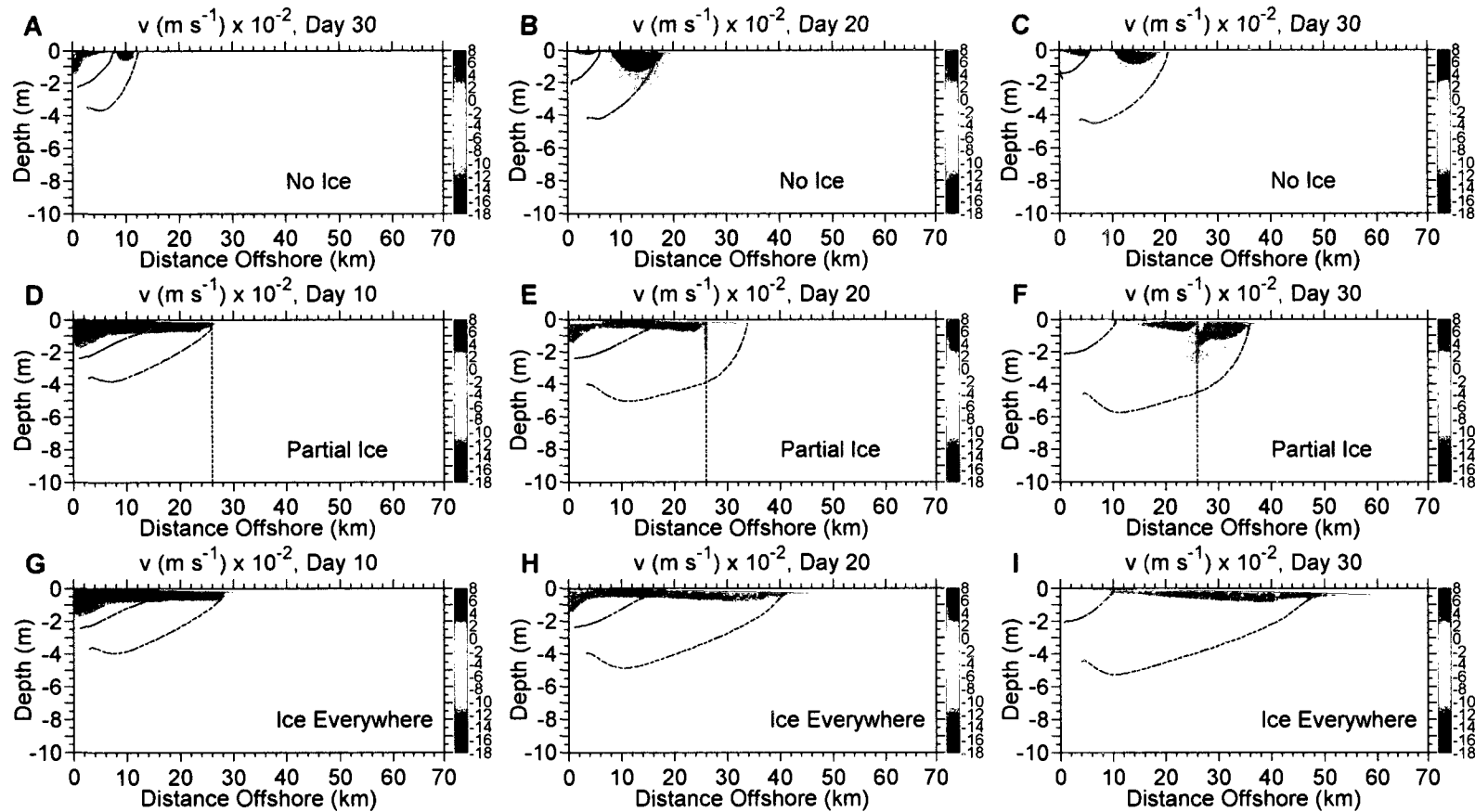


Figure 3.13. Cross-shelf sections of  $v$ , cross-shore velocity ( $\text{m s}^{-1}$ ). Sections are from an along-shore distance,  $x = 100$  km at 10 (A), 20 (B) and 30 (C) days for experiment 1. Positive  $v$  are directed towards increasing offshore distance,  $> y$ . The black lines are the  $\Delta\rho = 11$  (inshore) and 23 (offshore) ( $\text{kg m}^{-3}$ ) contours. (D-E) The same for experiment 2. (G-I) The same for experiment 3.

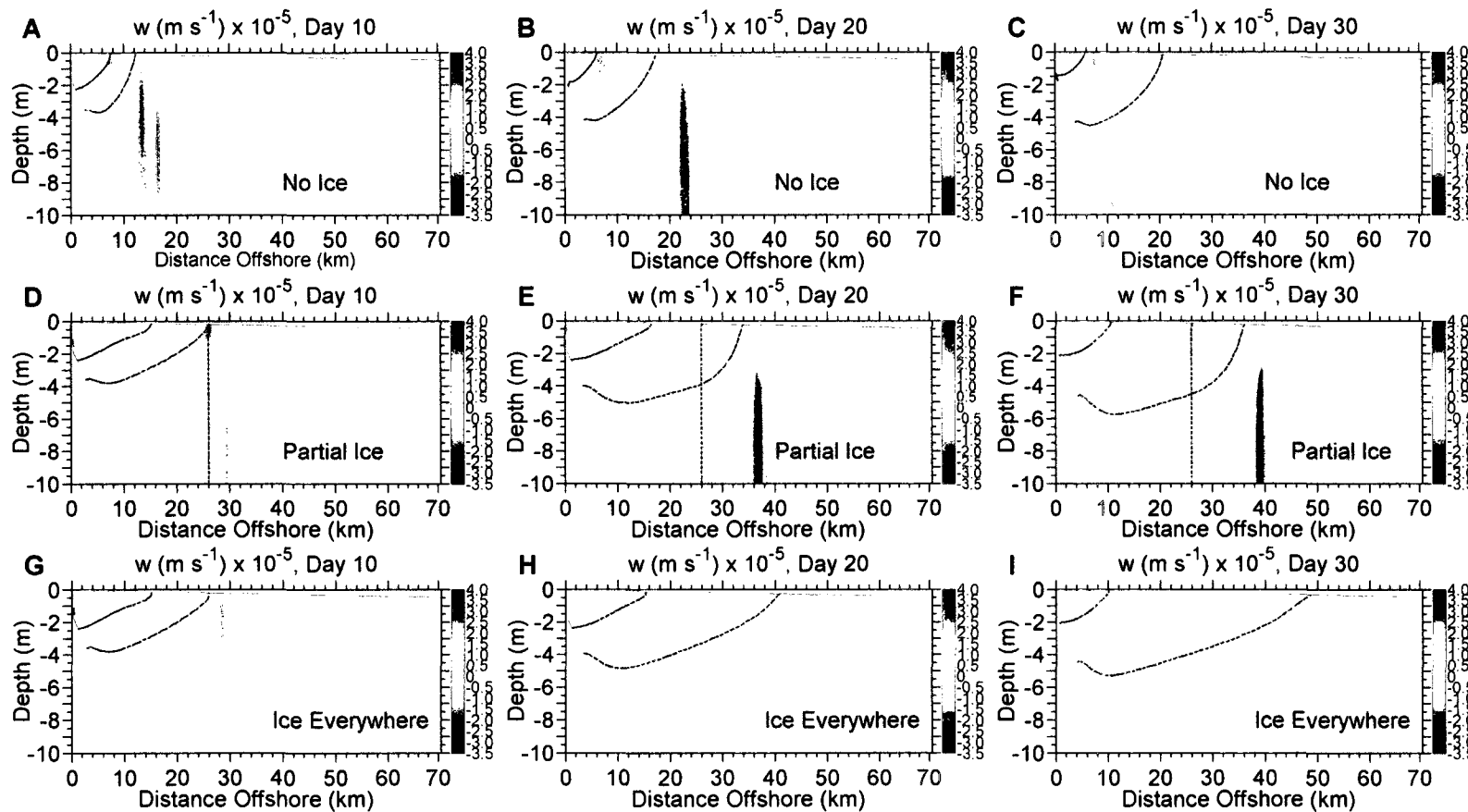


Figure 3.14. Cross-shelf sections of  $w$ , vertical velocity ( $\text{m s}^{-1}$ ). Sections are from an along-shore distance,  $x = 100$  km at 10 (A), 20 (B) and 30 (C) days for experiment 1. Positive  $w$  are directed upwards. The black lines are the  $\Delta\rho = 11$  (inshore) and 23 (offshore) ( $\text{kg m}^{-3}$ ) contours. (D-E) The same for experiment 2. (G-I) The same for experiment 3.

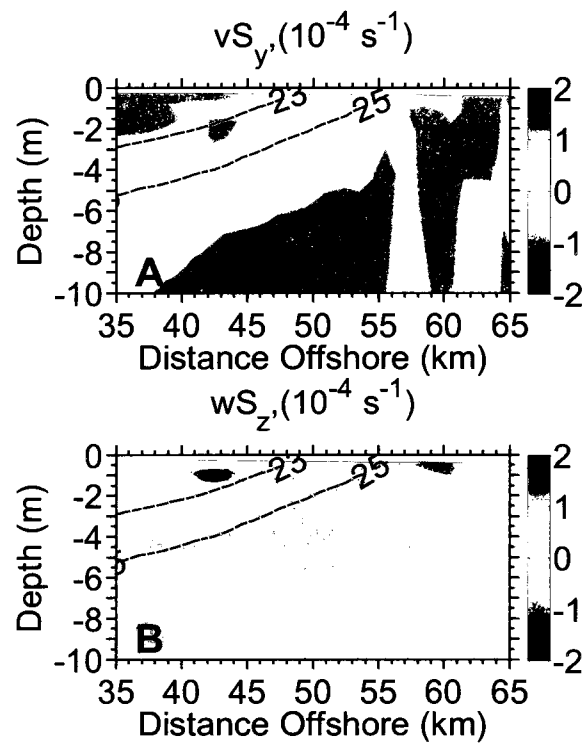


Figure 3.15. The important terms in the under-ice salinity balance. (A) Cross-shore advection of salinity ( $\text{s}^{-1}$ ) from day 30 of experiment 3. (B) Vertical advection of salinity on day 30 of experiment 3 ( $\text{s}^{-1}$ ).

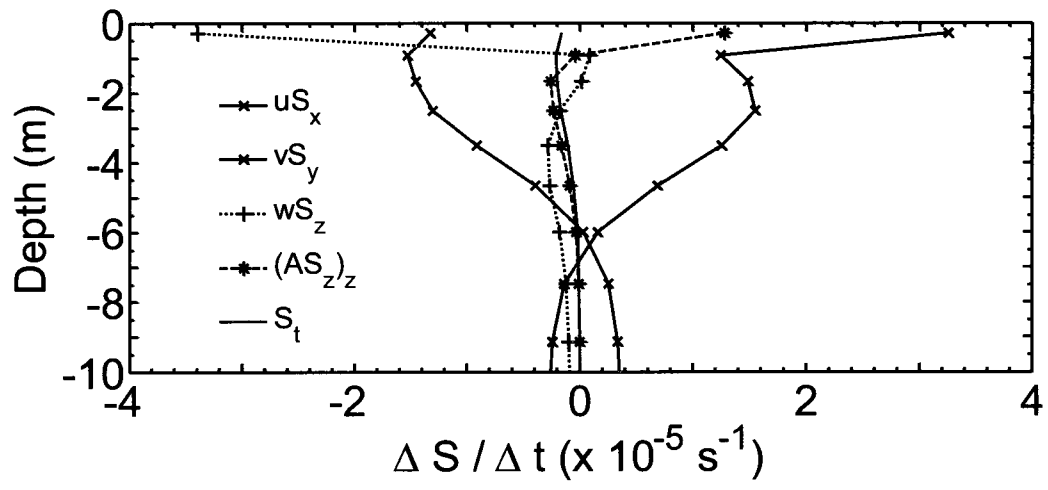


Figure 3.16. The salinity balance ( $\text{s}^{-1}$ ) on day 30 from experiment 3 at  $x = 100$  km and  $y = 46$  km.

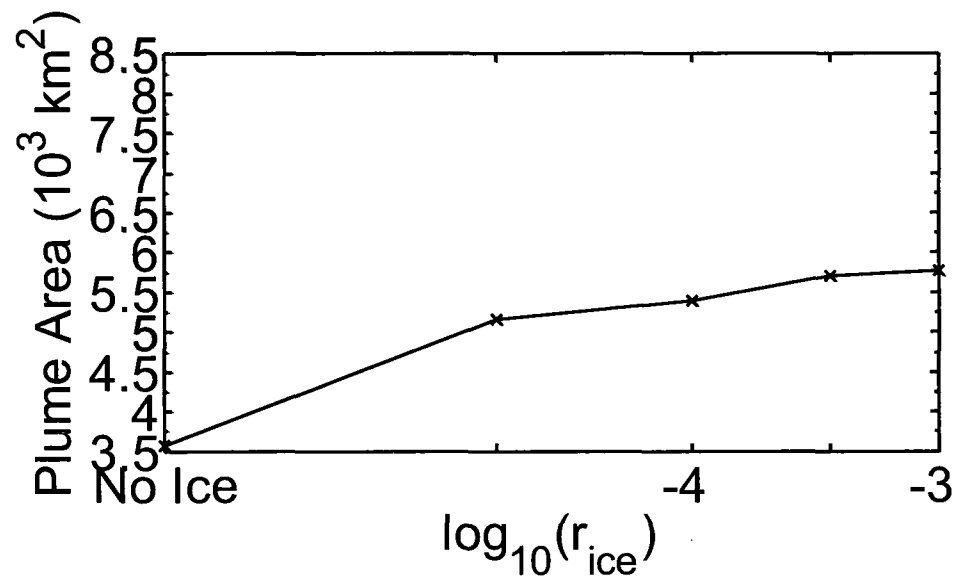


Figure 3.17 Plume area ( $10^3 \text{ km}^2$  at day 30) versus the  $\log_{10}(r_{ice})$  for a 26 km wide ice cover.

## Summary and conclusions

Idealized analytical and numerical models were used to illuminate the effect of a landfast ice cover on under-ice circulation. Landfast ice is included in the models as a surface stress, exactly analogous to placing a bottom boundary on the surface of the ocean. To investigate the effects of spatial variations in ice roughness, the linear ice-ocean friction coefficient was varied to test whether spatial variations in the ice-ocean friction coefficient exerted a torque on the water column under the ice.

Three forcing mechanisms were investigated: first we used vertically averaged analytical and numerical simulations to study the effect of a landfast ice cover on a lateral inflow (an elevated sea level at the western boundary of the shelf). Next we investigated the effect of an upwelling wind stress along a seaward landfast ice edge to determine the response of the under-ice circulation. Both vertically averaged analytical and numerical simulations were used. Unstratified numerical simulations that allowed for vertical variations were used to study exchange across the ice edge. The third forcing mechanism analyzed was a buoyant inflow under an ice cover; a river that enters the model domain through the southern coastal wall. In this case we used three dimensional numerical simulations to study the effect of landfast ice on a buoyant plume and to determine the differences between ice-free plume behavior and ice-covered buoyant plume behavior.

Lateral inflow experiments show that spatial variations in the strength of the frictional coupling between the ice and the ocean exert a vorticity torque on the water column. For a very wide ice cover where the ice-ocean friction coefficient increases with increasing distance from the coast (mimicking the offshore increase in roughness of the

Beaufort Sea landfast ice cover), the result is an increase in offshore spreading of the inflow (versus the ice-free and uniform ice cover scenarios) while for a narrow ice cover ( $< 40$  km), the effect of the surface stress curl across the ice edge exerts a vorticity torque in the opposite sense of bottom and under-ice friction (and the cross-shore increase in the under-ice frictional strength). The ice edge stress curl restricts flow under the ice in the same sense that Coriolis and the sloping bottom do in the simplified scenario we examined.

Wind driven experiments show that an along-shore, upwelling wind at the seaward landfast ice edge leads to a lowering of the sea level at the ice edge. As a result, a cross-shore sea level slope develops between the coast and the ice edge (the sea level at the coast remains higher than the sea level at the ice edge). This cross-shore sea level slope drives a geostrophically balanced upwind, under-ice flow. The magnitude of the upwind flow is largest near the ice edge (and near zero at the coast). The upwind flow initially increases but then begins to decrease after several days (the timing differs with different values of the ice-ocean friction coefficient). After 10 days, the upwind flow is weak ( $0.01 \text{ m s}^{-1}$  or less) and the sea level under the ice has decreased by  $> 1.3$  m (with a  $7 \text{ m s}^{-1}$  blowing continuously seaward of the ice edge). Cross-shore variations in the ice change the spin up and spin down time of the cycle whereas along-shore variations in the ice (along-shore variations in the ice-ocean friction coefficient and changes in ice coverage) can lead to along-shore sea level slopes that drive substantial currents, under the landfast ice cover, near the coast ( $> 0.06 \text{ m s}^{-1}$ ) after ten days.



Buoyancy forced experiments demonstrate that a landfast ice cover substantially alters the behavior of a buoyant plume from the ice-free scenario. The plume (including the anti-cyclonic bulge at the river mouth and the coastal current) are spread farther offshore than an ice-free plume with the same forcing (up to 9 times the local baroclinic deformation radius or 45 km versus  $< 30$  km for the ice-free plume). In accordance with the vertically averaged inflow experiments, the ice cover also widens the downstream coastal current compared to the ice-free scenario. When the ice cover is narrow and the plume interacts with the ice edge the change in surface stress across the ice edge leads to vertical circulation at the ice edge. The buoyant plume experiments demonstrate that Yankovsky and Chapman's 1997 scaling is not valid for an ice-covered plume and future work is necessary to develop an alternate scaling for landfast ice-covered plumes.

The results presented here suggest that more observational and theoretical research should include:

- 1) A better understanding of the frictional coupling between the ice and the ocean is necessary. This must include observations that provide insight into the spatial and temporal variability of the ice-ocean friction coefficient. Fundamentally, this depends upon knowing the variations in the ice thickness distribution of the landfast ice zone and the width of the landfast ice. Theoretical studies of how form drag (due to pressure ridges) may affect the frictional coupling between the ice and the ocean would likely be useful as well.
- 2) Observations on the distance over which the Chukchi Sea inflow influences circulation on the inner Alaskan Beaufort Shelf.

- 3) An understanding, via modeling, of the expected influence of ambient shelf stratification and horizontal density gradients on the under-ice circulation when forced by winds, along-shore pressure gradients and/or coastal discharges.
- 4) It is possible that the simple analytical solutions presented in chapters 1 and 2 of this thesis can be modified to include an ice edge and the transition zone between the landfast ice and the pack ice. Such a study would provide insight into the influence of the ice edge advective vorticity term on under-ice flow. We anticipate that the importance of this vorticity term should depend on ice width and the width of the transition zone offshore of the ice edge.
- 5) A more extensive modeling effort that explores the parameter space that governs buoyant flows under landfast ice should be undertaken. This effort should be directed at determining if a simple method for predicting how far offshore a buoyant plume will spread can be developed. This would be analogous to the development of a Yankovsky and Chapman (1997) type scaling for ice-covered arctic shelves. Such a scaling would be very useful in planning responses to marine contaminants spilled in rivers and/or beneath the ice during the spring freshet. Following Yankovsky and Chapman, the parameters that should be examined include the full range of  $Rd$  and the inflow Froude number,  $Fr$ . Thus it would be necessary to explore the full range of discharge profiles encountered in the Arctic and different shelf topographies (different latitudes, bottom slopes and coastal wall depths). Also it is important to elucidate the effect of the turbulent

closure scheme on plume depth and width (Chapman, 2002). Further our results show that a range of landfast ice widths needs to be considered as well.

- 6) In addition to further modeling efforts, since under-ice river plumes have bearing on the climate system and nearshore particle dispersal (both introduced contaminants and naturally occurring sediments and chemical species), detailed observations of large Kelvin number under-ice river plumes are necessary. Under-ice river plumes are understudied and detailed observations on the spatial scales and mixing of these plumes is lacking.
- 7) This research explored the response of the under-ice circulation to separate, but various, forcings. Since the real ABS experiences all three simultaneously, it would be useful to examine (in an idealized setting) how these affects give rise to along- and cross-shelf differences in the under-ice circulation.
- 8) Finally, this study ignored the thickness, dynamics and thermodynamics of the landfast ice cover. The dynamics of the landfast are complicated and depend on both the winds and ocean circulation as well as internal ice stresses. Consequently a more complete understanding of the under-ice circulation must include landfast ice dynamics and more realistic ice topography.

While these experiments were highly idealized, they are pertinent to dealing with any potential oil spills in shallow landfast ice-covered seas. The models demonstrate that an immobile landfast ice cover induces surface boundary layer transports that enhance offshore transport in the surface layer. This is pertinent because oil is buoyant and would presumably be constrained to surface boundary layers. This suggests that the spreading of

oil under an ice cover would be enhanced by under-ice boundary layer circulation, although these analyses do not consider the viscosity of oil and its interaction with the ice or water. At the very least the present study suggests that the potential for increased offshore transport of oil under an immobile ice cover needs farther careful consideration.

As a whole, this work represents the first comprehensive step towards developing a basic theoretical understanding of ice-covered Arctic shelf circulation. The results have suggested explanations to features of observed currents underneath the Alaskan Beaufort landfast ice cover (Weingartner et al., 2009) and suggest possible climactic implications of the large Siberian rivers on the Arctic basin. The results also demonstrate why a landfast ice cover is important to under-ice circulation and how profoundly different ice-covered shelf circulation is from ice-free shelf circulation.

## *References*

- Chapman, D.C., 2002. Sensitivity of a model shelfbreak front to the parameterization of vertical mixing. *Journal of Physical Oceanography* 32 (11), 3291-3298.
- Weingartner, T.J., Danielson, S.L., Kasper, J.L., Okkonen, S.R., 2009. Circulation and water property variations in the nearshore Alaskan Beaufort Sea (1999-2007). US Dept. of Interior, Minerals Management Service, Alaska Outer Continental Shelf Region, Anchorage, Alaska, p. 154.
- Yankovsky, A.E., Chapman, D.C., 1997. A simple theory for the fate of buoyant coastal discharges. *Journal of Physical Oceanography* 27 (7), 1386-1401.